Synergy of Earth Observations with other smart, monitoring platforms (e.g. UAVs) for precision farming: The case of vineyards in Greece

Author
Vlachopoulos Odysseas

Supervisor
Dr. Gerasopoulos Evangelos

*A thesis submitted on the fulfillment of the requirements
for the degree of Master of Science*

in the

Department of Informatics and Telecommunications,
Master of Science in Space Science Technologies and Applications

August 2017

Abstract

The recent leaps in technological advancements and the capabilities for low cost and high quality equipment has provided the agricultural and scientific community with tools and analytical methodologies that enable rapid, easy and consistent data acquisition for farming purposes.

Site-specific agricultural analysis has been performed for a pilot vineyard in the region of Attiki, Greece, during the important cultivation period of summer (June to August 2017) in regard to possible stress factors, irrigation issues, crop vigor, hydrological behavior etc., utilizing **airborne and space-borne remote sensing techniques**, while developing the **zonal approach** as a potent strategy to address those issues and consequently optimize the cultivation practices.

The current study exercises precision agriculture for vineyards, otherwise called **precision viticulture**. The methodology and the instrumentation utilized have been chosen and engineered in regard to crops specific **spectral reflectance and emissivity characteristics**, employing an **Unmanned Aircraft Systems (UAS)** with thermal and multispectral monitoring capabilities.

A commercial four-band and panchromatic sensor array, the **Parrot SEQUOIA multispectral sensor** and the **radiometric Flir Vue Pro R thermal camera** comprised the remote sensing UAS payloads, performing flights over the ~20ha vineyard area. The specific pilot site has been due to its **high internal variability** .

The multispectral, panchromatic and thermal datasets were processed through a **photogrammetric pipeline** to create orthomosaics of the surveyed area. These orthomaps were employed to extract **Vegetation Indices** like the Normalized Difference Vegetation Index (NDVI), the Red Edge Chlorophyll Index (CI-RedEdge) and others.

The pilot vineyard is also examined for the **temporal variation** of its several characteristics through the open **Sentinel-2 satellite images**, atmospherically corrected, in order to provide a holistic and consistent approach to the remotely sensed vineyards.

The whole procedure has been labored through the open Geographic Information System platform **QGIS** utilizing where needed **Python** and **R** programming languages and the commercial **Pix4D software**.

The **UAS orthomosaic products** and the **satellite multispectral images** of the vineyard were assessed for their information capacity and PV contemporary value. The overall results were highly rich in their information qualities and quantities, highlighting the spatiotemporal variation within the vineyard and providing indications for stress evaluation and optimization strategies through the interpretation of the grapevines specific characteristics, while illustrating the potential of advanced techniques like hyperspectral monitoring, very high resolution satellite imaging and the inseparable in situ components.

Keywords: *vineyard; unmanned aerial vehicle; UAV; unmanned aircraft system; UAS; precision farming; agriculture; viticulture; multispectral; thermal; photogrammetry; vegetation index; Sentinel 2; remote sensing; earth observation*

Contents

Table of Figures

List of tables

The current thesis is dedicated to my beloved partner in life Nafsika
for the unlimited support throughout every part of this endeavor.

Be a terroirist, not a terrorist.

1 Introduction

Agriculture and farming practices have been following human existence and evolution in an indivisible way. Nowadays agriculture is one of the most important economic and cultural sectors in global, national and local scale. Sustainability, food security and nutrition quality along with the equally important monitoring and assessment of the environmental and climatic impacts are inseparable aspects of todays' agricultural development and policy making around the globe.

Quoting the World Farmers' Organization Policy Paper on Climate Change and Agriculture, 2012[1], *"Agriculture, climate change, food security and poverty reduction are inextricably linked. This link is unique to the agricultural sector, and therefore, deserves proper recognition. As the world population grows to a projected 9Bn by 2050, agricultural production must also increase by an estimated 70% according to FAO. This increased production must come at a time when climate volatility, more frequent extreme weather events and temperature changes increasingly threaten the viability of agriculture and forestry sectors and rural infrastructure throughout the world. Along with food, global demand for water and energy will also increase, putting additional pressure on the world's natural resources and threatening the very ecosystems and biodiversity we rely upon to sustain ourselves."*

According to the Food and Agriculture Organization (FAO) of the United Nations[2], **food insecurity**, **agrochemical demands** and **quality assurance** in agricultural products are enormous challenges aggravated by the growing earth population, the scarcity of resources and the evident world climatic changes. These challenges are in the center of todays' policy-making highlighting the necessity for reliable, accurate, timely and sustained crop monitoring information and yield forecasts at local, national, regional and global scales.

Remote Sensing (RS) and **Earth Observation (EO)** are highly efficient tools for the acquisition of such valuable information, complementing the scientific and empirical agricultural knowledge. In this context, multiple initiatives have been developed in order to examine and determine strategies in every scale.
This era of intensive expanse and cost-effectiveness of sensing techniques and satellite data has allowed the farming activities to follow into an industrialization and incorporation of modern state-of-the-art technologies and analytical multidisciplinary practices in compliance to relevant policies and strategic aims.

The combination of farming and sensing has been generically labeled as **Precision Farming**. In respect to the agricultural sector this bundle of practices is mostly encountered as **Precision Agriculture (PA)**.

---

[1] http://www.wfo-oma.com/media/k2/attachments/WFO_policy_paper_climate.pdf
[2] http://www.fao.org/docrep/016/ap106e/ap106e.pdf

The generic scope of PA has been under specific consideration since the late 1980's. Research activities and applied practices have included various sensors, programmable automation devices, variable rate controllers and other instrumentation.

The first international journal entitled "Precision Agriculture" was published in 1999 and since then there has been a visible and well established network of scientists, facilities and governmental policy making offices around the globe that exercise PA in the field and in specialized PA conferences and fora.

In the context of term definition, "Precision" is a word of specific meaning. The concept of the precision factor is to best monitor and analyze the internal variabilities of a farming field and in continuation,
(I) interpret and apply solutions to the potential agricultural issues;
(II) apply potential optimization methods for those variables.
Modulating cultural practices as a function of spatial and temporal variation within agricultural fields is the apparent result of the process under the term Precision Agriculture (Kropff et al., 2007; Moran et al., 1997; Zhang et al., 2002).

The vast development of the **Global Navigation Satellite Systems (GNSS)** and the **Geographic Information Systems (GIS)** along with the advancements in RS and satellite exploitation, has allowed PA to become a promising practice environment for agriculture and farmers with a strategic advantage.

From ancient to modern ages the cultivation of grapevines (**Vitis Vinifera**) has been a major agricultural practice in the Mediterranean area and worldwide. Throughout the years from ancient Greek civilization until today multiple varieties have been cultivated and mitigated towards central Europe and other parts of the world. Table grapes, wine and raisins are the main products of this cultivation.

Vitis Vinifera is a plant species subject to multiple stressful or beneficial factors. Its cultivation is considered one of the most demanding and complex in modern agriculture, while the farming and consuming practices root deep in the culture and history of human society. Detailed farming activity, quality products, hazard prevention and recognition, sustainability concerns, mitigation strategies and other vital aspects are yet to be integrated and analyzed. Additionally, vineyards exhibit very important interactions with the initial and developing human design and cultivation practices.

As permanent crops, there are strong and complex relations with various features like:
- Field structure and topography chosen in regard to the specific vine variation;
- The initial vineyard architecture for the rowing and spacing of the plants;
- Various components for the best control of the interior of the vineyards like sentinel vines or trees at the borders of the vineyard;
- The agrometeorological profile of the area and the meteorologically derived and microclimatic conditional (conditions *within* each plant) design of the plants (e.g. Santorini basket -or "kouloura"- vines);
- Irrigation methods and engineered or natural water flows;

- Agrochemicals (fertilizers, herbicides, pesticides) used at specific cultivation times and possible infestations;
- Soil history, composition, structure;
- Cultivation practices like pruning and ploughing;
- Vines' characteristics like age, main root depth etc.

In the current implementation methodology of the automation behind PA, specific tools and variability sensors have been used that best fit to the vineyards RS monitoring needs.

PA methods vary in regard to the monitored crops, trees, fields or generally vegetation. For grapevines which are **permanent multi-annual crops**, a different approach from seasonal cultivated crops like corn is needed, and the bundle of precision farming practices is called **Precision Viticulture (PV)**.

PV acknowledges that **inherent variable production systems** are existent within vineyards and the objective is to control and deliver decisions and expected outcomes managing those variabilities in multiple ways.

Several grape **structural properties** like the canopy Leaf Area Index (LAI), leaf layers and density, **biochemical properties** like anthocyanins/carotenoids/phenolics content, pH, solutes and many more have been found to be spatially variable in recognized patterns within vineyard zones (Arno et al., 2009; Bramley, 2005) establishing the **zonal approach** to PV. **Other properties** like brix and berry weight are also subject to the zonal approach and can be interconnected with the structural and biochemical ones. Vines are highly complex plants that should be ideally monitored alongside their major annual growth stages (**Figure 2**) in order to assess growth factors, characteristics, potential issues, crop quality and biomass features.

Determining **discrete regions and zones of spatial variability within a vineyard** provides multiple advantages for the farming strategies towards determining precautionary measures, diagnosis, treatment and optimization in quality and quantity. In the traditional and empirical approach of vines cultivation and farming, these aspects are treated homogeneously, resulting in a series of disadvantageous and inefficient practices, a waste of resources, potential public health issues and lower quality products.

Vineyards should be monitored not only spatially in the context of the field they are planted in, but most importantly temporally, through time series of observations and status monitoring.

This is the main reason that in the case of vineyards satellite observation is essential to determine the needs and condition of grapevines. Alongside monitoring with satellites and executing Unmanned Aerial Vehicles (UAVs) very high resolution campaigns, in situ networks of relevant sensors (meteorological, air and soil humidity/temperature, soil salinity etc.) critically complement the whole PV procedures.

Figure 1 provides a sample overview of the layered information provided by the Sentinell-2 satellites and a UAV as a generic approach to PV.
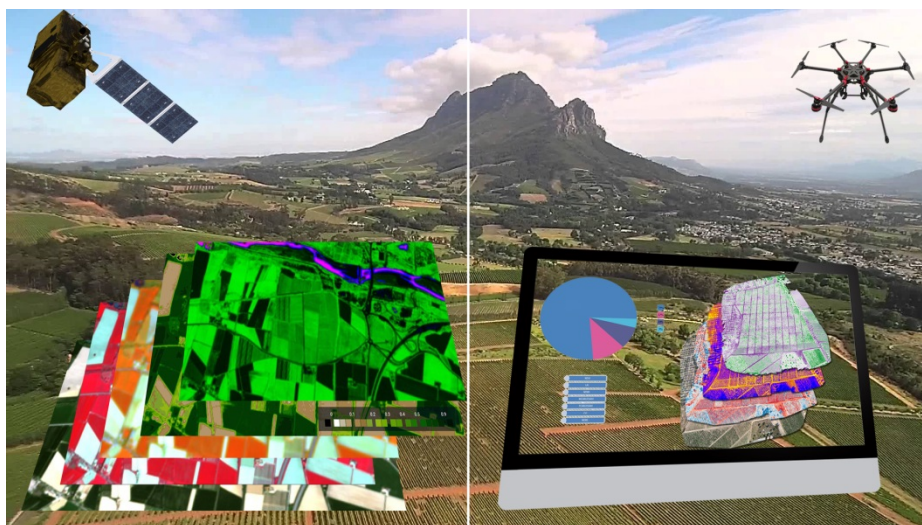
Figure 1: An overview

The main objectives of PV are

(1) the vegetation condition: needs, stress and growth;

(2) the irrigation/water management of the farming fields;

(3) the better management of fertilizers, pesticides and other agrochemicals;

(4) crop forecasting and yield predictions;

(5) decision support systems.

PV is an interdisciplinary holistic approach to vineyard farming practices, while through RS techniques a farming engineer is exercising non-destructive and time consistent monitoring methodologies.

As a result, in order to achieve better production rates, use early stress recognition tools, automatize as much as possible the production itself, make best use of resources and determine mitigation strategies due to climate change conditions, detail is vital and analysis has to be made for the specific place under the specific conditions at the specific farming activity, thus conducting **site-specific PV techniques**.

The pilot vineyard explored under the PV prism is located in Greece, engulfed in the unique characteristics of the Mediterranean basin. The macroclimatic conditions and general location of the pilot site make the PV monitoring highly interesting from both scientific and commercial views for multiple reasons:

- The Mediterranean basin is one of the regions most exposed to the risk of climate change (Intergovernmental Panel on Climate Change (IPCC), 2007);
- The Mediterranean region in general and Greece to a more specific extent, exhibit an extremely high variability that derives from a unique geological perspective and history. Topography, soil composition, climatic status and extremely variable micrometeorology (terroir factors) are principle

ingredients for this diversity and interest translated into plants and vine products unique characteristics;

- Great differentiations can be observed in vital cultivation factors like water availability/irrigation and nutrient flows;
- For the Mediterranean countries like Greece, the cultivation of vines is a very important agricultural aspect with deep cultural roots and considerable economic impact through production volumes and very high quality products appreciated and delivered all around the world;
- Very high quality wines and grapes have become trademarks of whole rural regions due to tradition and their socioeconomic impacts.

Under the above general concepts on PV and the oenological interest, the Information Communication Technologies (ICT) and GIS rapid evolution along with low cost airborne optical instruments development and open satellite data, an efficient Concept of Operations (CONOPS) can be perceived.

The high agronomical complexity of vineyards monitoring poses a real challenge for the farming engineers and the agricultural science. A multidisciplinary approach on the spatiotemporal variability and the extremely rich observational data on vineyards can be acquired and transformed into useful knowledge aiming towards the maximization of the quantitative, qualitative and sustainability grapevine properties.

This endeavor has been initiated in the current study utilizing the tailored instrumentation acquired through a successful proposal to the **ESA Earth Observation Entrepreneurship Initiative (EOEI)**. The UAS and the vegetation monitoring payloads have been acquired as the proposal's needs for the implementation of a PA CONOPS.

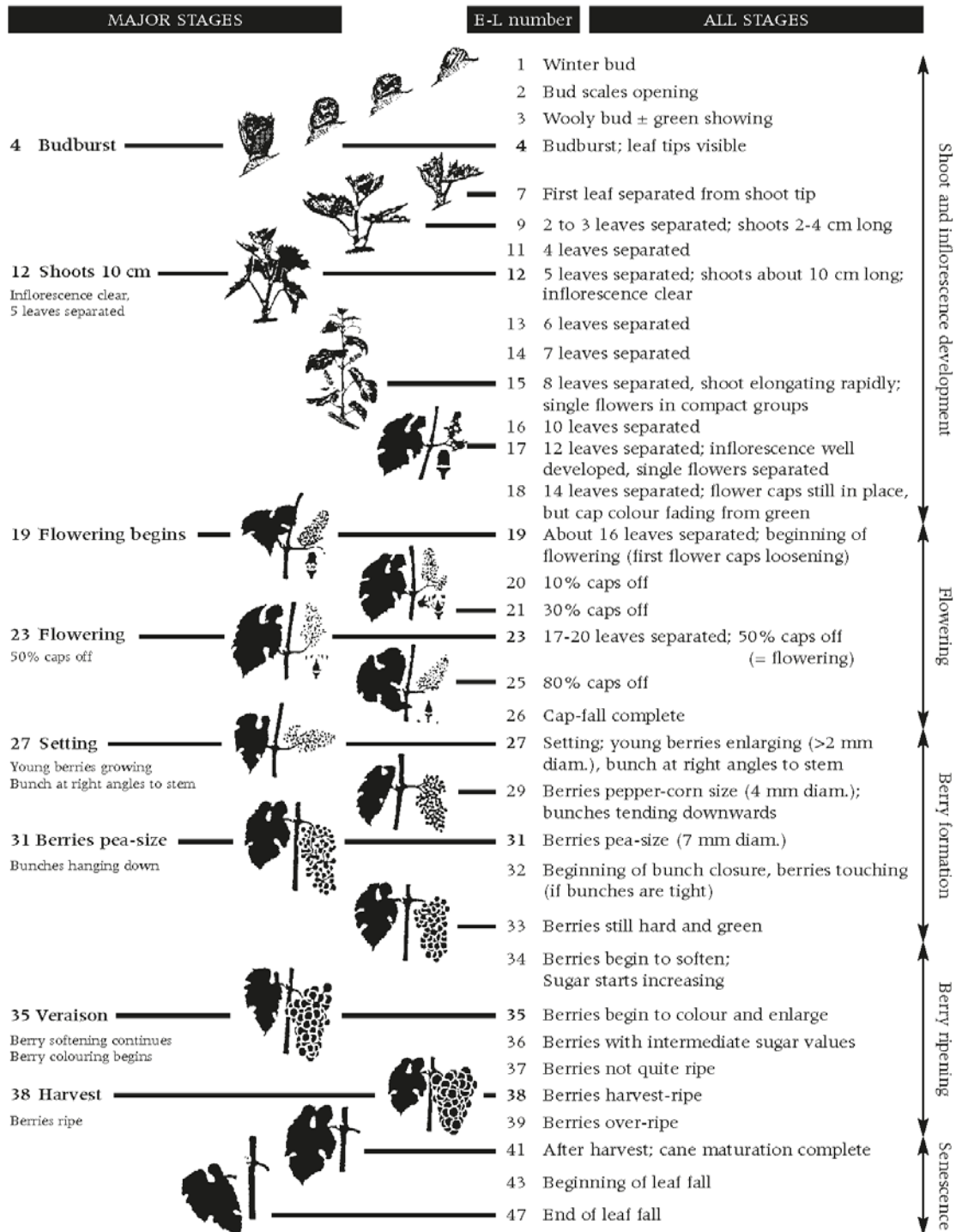| MAJOR STAGES	E-L number	ALL STAGES	
	1	Winter bud	
	2	Bud scales opening	
	3	Wooly bud ± green showing	
4 Budburst	4	Budburst; leaf tips visible	Shoot and inflorescence development
	7	First leaf separated from shoot tip	
	9	2 to 3 leaves separated; shoots 2-4 cm long	
	11	4 leaves separated	
12 Shoots 10 cm	12	5 leaves separated; shoots about 10 cm long; inflorescence clear	
Inflorescence clear, 5 leaves separated	13	6 leaves separated	
	14	7 leaves separated	
	15	8 leaves separated, shoot elongating rapidly; single flowers in compact groups	
	16	10 leaves separated	
	17	12 leaves separated; inflorescence well developed, single flowers separated	
	18	14 leaves separated; flower caps still in place, but cap colour fading from green	
19 Flowering begins	19	About 16 leaves separated; beginning of flowering (first flower caps loosening)	Flowering
	20	10% caps off	
	21	30% caps off	
23 Flowering	23	17-20 leaves separated; 50% caps off (= flowering)	
50% caps off	25	80% caps off	
	26	Cap-fall complete	
27 Setting	27	Setting; young berries enlarging (>2 mm diam.), bunch at right angles to stem	Berry formation
Young berries growing Bunch at right angles to stem	29	Berries pepper-corn size (4 mm diam.); bunches tending downwards	
31 Berries pea-size	31	Berries pea-size (7 mm diam.)	
Bunches hanging down	32	Beginning of bunch closure, berries touching (if bunches are tight)	
	33	Berries still hard and green	
	34	Berries begin to soften; Sugar starts increasing	Berry ripening
35 Veraison	35	Berries begin to colour and enlarge	
Berry softening continues Berry colouring begins	36	Berries with intermediate sugar values	
	37	Berries not quite ripe	
38 Harvest	38	Berries harvest-ripe	
Berries ripe	39	Berries over-ripe	
	41	After harvest; cane maturation complete	Senescence
	43	Beginning of leaf fall	
	47	End of leaf fall	

Figure 2: Diagram of the vine growth stages (source: Coombe and Dry, 2004)

6

2 Remote Sensing as a tool for Agriculture

2.1 The overview

Remote Sensing (RS) is defined as "*the acquisition of data using a remotely located sensing device, and the extraction of information from this data*" (McCloy, 2006). It has also been considered as the technique to observe and depict objects or phenomena under the assumption that no physical contact or destructive methods have been applied in the process. In this context, RS has been a continuously advancing method of observing the Earth (**Figure 3**) and in this particular subject, vegetation and crops (Landgrebe, 1999; Liaghat and Balasundram, 2010; Schellberg et al., 2008).
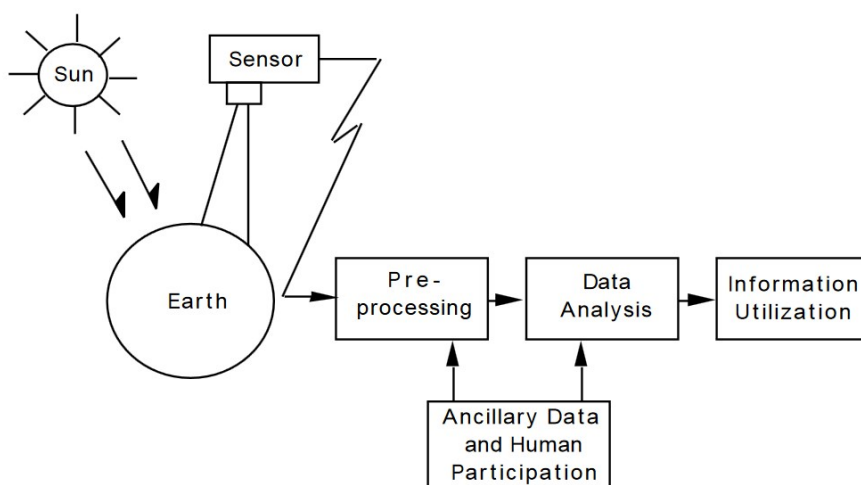
Figure 3: A conceptual overview of an RS based information system. Source: Landgrebe, 1999

RS usually refers to **space-borne**, **air-borne** and **ground-based** technology and instrumentation that include multiple different and highly complementary techniques in regard to scientific, empirical and quantitative results. The remote sensors are clustered in two groups: passive and active. Passive remote sensors like photographic optical sensors and radiometers are sensors that respond to external only stimuli and gather radiation through reflectance or emission from the objects under inspection. The most common source of radiation detected and recorded by passive sensors is reflected sunlight. Active remote sensors like Radars and Lidars are instruments that use internal stimuli and make detailed use of emitted and backscattered radiation determining the inspected object by the time delay of the radiation emitted and the target geometry.

This differentiated RS equipment has a vast variety of uses and has been extensively used in vegetation monitoring since the beginning of the 20th century, delivering excellent products and scientific results. Cameras with very high resolution and sensitivity, new mathematical approaches in Radar technology, swarms of satellites and aerial vehicles bearing such instrumentation are examples that highlight the surge in quantity and quality of the EO products all around the globe.

These advancements in RS and EO have been achieved through the operational variability in respect to the instruments' **spatial, temporal, spectral and radiometric resolutions**, as well as technical specifications like size, operability, production rates and accessibility.

Of particular interest for RS technology as payloads of EO satellites or air-borne vehicles are the Spatial , Spectral, Temporal and Radiometric resolutions (Hall et al., 2002).

- **Spatial** resolution describes the detail, the pixel size (one side of the pixel square) in a photographic image, and ranges according to the instrument. Satellite imagery is regulated by international and national laws and can be as low as 30cm ranging up to kilometers in global observation products. On the other hand, aerial images can have spatial resolutions of few centimeters.
- **Temporal** resolution applies mainly to satellite data, describing the frequency, the time elapsed, from sequential depiction of a given object or area. When considering the temporal dimension of the RS image data, the main factors under consideration are the shadowing effects, the leaf status for vegetation along with its phenological complexity and the seasonal differentiations.
- **Spectral** resolution is defined by the portions and the range of the electromagnetic radiation spectrum discrete segments that is recorded by the imaging system. In this manner, the information acquired is extracted by the targets' spectral reflectance curve or spectral signature, which define the characteristics and the unique characterization of the observed material (here mainly vegetation and soil). The higher the spectral resolution the more complete is the discrimination and distinctiveness of the different objects and their different states, specifically for the vegetation.
- **Radiometric** resolution is determined by the sensor's sensitivity to the magnitude of the electromagnetic energy, thus determining its ability to detect small differences in the reflected or emitted energy. In imagery the radiometric resolution is represented and measured by the number of discrete brightness levels recorded in each pixel. This is delivered by pixel data whose every dimension is measured in positive numbers from 0 to a specific power of 2, using bits to code them in binary format. For example if a sensor digitalizes the pixel brightness value with 8 bits, there should be 2^8=256 digital values available, ranging from 0 to 255 (grayscale levels, usually expressed in 8, 11, 12 or 16bits).

Tradeoffs should be particularly considered concerning RS data and their resolutions. In order to acquire high spatial resolution the optical sensors have to be designed with a small Instantaneous Field of View (IFOV), which in return reduces the energy input to the sensor, thus reducing the radiometric resolution. In order to acquire the same high spatial resolution while keeping high radiometric resolution by allowing high amounts of energy input to the sensor, it would be necessary to broaden the wavelength range for a given band, thus reducing the spectral resolution. As a result, instrumentation for RS is designed to best fit the objectives under consideration.

By those principles and the particular observation targets, the Sentinel 2 Multispectral Instrument (MSI) and the UAV optical instruments have been designed and chosen for the agricultural and vegetation applications, measuring solar radiation reflected and emitted by vegetation at specific wavelength intervals. Details on their specifics follow in the corresponding chapters.

All materials that are reached by radiation are subject to multiple physical and chemical processes. In respect to incident light radiation from our sun, radiation is reflected, transmitted and absorbed in compliance with the law of conservation of energy. These interactions of radiation with matter are dependent on the radiation itself and the material it reaches upon. Different conditions result in different and variable interactions.

2.2 Vegetation features within the electromagnetic spectrum

Vegetation in the current context is observed in their two main interactions with solar energy: **absorption and reflection** (Wooley, 1970), both of which vary according to multiple factors that are correlated with age, leaves internal and external structural characteristics, pigments (chlorophylls, carotenoids), dry matter, water content, radiation wavelength, incidence angle etc.

In regard to **absorbed radiation**, the photosynthetic active radiation (PAR), used for photosynthesis and organic matter composition, accounts for about 1/3 of the total absorbed radiation and the thermal effective radiation, which is used for transpiration and plant temperature, accounts for almost 2/3 of the total absorbed radiation. The optical properties of plants regarding the absorbed radiation is once again dependent on their particular characteristics from canopy and leaves, down to molecular level.

Reflectance is of particular interest as it is the principal measurement used under the current methodologies for the optical space-borne and air-borne instruments. Reflectance has the characteristic of being independent of the amount of radiation reaching a surface, thus allowing the detection of the corresponding variabilities and uniqueness in reflectance between different objects/materials independently of external variabilities or under calibration techniques that formulate those variabilities e.g. illumination angles.

In the field of vegetation monitoring and RS, extensive studies have been made in regard to vegetation spectral characteristics and its spectral reflectance transforms called **vegetation indices (VIs)**, correlating them with stress and physiology, photosynthetic capacity, fraction of absorbed photosynthetically active radiation (FAPAR), nutrient deficiency, leaf area, biomass and other phenotypical observations (Myneni et al., 1995) and biochemical properties.

From the empirical inspections to today's state-of-the-art spectral analyses and mathematical formulations, the philosophy is that most indices are derivatives of surface reflectance depending on the wavelength portion under observation. The unique way that vegetation reflects the electromagnetic spectrum of the solar energy is its spectral signature (Smith, 2001), (**Figure 4**).

The general interaction of spectra with vegetation is generally well-documented[3]. In **the visible part of the spectrum (400 to 700 nm),** photosynthesizing plants do not reflect much light in violet-blue (~ 450

---

[3] Passive remote sensing usually does not take into account the solar-induced chlorophyll fluorescence emittance of vegetation which is a form of luminescence at longer wavelengths than those absorbed (~1% of the solar energy captured) and quite small compared to the reflected radiation. However, it has been under detailed studies in the recent years (MDPI — Remote Sensing Special Issue "Remote Sensing of Vegetation Fluorescence and Photosynthetic Efficiency", 2017).

nm) or red (~ 670 nm) wavelength regions, also known as chlorophyll absorption bands, because chlorophylls and other pigments/leaf biochemical constituents absorb much of the incident energy in these wavelengths for the process of photosynthesis (Hoffer, 1978). Those observations are deduced by the corresponding absorption peaks at ~420, 490 and 660 nm. Under a simplistic scheme, the portions of Red, Green and Blue light reflected show the vigor, the photosynthetic status of plants. The higher the chlorophylls concentration the greener the vegetation as it highly reflects Green while absorbing the wavelengths perceived as other colors by the human optical instrument, the eyes. On the other hand, vegetation decline and chlorophylls degradation translates to higher Red wavelengths reflection, while carotenoids (xanthophylls and carotenes), which degrade in slower rates, now dominate the leaves absorbing Blue light and reflecting Red and Green, thus resulting in the visible yellow vegetation color. This is a phenotyping visual interpretation of vegetation condition and can only provide limited information about the true nature of plants and their state, particularly between distinctive growth stages or under conditions that will soon be visibly stress generating. However, it is the visible part of the spectrum that carries the energy needed for vegetation to synthesize organic compounds and grow. In later stages of vegetation stagnation and in the process of death, tannins, brown pigments develop and the overall leaves reflectance in the visible spectra decreases proportionally.

The specific mechanisms of vegetation and light interactions in all the different inertial layers and composition are part of a different methodology that would unfold under specific conditions the details about a particular plant, something that concerns a future endeavor for vitis vinifera.
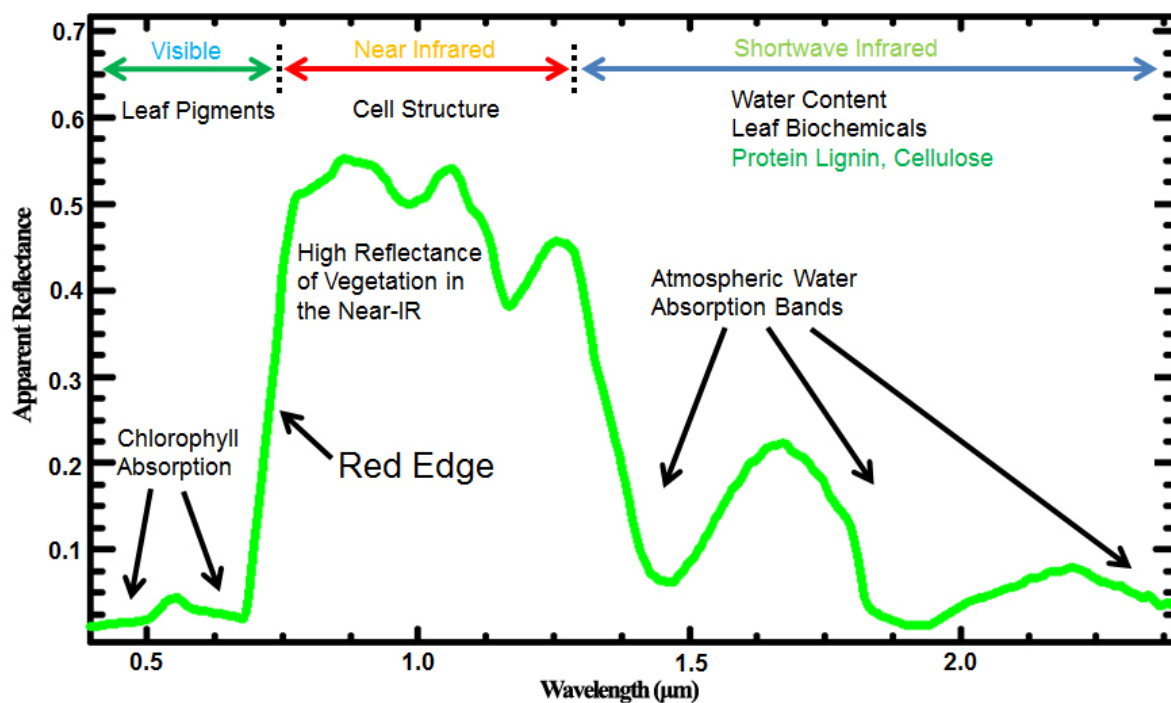

Figure 4: Typical vegetation spectral signature (green), Source, modified: Mark Elowitz

In the edge and outside of the visible part of the spectrum, especially in the Near-Infrared (NIR), vegetation provides a tremendous amount of information, a universe of invisible characteristics that has enabled new ways of vegetation monitoring with RS and spectroscopy methodologies. This transformed knowledge that combines multiple parts of the reflectance spectrum and indices generation has allowed an unprecedented knowledge burst about plants, their status, science and derivative practices.

Between the far end of the Red part of the spectrum and up until ~800nm extends a narrow characteristic vegetation reflectance band, **the Red-Edge narrow region**. This spectral feature that embodies a very high difference in reflectance values from very low Red to very high NIR is usually determined at 10-70nm wideness depending on the detail available at the instrumentation and the number of bands at this portion of the spectrum, allowing the possible differentiation between species and their status. Sampling at 10nm intervals is considered best practice for rather wide band spectroscopy. The red-edge has been extensively studied and has provided a robust indication of chlorophyll content, LAI and nitrogen status among others. Changes in chlorophyll concentration result in a Red-Edge shift. High chlorophyll increases absorption in the red region and pushes the Red-Edge to longer wavelengths in the NIR.

Entering the **NIR part of the spectrum (700-1100 nm),** the reflectance of vegetation is indicatively high. This characteristic is explained by the fact that NIR radiation energy is almost useless to vegetation and plants, it is not absorbed and thus most is reflected and transmitted. As expected, different leaf and cell structures reflect and scatter NIR radiation in different ways, however keeping this characteristic common throughout all vegetation species. In regard to plants like vines that have multiple layers of leaves and a dense canopy, the additive effect results in very high portions of NIR reflectance.

In the **Shortwave Infrared (SWIR) region (1100-2500 nm),** the overall vegetation reflectance in relatively low while the main characteristic is the strong water absorption features at specific portions of the spectrum. Water content in the plant tissue causes relatively high reflectance when the plant is growing and healthy, while the overall reflectance in this region decreases with the decline of the plant. Biochemical substances absorbing radiation in this part are cellulose, sugar, nitrogen and others, however they are hardly detectable in fresh vegetation due to water concentrations that obscure and decrease the overall reflectance.

Cellular water in vegetation absorbs highly at wavelengths and energy levels beyond the visible spectrum. Vegetation maintains a **thermal balance** through convection and evaporation, dissipating energy into the environment. Those processes are mainly dependent on leaf size, shape and stomatal opening/closure control. Absorbing radiation along with the biological processes result in the production of thermal energy and the consequent release of water vapor to the atmosphere through leaves' stomata (aquatic plants are not under consideration as they do not have stomata) because of their conductance and vapor pressure deficit. This loss of water is called **transpiration**, a process that cools the plants. Plants cannot gain carbon dioxide for photosynthesis without simultaneously losing water vapor as carbon dioxide enters the plants through the same stomata from which they simultaneously lose water vapor. Transpiration derived loss of water results in higher concentration of solutes in cells

and a drop of water pressure in plants' cells transporting water from areas of higher concentration (from soil to roots, stems and leaves) back to the cells in an exemplary hydraulic procedure.

Pathogen stressed plants (by e.g. fungi, foliar bacterial plant pathogens) may result in **internal heat accumulation and a rise in canopy temperature** (Gudesblat et al., 2009; Melotto et al., 2008). The plant's stomata are forced to close, ceasing to transpire, while pathogen ruptured epidermis is causing water loss. This translates into less carbon dioxide diffusion, photosynthesis disruption and the deterioration of the plant's health and growth, interfering with protein and later chlorophyll synthesis (Reddy and Zhao, 2005). As a result, in **the Thermal Infrared (TIR) domain (6-14 μm)** valuable knowledge can be extracted mainly by the radiation emitted from the leaves epidermal materials and the transpiration process deriving from leaf water content. Additionally TIR is sensitive and provides accurate results in regard to vegetation water stress, as the lack of water means that vegetation cannot lose heat with transpiration, raising its temperature. Overall, TIR provides insight to vegetation stress from water and other factors, gas exchange monitoring by stomatal responses (transpiration rate) and soil moisture content.

2.3   State of the Art Review

The quality and amount of discrete layers of knowledge from the reflected and emitted radiation captured by RS instruments is always the limiting factor in vegetation monitoring along with the computational and algorithmic robustness for the processing of the data.

In the current study broadband sensors have been used from space-borne and airborne observational platforms specifically designed for vegetation monitoring and utilized in relevant methodologies on full scale scientific and commercial applications for PA and PV globally.

Indicatively, the G20 Ministerial Declaration launched the Group on Earth Observations Global Agricultural Monitoring (GEOGLAM[4]) initiative in June 2011, with the aim "*of strengthening GLobal Agricultural Monitoring by improving the use of remote sensing tools for crop production projections and weather forecasting*". In the context of GEOGLAM, the Joint Experiment of Crop Assessment and Monitoring (JECAM[5]) initiative has utilized in multiple test sites around the world the observational platforms of the Sentinels missions, Landsat, Radarsat and other satellite missions, UASs with multispectral and thermal payloads among others, while complementing and validating with in situ components. In the recent years a wide range of activities promoting EO as a key enabler for smart, sustainable agriculture have been launched. These range from European Union (EU) projects (e.g. APOLLO[6], FATIMA[7]), to Public–Private Partnership (PPP) schemes (e.g. EIP-AGRI[8]), European Space

---

Agency (ESA)-funded projects (e.g. the Food Thematic Exploitation Platform, Sentinel-2 for Agriculture[9]) and large-scale demonstrators under the IoF2020[10].

In general, the collection of data from remote sensing platforms has considerable potential. Numerous studies have been undertaken using both airborne and satellite remote sensing platforms and sensors, including studies using optical and thermal -multispectral and hyperspectral-, Lidar and Radar sensors.

Inspecting the State-of-the-Art in the sector of Precision Agriculture and Precision Viticulture, there are **multiple inter-dependable and connected advancements** in multiple scientific and commercial procedure layers.

Methodological scientific advancements and tendencies today are driving the **technological** progress while provoking its further development, driven by applications and needs. In the same time, this technological expansion and huge **data surge** motivates and drives the relevant expanse of the scientific and commercial methodologies utilized for RS observational platforms in the scope of PA and PV.

State-of-the-art **optical and thermal multispectral and hyperspectral sensors** have been engineered in the recent years that provide reflectance and emittance data in hundreds of portions throughout the observed electromagnetic spectrum, allowing the construction of hundreds of Vegetation Indices, detailed and plant-specific discriminating responses to radiation, spectral signatures, variations and features recognition (Borengasser et al., 2007) among other products (Broge and Leblanc, 2001; Dalal and Henry, 1986; Datt et al., 2003; Filella et al., 1995; Franke and Menz, 2007; Gomez et al., 2008; Guanter et al., 2005; Haboudane et al., 2004; Haboudane et al., 2002; Hansen and Schjoerring, 2003; Peña-Barragán et al., 2011; Rao et al., 2008; Rao et al., 2007; Rao, 2008; Thenkabail et al., 2004; Thenkabail et al., 2013; Thenkabail et al., 2000; Thenkabail et al., 2002).

Synthetic Aperture Radars (SAR) are exquisitely used for crop monitoring allowing the estimation of biomass, leaf area index, multiple phenotypical features extraction and other useful knowledge like growth rates and yields (Antropov et al., 2011; Arii et al., 2010; Arii et al., 2011; Ballester-Berman and Lopez-Sanchez, 2010; Ballester-Berman et al., 2013; Baup et al., 2016; Burini et al., 2008; Campos-Taberner et al., 2017; Charbonneau et al., 2010; Cloude and Papathanassiou, 1999; Cloude, 2009; Cloude and Pottier, 1997; David Ballester-Berman et al., 2012; Dubois et al., 1995; Feng Xu and Ya-Qiu Jin, 2005; Fisette et al., 2013; Freeman and Durden, 1998; Freeman, 2007; Gherboudj et al., 2011; Hajnsek et al., 2003; Hajnsek et al., 2009; Jagdhuber et al., 2013; Jong-Sen Lee et al., 2000; Lee et al., 2014; Lee and Ainsworth, 2011; Liang et al., 2009; Loew et al., 2006; Lopez-Sanchez et al., 2012; Loussert et al., 2016; Mansaray et al., 2017; Mattia et al., 1997; McNairn et al., 2014; McNairn et al., 2009; McNairn and Shang, 2016; Merzouki et al., 2010; Moran, 1997; Oh et al., 1992; Papoutsis et al., 2017; Prasad et al., 2009; Singh et al., 2009; Song et al., 2010; Srivastava et al., 2009; Steele-Dunne et al., 2017; Topp et al., 1980; Treuhaft et al., 2011; Truong-Loi et al., 2009; van Zyl et al., 2011; Villa et al., 2015; Wang et al., 1998; Wentao An et al., 2010; Yamaguchi et al., 2005; Yi Cui et al., 2014)

---

[9] http://www.esa-sen2agri.org/SitePages/Home.aspx
[10] http://cordis.europa.eu/project/rcn/206761_en.html

All these active or passive sensors are **both air- and space-borne** enabling the monitoring of vegetation throughout the electromagnetic spectra in all different spatial, temporal, spectral and radiometric resolutions, tailored to the specific needs for vegetation, soil and low altitude atmosphere monitoring. Depending on the **observational platforms' capacities**, different layers of knowledge can be extracted serving different or common needs.

Depending and constrained by costs, politics and priorities, EO platforms, especially space-borne, can provide very different products. For example under the current reality, state-of-the-art constellations of very high spatial resolution satellites (e.g. 30cm pixel size) that carry multispectral optical instruments and can cover each part of the Earth every day is under discussion and preparations, designed to deliver huge volumes of very useful data on vegetation monitoring. However it is still really expensive and complicated both for manufacturing and maintenance, keeping the needed scientific high quality of the products delivered. On the other hand a smaller, state-of-the-art EO satellite constellation with hyperspectral optical payloads that can provide data over every part of the Earth every two weeks is again extremely useful for science and applications. An enlightening example of a full scale satellite EO constellation is the initiated SuperView-1 constellation from China consisting of 16 optical satellites with 0.5m resolution, 4 satellites with resolution better than 0.5m, 4 VHR X-band SAR satellites and multiple micro video and hyperspectral satellites once fully assembled in space[11].

For satellite EO platforms, **tradeoffs** between costs, volumes, data availability, data quality and resolutions, the temporal dimension, instrumentation dedicated functions, longevity and mission plan and many other factors determine the exercised state-of-the-art nowadays, as the real capabilities in technology and applications are huge.

In regard to PA and PV the current capacities in multispectral and hyperspectral optical and thermal monitoring of a vineyard can be exercised daily from space even through video products, while computational capacities to process such volumes of data can be provided with high efficiency. However this is one of the real challenges scientifically examined. Big, gargantuan data should be redefined with methodologies that demand and have the ability to extract smart data: the most competent knowledge in the highest detail possible.

Information extraction from hyperspectral and multispectral image datasets –both optical and thermal- are numerous and ever-evolving. Pixel- and object-based classification techniques based on statistical analysis (Kalouptsidis et al., 2007), neural networks and deep learning (Hu et al., 2015) and many others (Bioucas-Dias et al., 2012; Courty et al., 2012; Fauvel et al., 2013; Iordache et al., 2012; Li et al., 2012) have been developed and published. Spectral Unmixing for sub-pixel level information (Chang, 2013), anomaly detection (Matteoli et al., 2014; Nasrabadi, 2014), spectral matching and labeling by comparing spectral signatures with spectral libraries (Thenkabail et al., 2002; Thenkabail et al., 2004; Thenkabail and Lyon, 2016), spectroscopy for quantifying the relation between the spectrum of an object and a parameter (Choe et al., 2008), change detection through temporal analysis with various methods (Camps-Valls and Bruzzone, 2009; Ghosh et al., 2013; Pratola et al., 2013; Singh et al., 2014) are methodological tools and processes for knowledge extraction and machine learning techniques for

---

[11] https://www.geospatialworld.net/news/china-launches-two-multi-sensor-high-resolution-remote-sensing-satellites/

campaign derived (UAS) or multi-temporal (satellite) analysis of hyperspectral and multispectral data from optical and thermal sensors.

In regard to **UAS state-of-the-art**, it has to be mentioned that the technological and methodological limits are the generic avionics limits. For example, fixed wing Unmanned Aircraft Systems can cross oceans and continents by sophisticated avionics designs and multiple redundant GNSS, flight stability and control systems, power consumption optimization even with solar panels and miniaturized RS technology, controlled and monitored automatically under specific flight plans or under live coverage from satellite telecommunications. The constraints and limitations of UAS observational platforms (balloons included) are dependent on each specific system, its purpose, cost and capacities. VTOL (Vertical Take-Off and Landing) multirotor drones are cheaper than fixed-wing ones in general and much easier to land and take-off, however they need much more power and battery capacity for surveying the same area compared to the very low consumption due to the aerodynamics of the Fixed-Wing drones.

The payloads on board a UAV are limited by the platform capacity in power consumption and maximum weight depending on power, structural, aerodynamics and mission specific properties. For example, a robust UAV that operates in higher altitudes for e.g. 8 hours that can lift up to 20kg payload at full maneuvers and speed capacity to withstand extreme weather phenomena and winds, can even operate with a Radar or multiple optical instruments. Today, the most cost-effective and well established UASs are the VTOL multirotor ones that operate easily in any altitude, safely in the operators line of sight, with very small but highly efficient multi- and hyperspectral optical, thermal payloads, Lidars etc., with limited surveying capacity due to power consumption, but with the flexibility of engineering a suitable multistep flight plan.

The mass production of UASs, the expanse of EO satellite constellations like the Sentinel missions and nanosatellites equipped with optical instruments of great complexity and capabilities and huge networks of cost effective in-situ sensors backed by Internet of Things (IoT) information grids, at least promise the dawn of a new epoch on agricultural knowledge, practices and effective multidisciplinary methodologies for smart and sustainable farming all around the globe.

Summarizing, **Remote Sensing for agriculture is a solution looking for a problem**.

3 Methods and Data

3.1 Observational Platforms

3.1.1 Sentinel satellites

The European Space Agency has designed and implemented a series of satellite missions, a constellation of supplementing payloads, with the corresponding in-land infrastructure, that will support numerous EO objectives covering in high resolutions the whole globe for the **Copernicus program** needs. Those missions are providing data under open and free policy (Harris and Baumann, 2015) and distribution to any interested party under simple registration to the Copernicus Sentinel Hub. All high resolution Copernicus Sentinel satellite stills and animations processed by ESA are released under the Open Access compliant Creative Commons CC BY-SA 3.0 IGO license[12]. In Greece, the National Observatory of Athens (NOA) has developed and introduced to the public the Hellenic Sentinel Data Mirror Site (HNSDMS)[13] providing to the eastern European countries and northern Africa the first mirror node for Sentinel products and data access.

In the current perspective of land monitoring, the sub-constellation of Sentinel-2A and 2B (Sentinel-2B has been launched at the 7th of March 2017, proven operational and undertaking calibration and validation processes before public use) will be exploited.

Sentinel-2 (S2) satellites are launched into a sun-synchronous orbit at 786 km, inclination = 98.5º, (14+3/10 revolutions/day) with 10:30 hours Local Time at Descending Node (LTDN). This local time has been selected as the best compromise between cloud cover minimization and sun illumination. S2 delivers a 290 km swath promising a revisit time of approximately 5 days and about 10 days for delivering cloud-free imagery under the same viewing angles. The S2 missions are carrying the MSI payload which records radiation at 13 discrete bands of the electromagnetic spectrum (**Table 1**), spectral channels in the visible near infrared (VNIR) and SWIR range. The main objectives of the S2 missions are land, agriculture, inland water and hazards monitoring[14]. The radiometric resolution of the MSI instrument is 12 bits, enabling the image to be acquired over a range of 0 to 4.095 potential light intensity values.

In respect to the spatial resolutions of those bands, 4 are at 10meters, 6 at 20m and 3 at 60m covering specific needs mostly dedicated to agriculture, forestry and water observation. The overall design has been engineered to provide continuity to present and past EO satellite missions and according to extensive scientific pre-production theory, RS practices and in-situ measurements.

---

[12] http://open.esa.int/copernicus-sentinel-satellite-imagery-under-open-licence/
[13] https://sentinels.space.noa.gr/dhus/#/home
[14] Sentinel-2 Preparatory Symposium Abstract Book, 23-27 April 2012, ESA-ESRIN, Frascati (Rome), Italy

Sentinel-2 Bands	Resolution (m)	Bandwidth (nm)	Central wavelength (nm)
Band 1 - Coastal aerosol	60	20	443
Band 2 - Blue	10	65	490
Band 3 - Green	10	35	560
Band 4 - Red	10	30	665
Band 5 - Vegetation Red Edge	20	15	705
Band 6 - Vegetation Red Edge	20	15	740
Band 7 - Vegetation Red Edge	20	20	783
Band 8 - NIR	10	115	842
Band 8A - Vegetation Red Edge	20	20	865
Band 9 - Water vapour	60	20	945
Band 10 - SWIR - Cirrus	60	30	1375
Band 11 - SWIR	20	90	1610
Band 12 - SWIR	20	180	2190

Table 1: Sentinel-2A MSI specifications [15] [16]

The image products of S2 released for public use and processed in the current project are Level-1C (L1C) which are products after multiple thorough transformations, interpolations and corrections in the Level-1A (L1A) and Level-1B (L1B) products from the Copernicus ground segment[17]. The L1C products present the top of the atmosphere (TOA) reflectance values for each band in fixed cartographic geometry (combined Universal Transverse Mercator (UTM) projection and WGS84 ellipsoid) along with applied radiometric and geometric corrections (including orthorectification and spatial registration). Every MSI L1C granule (or tile) covers an area of 100x100 km^2.

However, TOA products and their radiometric measurements transformed to reflectance values, are subject to the **atmospheric media**. Several physical factors complicate the quality of the remote sensed information. Atmospheric particles (aerosols) distortions, gases like ozone and carbon dioxide, thin clouds, water vapor and the sun position effects absorb and scatter radiation, meaning intensity reduction and direction alteration respectably. These attenuation factors to sun radiation towards the Earth and upwards to the sensor comprise the MSI sensor's final input that will be transmitted to the Earth stations.

Those distortions create the effect of "haziness" to the final products reducing the overall contrast and the "adjacency effect" which describes the interference of scattered radiation from neighboring pixels to any given pixel itself.

L1C products are published without considering these effects, as for multiple applications, those are trivial. However, for vegetation status monitoring and accurate results, it is good practice to perform atmospheric corrections to the S2 products before any further processing towards vegetation indices generation and consequent knowledge extraction. Numerous studies have been published highlighting

---

[15] https://earth.esa.int/web/sentinel/user-guides/sentinel-2-msi/resolutions/spatial
[16] https://sentinel.esa.int/web/sentinel/user-guides/sentinel-2-msi/resolutions/radiometric
[17] https://sentinel.esa.int/web/sentinel/technical-guides/sentinel-2-msi/level-1c/algorithm

the disruptive factors of media conditions like the atmospheric water vapor and aerosols contamination which lowers the NIR response accuracy of MODIS-NDVI sensor (Huete et al., 2002).

It should be underlined that S2 L1C data are reflectance products and not radiance. This is a transformation taking into account the TOA radiance (up-welling radiation), the sun irradiance (down-welling radiation reaching the Earth from the sun, depending on their distance) and the sun zenith angle. By transforming spectral radiance to reflectance (reflectance represents the ratio of radiance to irradiance thus providing a standardized measure directly comparable between images), delivered MSI data are independent of the degree of illumination of the Earth objects which depends on factors like time, season and latitude.

In addition, apart from the usefulness of reflectance products, it should be mentioned that remote sensed radiance is highly valuable considering the construction of observed objects' spectral signatures and the compilation of spectral libraries. In the same manner, radiation attenuation and distortion at the sensor as described above should be taken into serious consideration in order to extract valuable and consistent knowledge and corresponding spectral libraries. S2 L1B products provide TOA radiances in sensor geometry.

Multiple methodologies for atmospheric correction and removal of atmospheric effects exist for S2 MSI (Lantzanakis et al. 2017). **S2 Level2A (L2A)** products transform L1C data TOA reflectance values to bottom of the atmosphere (BOA) reflectance values by performing atmospheric correction algorithms. The final L2A product granule covers an area of 100x100 km^2 like the original L1C. Today, the efforts by ESA to remove the burden of atmospheric correction from the user have been successful delivering the first thousands of S2 L2A products from the Copernicus S2 DataHub, while other organizations like the Theia Land Data Center and the French Centre National d'Études Spatiales (CNES) have already been providing S2 L2A imagery for multiple areas around Earth using the Multi-sensor Atmospheric Correction and Cloud Screening (MACCS) software, currently expanding their portfolio to cover all existing S2 products.

As the overall results of different algorithms in the atmospheric correction endeavor show little differentiations, the official methodology from ESA has been performed in order to acquire S2 L2A products.

Describing in detail and explaining the atmospheric correction algorithms is not part of the current study[18]. ESA's L2A algorithm (developed by DLR/Telespazio, **Figure 5**) is based on an algorithm proposed in Atmospheric/Topographic Correction for Satellite Imagery (ATCOR; Richter and Schlaepfer, 2011), which performs atmospheric correction based on the LIBRADTRAN radiative transfer model (Mayer and Kylling, 2005) using a database of look-up tables (generated for a wide variety of atmospheric conditions, solar geometries, and ground elevations, calculated with a high spectral resolution of 0.6 nm) compiled using the freely available software library called libRadtran1. This database is resampled using the S2 spectral responses, in order to obtain the sensor-specific functions needed for the atmospheric correction, i.e. path radiance, direct and diffuse transmittances, direct and diffuse solar fluxes, and spherical albedo.

---

[18] https://sentinel.esa.int/web/sentinel/technical-guides/sentinel-2-msi/level-2a/algorithm

The overall performance of the atmospheric correction algorithm, classification processes and masks construction is competent and the results are visible to the human eye at a glance, even if there is no available information on the bidirectional reflectance behavior of surfaces, and thus a simple isotropic (Lambert) reflectance law is assumed.
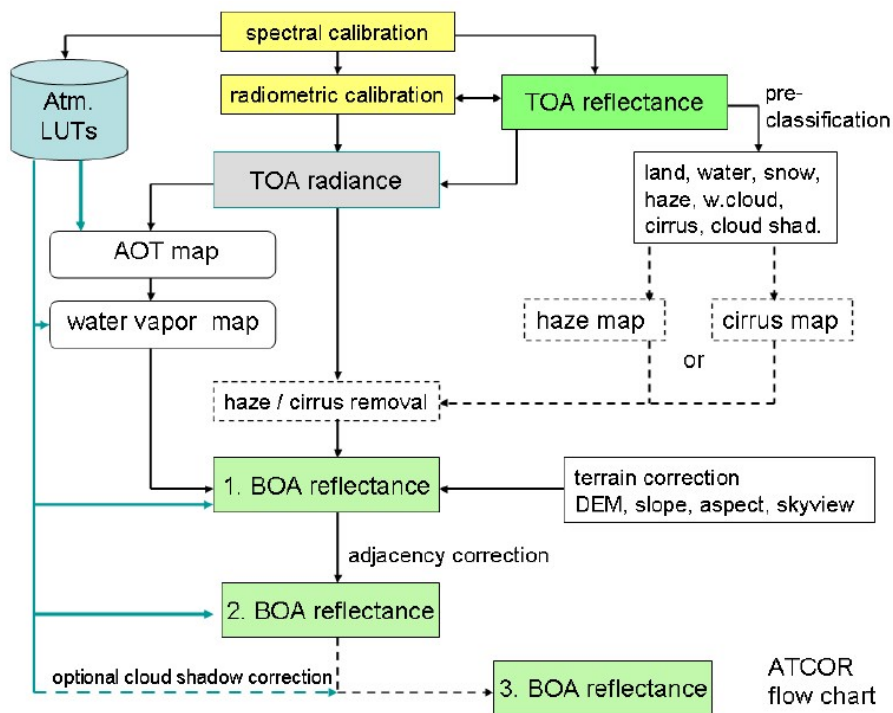

Figure 5 : Atmospheric correction processing steps[19]

The technical process includes the open source SNAP tool provided by ESA and Copernicus using the S2 toolbox and the "sen2cor" SNAP plugin. The consequent L2A products provide the BOA reflectance values that can be used to extract useful and corrected knowledge for vegetation and land condition (**Figure 6, Figure 7**). In the current experiment 10m products have been constructed, meaning that the intermediate processes have fabricated the 60m and 20m products as well. All those bands are needed for the vegetation indices composing.

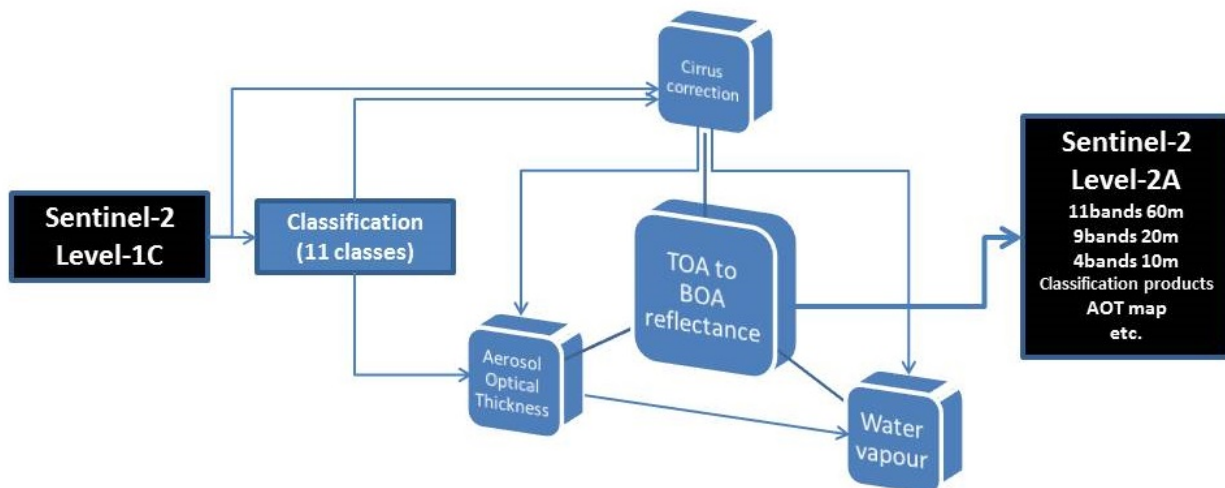[19] Sentinel-2 MSI – Level 2A Products Algorithm Theoretical Basis Document

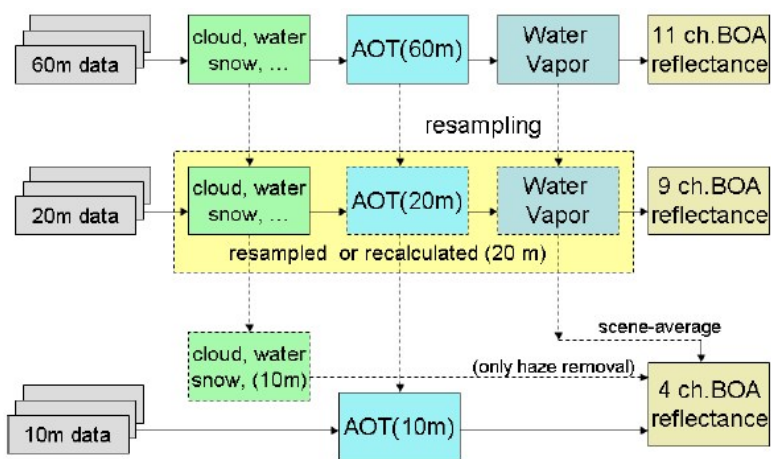**Figure 6 : Overview of the transformation from L1C to L2A S2 products**

Figure 7 : Overview of the L2A algorithm products[20]

---

[20] Sentinel-2 MSI – Level 2A Products Algorithm Theoretical Basis Document

3.1.2 Unmanned Aircraft Systems

In the recent years, technological advances have been excessively trying to reduce the size and mobility of electronic parts while keeping or upgrading their efficiency. One of the most prominent technological successes are mobile phones with capabilities met only in highly advanced computers in the past decade. Today's smartphones embed a series of state-of-the-art technologies including highly accurate GNSS receivers from the American Global Positioning System (GPS), EU's Galileo/EGNOS, Russia's GLONASS to China's BeiDou and possibly regional constellations. Especially in Europe, awaiting on the full operational capability of the EU Galileo GNSS, and thanks to EGNOS Satellite-based augmentation systems (SBAS), the free, non-military USA GPS accuracy is improved from 17 meters without EGNOS to about 3 meters, which is a remarkable achievement.

A literal analog to everyday smartphones and their tremendous capabilities has been the blooming of **Unmanned Aerial Vehicles (UAVs),** better described as **Unmanned Aircraft Systems (UASs)** or **Remotely Piloted Aircraft Systems (RPASs)** or simply **"drones"**. The analogy consists in the fact that a UAS could be naively described as a flying smartphone dedicated to specific functions. Instead of the smartphones numerous functionalities, a UAS has specific components that enable its performance and control.

UAS is the preferable conditional term for drones as it embodies the ground segment as well. UASs have been extensively used in PA and of course PV since the beginning of the 21st century (Lamb, 2000; Lamb et al., 2011).

The development and rapid expansion of UASs is being followed by a delayed and insufficient **regulatory scheme** all around the globe. Even if laws and regulations have been established in multiple countries in the recent years only, it has been widely observed that they are inadequate to maintain a balanced and well defined area of operational status for UASs. These existent regulations cannot be considered either complete nor fixed for the consequent changes that UAS mass production and availability will impose on many aspects of scientific, professional or everyday use in modern society. By the end of 2017 and the following years, a more robust and centralized regulatory framework is expected to be published and nationally implemented.

The diversity of national and regional UAS directives and the lack of common policy is currently the source of multiple implications on operational services. For example, Cuba, Egypt and Uzbekistan are countries that totally ban UAS deployment of any kind. By October 2016, 99 countries around the globe have no rules at all concerning UASs, 65 have regulations in place and 15 countries have regulations in pending condition (Stöcker et al. 2017). Many EU countries have implemented risk and usage oriented frameworks for UAS deployment mainly depending on weight and visual or beyond-visual contact operations. Additionally UAS flights are obliged to no-flight zones, altitude limits, operation area limits from ground station, remote flight certificate ownership, official training and more.

In general, the regulatory framework, laws and guides regarding UASs at national and international level are the subjects of the individual country aviation organizations, the European Aviation Safety Agency (EASA), the US Federal Aviation Administration (FAA), the UN International Civil Aviation Organization

(ICAO) regulations and others. Any UAS is subject to all of those regulatory laws and specifications depending on jurisdiction and local enforcement maturity/practices while fundamentally ensuring and protecting public privacy and safety as well as the environment[21].

In regard to the **Greek national UAS regulations framework**[22], the Hellenic Civil Aviation Authority has published the specifications and regulations in regard to the relative laws from 2016. A dedicated platform for pilots/UASs registration and certification purposes as well as flight missions reporting for audit and permission have been developed and made available for public use.

The **UAS used in the current study** is a multicopter -specifically a **hexacopter**- along with its **payloads** and the **ground segment** (**Figure 8**). The assembled UAS has been designed in order to provide flight and payload capacities in regard to its primary objective: Depict and monitor agricultural land while remaining within the national and international regulatory framework.

UAV type	Hexacopter – DJI S900 skeleton
Payload max weight	4 kilograms + battery
Endurance (without payloads)	30 minutes
Endurance with current payloads	20 minutes
Max Speed (no payloads)	16 m/s
Max altitude	6000 m

Table 2: UAV main specifications

The hexacopter's avionics "brain" setup is the most reliable and sophisticated, open source **autopilot** system Pixhawk 2.1 with an integrated single board flight controller and sufficient I/O for multiple instruments. It exhibits triple redundant Inertial Measurement Units (**IMUs**), and the capability to use up to 3 GNSS modules. The IMU is the inertial navigation system of the UAV allowing the computer to track the craft's position and state by measuring its specific force, angular rate, surrounding magnetic field, pressure and other physical parameters. the IMU integration with GNSS receivers provides the system with dead reckoning capability allowing it to track position while measuring speed, acceleration, inclination, flight position (pitch/roll/yaw movements) among others. The Pixhawk 2.1 IMU has a total of 29 Micro-Electro-Mechanical-Systems (**MEMS**) sensors for redundancy and navigation robustness: 3 triple axis accelerometers, 3 triple axis gyroscopes, 3 triple axis magnetometers and 2 barometers. The autopilot has been configured and programmed with all the necessary utilization procedures, safety measures and operational details in regard to its components and the ground segment.

Connected to the autopilot are the **GNSS receiver, Lidar, the UAS mainframe servos, 6 electric brushless motors with corresponding electronic speed controllers and 2 telemetry modules**.

- The **GNSS receiver** exhibits highly sophisticated characteristics with industry leading -167dBm navigation sensitivity, concurrent reception of up to 3 GNSS (from GPS, Galileo, GLONASS,

---

[21] The comparative collections of UAV regulations can be found in detail in online detailed frameworks like ERSG, EUROCONTROL, JARUS, UVS International, dronerules.eu and others, however usually outdated or incomplete.
[22] http://www.ypa.gr/userfiles/fa3cb89c-ac1a-4d4b-99ab-a34f011804e1/document%20(2)%20%CE%A6%CE%95%CE%9A-30-9-2016.pdf

BeiDou), security and integrity protection, advanced jamming and spoofing detection and two temperature compensated three-axis integrated circuit magnetometers (digital compasses).

- The **Lidar** is a lightweight laser rangefinder for precision hovering, anti-collision and Above Ground Level (AGL) landing assisting purposes.
- The **telemetry modules** are dedicated to the ground segment. One pair for the electronic device (smartphone, tablet or laptop) with the highly sophisticated open-source software **Mission Planner** which was used in the current project, and one pair for the 2.4Ghz Radio Controller which has been programmed internally defining its functionality and safety precautions.

Figure 8: The UAS with payloads and 2 instances of Mission Planner after two flights

The basic avionics needed for flight control and the **management of image datasets generated** as accurate measurements from the autopilot are GNSS readings, the pitch, roll and yaw aircraft positions and the time (**Figure 9**).
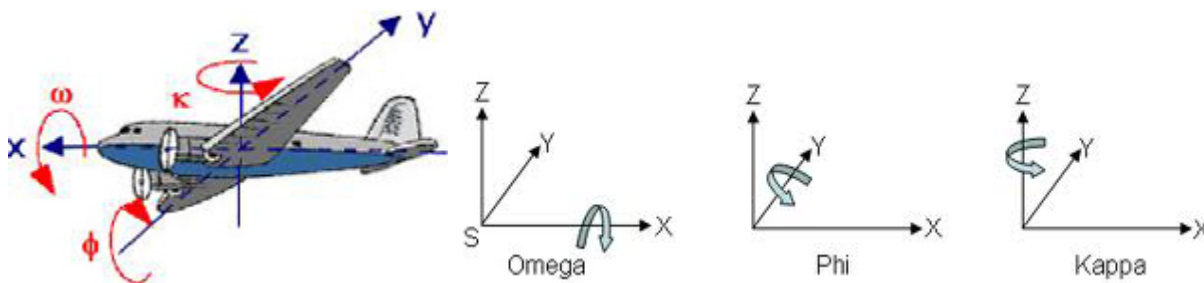
UAS	Image data
Time (Time and position XYZ)	Time of acquisition
Position XYZ	Position XYZ
Roll	Omega
Pitch	Phi
Yaw	Kappa

Figure 9: Avionics and image properties for photogrammetric reasons

3.2 UAV payloads

3.2.1 Parrot SEQUOIA Multispectral camera

The multispectral camera mounted on the UAV that best fits the agricultural operations in terms of specifications, utilities and cost effectiveness is the Parrot Sequoia. Sequoia exhibits a series of state-of-the-art components, designed primarily for agricultural and vegetation monitoring applications. It is easy to use, with outstanding precision while being light-weighted (107 grams total) and miniaturized (Body: 59mm x 41mm x 28mm; Sunshine sensor: 47mm x 39.6mm x 18.5mm).

In the different parts of the electromagnetic spectrum **Sequoia has a total of 5 sensors**: One panchromatic RGB sensor at 16Megapixels (Mpx) and 4 narrow band, synchronized 1.2Mpx monochrome sensors at the Green, Red, Red Edge and NIR parts. In more detail, the panchromatic and monochromatic sensors exhibit the following specifications shown in **Table 3**.

Panchromatic	Monochromatic
Focal Length 4.9 mm	Focal Length: 4.0 mm
Imager resolution: 4608 x 3456 pixels	Imager resolution: 1280 x 960 pixels
Imager size: 6.2 mm x 4.6 mm	Imager size: 4.8mm x 3.6mm
Horizontal Field of View (FOV) : 63.9°	Horizontal FOV: 70.6°
Vertical FOV: 50.1°	Vertical FOV: 52.6°
Dual FOV: 73.5°	Dual FOV: 89.6°

Table 3: SEQUOIA sensor optical specifications

Sequoia uses **Global shutter** for the four bands. In global shutter mode, all of the pixels on the sensor begin collecting charge simultaneously. For the RGB Camera it uses Rolling shutter. In Rolling Shutter mode the pixels are collected row by row, allowing a higher definition of the imagery.

The camera additionally features an **IMU**, a **magnetometer** and **WiFi interface**. The sensors input are automatically calibrated thanks to the sunshine module on top of the UAV, thus making it possible to compare photos over time, despite variations in light during photo shoots. This sunshine module integrates a **GNSS receiver** to locate the camera when photos are being taken and geotag them while storing them in a detachable **SD card** and **4 ambient light sensors** fitted with band-pass filters identical to those on the multispectral sensor.

The SEQUOIA multispectral sensors have been designed mainly for agricultural purposes. The Green, Red, Red-Edge and NIR sensors at vegetation-specific spectral bands have been proven by extensive studies and utilization to best serve in the observation of plants due to vegetation spectral emission characteristics. For the same vegetation characteristics exploitation, the corresponding Sentinel-2 MSI sensors have been designed and implemented in similar electromagnetic wavelength portions, with similar bandwidths. This similarity is shown in **Table 4**.

PARROT SEQUOIA					
Sensor	Green	Red	Red-edge	Near infrared	RGB
Bandwidth (nm)	40	40	10	40	
Central wavelength (nm)	550	660	735	790	
Definition (Mpx)	1.2	1.2	1.2	1.2	16
SENTINEL-2					
Bands	Band 3 - Green	Band 4 - Red	Band 6 - Red Edge	Band 8 - NIR	
Bandwidth (nm)	35	30	15	115	
Central wavelength (nm)	560	665	740	842	
Resolution (m)	10	10	20	10	

Table 4: Parrot Sequoia and respective Sentinel-2 sensor spectral specifications

Apart from the sunshine module and its internal calibrating process for each photo, to create reflectance compensated outputs for each flight, the **reflectance calibration panel** is used before and after each flight (**Figure 10**). During post-processing of the imagery taken, these vital readings will guarantee the best results in concern to illumination, time and location as they are also geotagged and contain additional layers of information for the processing software.

Figure 10: Calibration Target and positioning

The optical instrumentation details and internal calibration techniques embedded in the SEQUOIA solution cannot be examined under the current approach as it is highly complicated and fragments were very recently made available to the public after extensive requests. Even for the processing

environments used, it is highly complicated to embody those parameters –if possible at all- thus deploying a software dedicated to the support of SEQUOIA among others, **Pix4D**, is recommended.

Multiple parameters for best results should be taken into account when capturing data. Clear sunny days, without clouds, at light overcast times (midday) in order to minimize sun position and illumination changes while avoiding as much as possible shadowing effects and differentiations, favorable wind, enough GNSS satellites and other decisive factors.

3.2.2   Flir Vue Pro R Thermal Infrared camera

Thermal Infrared (TIR) is the part of the electromagnetic spectrum between 3 and 20 μm combining the mid-wavelength and long-wavelength infrared. TIR imagery provides knowledge about the surface temperature and thermal properties of the materials under inspection.
TIR data are usually acquired in Longwave infrared, at the spectral range of 8-14 μm, a portion of the electromagnetic spectrum that includes peak emission areas while being a very good atmospheric window for airborne and space-borne sensors (absorption by water vapor and other gases restrict recording of TIR in two wavelength windows: 0.2-5μm and 8-14μm) (Dash et al., 2002). The solar radiation at this range is almost fully absorbed by surfaces resulting in measurements with little interference from reflected radiation. The sources of heat for the surface of the Earth are the geothermal energy produced by the decay of radioactive elements inside the planet and the solar energy. The latter is much more significant that the geothermal energy which is nearly uniform and does not account at all for the thermal variability in a given TIR image. Solar energy absorbed by the surfaces during daytime depends on the unique physical characteristics of the objects, climatic conditions, clouds and topography.
The variations in **emitted energy** by surface materials are driven by their kinetic temperature and the physical property of emissivity, which describes the efficiency of a surface to emit thermal energy compared to an object capable of totally absorbing and emitting all incident radiation independently of wavelength, a blackbody (emissivity=1). The ratio of the energy emitted by a real surface at a specific temperature to the amount emitted by a blackbody at the same temperature is the formula for emissivity, taking values in reality that never exceed 1, but for most natural materials it varies at values near 1, indicating that they are generally strong emitters (Gaussorgues and Chomet, 2012). Measured emissivity is usually dependent to surface morphology, spectral wavelength, temperature and view angle. Because of its wavelength dependence, an emissivity spectrum can identify materials like the similar functionality of the reflectance spectrum.
In the physical realm, the Stefan-Boltzman Law $E = s * T^4$ (s: constant) gives the total energy being emitted at all wavelengths by the blackbody and the Wien Displacement Law $3 * 10^7 / T$ gives the peak wavelength of the radiation distribution (in Angstroms), explaining how the shift of the peak radiation to shorter wavelengths is inversely proportional to the temperature of the emitting object. Thus, it is easily shown that the hotter the object, the more radiation and the shorter the wavelength of IR light emitted.

In regard to surface materials' kinetic temperature, it does not remain the same during daytime and nighttime and it is differentiated between different materials due to their heat budget and thermal properties, thus giving a spatial variability depicted in TIR data as well. This property includes the material's thermal capacity (how much heat is needed to give a specific rise in temperature), thermal conductivity (transfer of heat by conduction to cooler areas below) and the density of the material (Modest, 2013).

As a result of those physical variabilities of surface materials, in order to decipher thermal data, the thermal properties of the depicted materials should be known, the solar elevation (time of the image acquisition) and the topography of the area.

For **vegetation monitoring** which has a rough surface, the emissivity values are close to unity, as compared to shiny and polished surfaces, thus the radiometric temperature evaluation is easier. Image acquisition and heat sensing of reflective surfaces is highly demanding as the result is distorted by environmental thermal reflection (e.g. reflection of the sky or the sun). Remote temperature sensing needs to address the surface emissivity and reflectivity at the TIR wavelengths of the surfaces depicted. As reflectivity R is relevant to emissivity E by the simplified formula $R = 1 - E$, the reflectivity factor is greatly diminished as the emittance factor has higher values close to unity.

Additionally, a **radiometric measurement** needs to account for atmospheric transmission interference (composition, relative humidity, distance between sensor and surface, strong surface winds), the background sky temperature at the specific time of imagery acquisition and the sensor special characteristics (focus, pixel size, blurring effect), in a highly complicated systemic approach.

The thermal camera used in the current experiment is a state-of-the-art miniaturized radiometric thermal sensor, **Flir Vue Pro R**, designed for numerous applications and very effective for precision agriculture purposes. The sensor is an uncooled VOx Microbolometer with 13mm lens, Field Of View for full sensor digital output at 45°x37° and 640x512 pixel resolution, with measurement accuracy of 5% of the reading. The spectral band in TIR is 7.5-13.5 μm.

The camera has been connected via MAVLink bus with the Pixhawk autopilot at 57600 baud rate, effectively altering the provided cable for the 7pin accessory port in order to geotag the images in WGS84.

For scientific purposes and maximum information extraction, still images are saved in **14-bit TIFF 6.0 format** (alternative option is 8-bit Radiometric JPEG) holding the image data, the basic image properties and the corresponding metadata. As TIFF standard does not cover the metadata needs for IR imagery, but does provide a flexible extension mechanism, every TIFF image has a dedicated EXIF 2.3 (EXchangeable Image File) that contains metadata common between almost all digital cameras holding the digital camera properties and GNSS geolocation, and the XMP 1.0 (Extensible Metadata Platform) that is designed to support custom types of metadata not defined by EXIF (**Figure 11**).
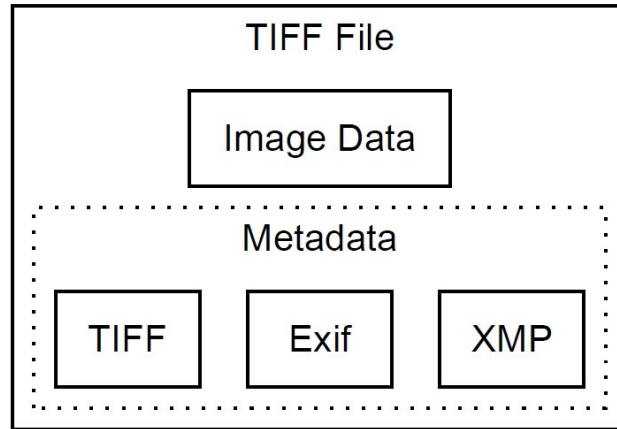
Figure 11: FLIR TIFF with EXIF and XMP extensions

Image settings are optimized for airborne operations by setting the flight altitude, environmental conditions like temperature etc. through FLIR's mobile application for mobile phones, connected via Bluetooth with the camera itself.

Calibration is a vital and most demanding aspect of the thermal cameras. Experiments and calibration techniques that have been implemented in regard to the specific system have shown that blackbody probes in temperatures up to 80°C versus Digital Numbers values (pixel values) has a strong correlation and the internal calibrating mechanism of the camera is quite robust. However, stable readings can be achieved after a warm-up stage of the camera. It has been measured that after 1-1.5 hours the data collection sustains its reliability as Flir Vue Pro R is an uncooled camera. At this point the camera temperature and the internal calibration system reaches a point of stability. The minor disturbances and instabilities caused by the air flow along the UAV flight cannot be accounted for.

For experiment reproduction reasons, the following settings have been configured:

The **scene settings** provide a combination of Automatic Gain Control settings to provide the best image for each particular application. For vegetation monitoring, under some assumptions, the settings used are:

- Region Of Interest (ROI) allows a given percentage of the field of view to affect the image: 100
- Digital Detail Enhancement (DDE) is an algorithm which is used to enhance image details and/or suppress fixed pattern noise: 10
- Active Contrast Enhancement (ACE) provides a contrast adjustment dependent on the relative scene temperature: 3
- Smart Scene Optimization (SSO) value defines the percentage of colors that will be linearly mapped. With SSO enabled at percentage values, the difference in gray shades between two objects is more representative of the difference in temperature. SSO helps to set how linear the Scene algorithms are to provide the highest amount of perceived contrast in every scene : 15

The **radiometric settings** alter the temperature measurement functions depending mainly on the environmental conditions. The ones enabled and set to specific values for the purposes of vegetation monitoring for the pilot vineyard are:

- Temperature Range, which adjusts the camera sensitivity and dynamic range: Auto
- Emissivity, to measure of the target surface ability to emit thermal energy: 98% (Chen, 2015; French et al., 2000; Fuchs and Tanner, 1966; Guoquan and Zhengzhi, 1993; Rubio et al., 1997)
- Air Temperature, sets the ambient temperature of the operating environment: 20°C
- Sky Condition sets the cloud cover conditions above the operating site affecting the background radiation incident on the scene: Clear
- Humidity sets the relative moisture content of the air: Medium (45%)
- Subject Distance : 100m

In agriculture, thermal imaging applications is growing and producing well established results. Irrigation monitoring, plants disease and stress factors detection, yield estimation and maturity evaluation are among others main knowledge extraction features in precision farming through TIR imaging. However, as thermal behavior of vegetation and soil varies according to climatic and environmental conditions, TIR imaging is applicable mainly to site-specific applications and not in a universal manner.

3.3 Data retrieval and methodology

3.3.1 Vegetation Indices

Generally, a ratio or a linear combination of reflectance values mainly in the visible and the NIR parts of the electromagnetic spectrum is termed as a **Vegetation Index (VI)** holding single numerical values as a transformation result (Kriegler et al., 1969; Price and Bausch, 1995).

These indices are used to qualify complex phenomena concerning vegetation that are determined by multiple and highly complex factors.

Hundreds of algebraic combinations of remotely sensed bands have been introduced until today in the last decades, mainly providing empirical evidence and result from reverse engineering of the data used from specific sensors and experiments. This can be described as the harsh reality of remotely sensed physical and biological procedures and quantities that may be discriminated in a well-defined and specific experimental environment but cannot be easily or at all reversely interpreted from spectral reflectance in various spectral bands and RS. In the spatial, temporal and spectral domains, the variabilities in a vegetated area are highly complicated and indicatively compose of plants physiology and leaf structure, water content, age, nutrients, stress factors like parasites (fungi, insects etc.), position/orientation, weather, atmospheric composition, sensor characteristics and calibration and many more (Myneni et al., 1995; Bannari et al., 1995).

However, most of the VIs hold real value to determine vegetation characteristics and provide useful information on almost all scales. Some of the most widely used and successful VIs have been produced in the current context in order to evaluate their performance and useful knowledge included.

3.3.1.1 Normalized Difference Vegetation Index (NDVI)

The most commonly used VI is the Normalized Difference Vegetation Index (NDVI) stated for the first time as the difference, the strong absorption contrast, between the NIR band and the Red band, normalized over the sum of these values, as "this ratio should provide a useful index of the greenness of a vegetation scene" (Rouse et al., 1974). Since this insightful discovery, NDVI has been immensely utilized for almost every application concerning vegetation knowledge extraction in RS in global scale (Hall et al., 2002; Labus et al., 2002; Pettorelli et al., 2005; Trishchenko et al., 2002).

$$NDVI = \frac{R_{NIR} - R_{Red}}{R_{NIR} + R_{Red}}$$

As a normalized entity, the NDVI values range between -1 and +1 with vegetation getting values >0 and soil, water around zero. A most important characteristic is that such a ratio is not influenced by the intensity of the total light reflected from a target. Thus, a target under shadowing effects reflects reduced light across the entire observed spectrum by approximately the same amount. As a result, two

spectrally similar features should produce the same ratio value. Even if this means poorer results for a (ratio induced) VI's output, it maintains the information shadow-free which is an exquisite characteristic when monitoring dense rows of e.g. vines and producing scientific or commercial results.

However, the results embody the underlying soil, a parameter that should be accounted for when correlating NDVI with other characteristics and features. Bare soil reflection is a complex and variable function of soil moisture, organic matter content, composition and its specific optical and physical characteristics (Lillesand et al., 2014).

NDVI increases when NIR reflectance is increased, meaning denser vegetation with more/grown leaves and less soil visibility. NDVI increases also when Red reflectance is decreased in case chlorophyll or/and canopy size is reduced. This of course does not occur during plant growth but in case of hazards, stress and senescence.

3.3.1.2 *Soil Adjusted Vegetation Index (SAVI)*

The well-known NDVI has been found to be decisively influenced by the underlying soil. Soil color, moisture and vegetation can be considered as noisy factors for the NDVI results. In order to provide more robust results in concern to soil and observed plants underlying vegetation, the Soil Adjusted Vegetation Index (SAVI) has been developed minimizing the soil brightness influence to the reflectance derived from Red and NIR wavelengths (Huete, 1988; Lyon et al., 1998).

$$SAVI = (1 + L)\left(\frac{R_{NIR} - R_{Red}}{R_{NIR} + R_{Red + L}}\right), L = 0.5$$

This shift of the origin of reflectance spectra at Red and NIR has been under consideration computing different indices like the Optimized SAVI (OSAVI) (Rondeaux et al., 1996) changing the value of the soil brightness correction factor L to 0.16 and other variations considering the soil, the bands and the instruments used.

In this experiment and for a vineyards specific approach, SAVI has been used in order to demonstrate its potential, however, it has been found to hold little useful information when compared with NDVI or other indices in the current methodology. In the algebraic realm, NDVI and SAVI are part of the same index category, assuming the convergence of vegetation spectra Red-NIR isolines to a single point in the spectral space (with the line of bare soil considered the zero-vegetation line), thus these ratio indices measure the slope of the Red-NIR line between the point of convergence and the Red-NIR point of the pixel (Huete et al., 1984; Kauth and Thomas, 1976). SAVI (1+L) term easily shows that when the adjustment factor is L=0, SAVI reduces to NDVI.

3.3.1.3   Green Normalized Difference Vegetation Index (GNDVI)

Another ratio-based index tested for its usefulness is the Green Normalized Difference Vegetation Index (GNDVI) (Buschmann and Nagel, 1993) found to be well suited for the empirical estimation of plants chlorophyll content and thus their photosynthetic ability using the Green band instead of the Red for reflectance transformation with the NIR (Gitelson and Merzlyak, 1997; Gitelson et al., 1996; Gitelson et al., 2002). The rate of photosynthesis and the chlorophyll content can provide critical information about the crop vitality and stress.

$$GDVI = \frac{R_{NIR} - R_{Green}}{R_{NIR} + R_{Green}}$$

3.3.1.4   NIR/G Green Ratio Vegetation Index (SR_GRVI)

A simple ratio index using the NIR and the Green band is the NIR/G Green Ratio Vegetation Index (SR_GRVI) (Spirada et al., 2006) that has been scarcely used and is currently developed in order to evaluate its potential with the Green band for vineyards. Nitrogen needs and plant growth stages observation has been recognized as its main potential (Miao et al., 2008).

$$Simple\ Ratio\ GRVI = \frac{R_{NIR}}{R_{GREEN}}$$

In regard to its algebraic functionality, SR_GRVI always takes positive values from 0 to infinity which can be a practical disadvantage compared with e.g. NDVI which takes values between -1 and 1. However, it has to be noted that NDVI is essentially a mathematical transformation of a simple spectral ratio NIR/Red, being functionally but not linearly equivalent with it. This is the reason why an index like the Simple Ratio NIR/Red Difference Vegetation Index, Vegetation Index Number (VIN) (Tucker et al., 1979; Bannari et al., 1995) was not examined. The algebraic analogy of GRVI can be examined with GNDVI.

3.3.1.5   Red Edge Chlorophyll Index (CI_RedEdge)

Utilizing the Red Edge band in vegetation indices has provided a very potent and rich environment for vegetation monitoring and status assessment (Clevers and Gitelson, 2013; Delegido et al., 2011; Zarco-Tejada et al., 2005). In this manner two of the most promising indices have been processed within the current experiment, recognized as more sensitive than other indices to changes in leaf chlorophyll.

The Red Edge Chlorophyll Index (CI_RedEdge) has been introduced as a highly formidable index to estimate the canopy and the overall chlorophyll content of plants, an endeavor that is quite complicated as changes in canopy chlorophyll content are obscured by the internal plant architecture, the leaf area index, the underlying soil and other factors. As a result the specific formula has been developed to

deliver trustworthy results in concern to basic crops (Gitelson et al., 2005; Vina et al., 2004). For vines Red Edge bands formulas have been also tested, as chlorophyll content is related to leaf age and net photosynthesis in the leaf (Poni et al., 1994), being an indicator of photosynthetic capacity for grapevine leaves of varying age.

$$CI_{RedEdge} = \frac{R_{NIR}}{R_{RedEdge}} - 1$$

3.3.1.6   Red Edge Normalized Difference Vegetation Index (RENDVI)

Finally, another well performing vegetation index estimating the chlorophyll content and vigor of plants, exercised on vineyards as well (Steele et al., 2008) is the Red Edge Normalized Difference Vegetation Index (RENDVI) or Normalized Difference Red-Edge (NDRE) (Barnes et al., 2000; Gitelson and Merzlyak, 1997; Hunt et al., 2011). Throughout the growing season for vineyards (June and July are vital months in this case) NDRE is more suitable for agricultural management than e.g. NDVI as the red-edge waveband is more sensitive to medium to high levels of chlorophyll content, and hence leaf nitrogen. The construction of a variability map for chlorophyll content, like the CI_RedEdge index and the NDRE, provides valuable information for a precision application of fertilizers or other farming practices. In this case, soil has the lowest values, stressed plants medium values and healthy plants the highest. The vegetation background below the vines and between the lines is well discriminated by the red edge reflectance.

$$NDRE \ or \ RENDVI = \frac{R_{NIR} - R_{RedEdge}}{R_{NIR} + R_{RedEdge}}$$

3.3.2 Photogrammetry and derivatives

3.3.2.1 General principles and the Pix4D software

Photogrammetry can be described as the method, the principles and the optical instruments that are employed in order to generate maps, 3D models and measurements of real world objects. In **aerial photogrammetry** conducted under the current context, the camera payloads are mounted on the UAV and look vertically towards the ground (**Figure 12**).

Photogrammetry relies in the very old concept that the distance between two points that lie on a plane parallel to the photographic image plane, can be determined by measuring their distance on the image, if the scale of the image is known.

Today, for UAS photogrammetry this is described by an Euclidean ground sample distance derived from the payload specifics (field of view, pixel resolution, altitude, shooting angles etc.). In order to determine the scale of a photo one can find the ratio between the camera's focal length and the plane's altitude above the ground being photographed.
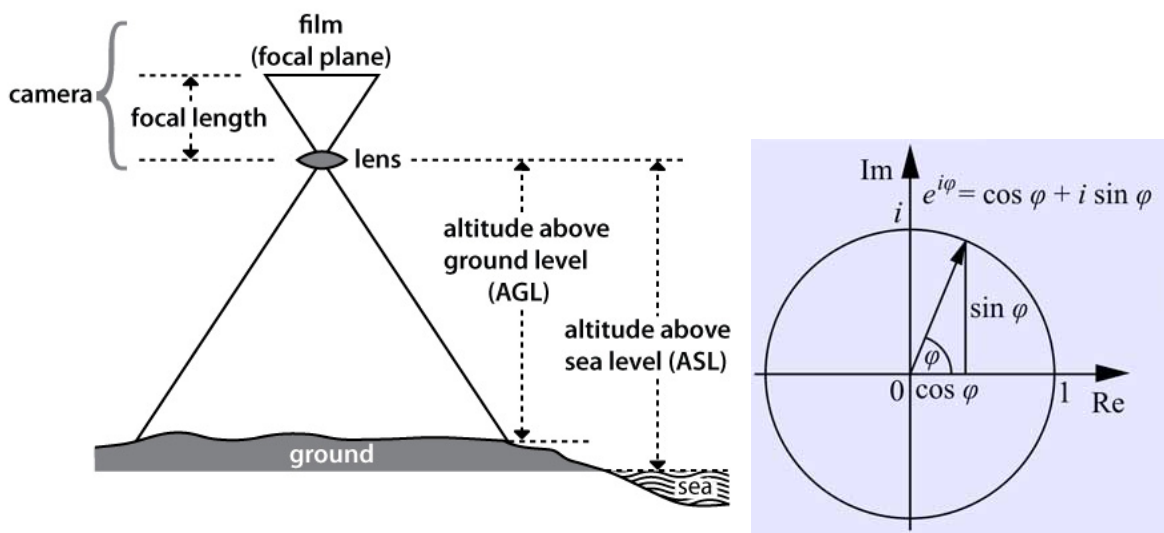
Figure 12: Scale geometry (source: Natural Resources Canada[23])

In the case of aerial photogrammetry in which the exact pitch, roll and yaw positions of the aircraft is known along with its exact geolocation, photogrammetry has been exercised under the label **stereophotogrammetry** as it can estimate the three-dimensional coordinates of points on Earth employing measurements made in two or more photographic images taken from different positions (Maas and Kersten, 1997).

A huge set of aerial photographs integrating in their EXIF the data from the autopilot (camera orientation from aircraft omega, phi and kappa attributes (**Figure 9**), flight altitude, focal length, principal point coordinates, distortions etc.) can be afterwards inserted in a photogrammetric pipeline, a

---

[23] http://www.nrcan.gc.ca/earth-sciences/geomatics/satellite-imagery-air-photos/air-photos/about-aerial-photography/9687

set of procedures that will allow the production of a 3D model representation of elevation data (see next: DSM) and a consistent orthomosaic of the whole area.

In order to produce an **orthomosaic or orthomap**, the images need to be orthorectified. **Orthorectification** is the process of removing the tilt effects from an image in order to create a planimetrically correct image. By this process, the orthorectified image has a constant scale wherein features are represented in their real positions. This process needs the accurate UAS orientation values and the initial production of the 3D model from multiple image stereo pairs. In the recently developed algorithms and image process software, stereo pairs have been advanced to a multiple stereo matching process that using as many inputs of neighboring images as possible to determine and produce a 3D point cloud. This is the reason behind the high overlapping image acquisition and UAS flight engineering. Stereo pairs and multiple stereo matching rely on the aerial triangulation process, which represents the mathematical process, the method of determining the coordinates of points of a terrain on the basis of aerial photographs. The purpose of **aerotriangulation** is to make a geodetic network more dense in order to provide photographs with the control points that are necessary for the compilation of topographic maps and for the solution of various engineering problems[24]. An aerotriangulation solution simultaneously determines the spatial intersection of image rays of a finite point from its position on overlapping photos.

The input data for aerotriangulation are derived from the flight details: photo coordinates, omega, phi and kappa rotation, camera calibration and the digital image dataset (**Figure 13**).

In this process, tie-points are generated by brute algorithms that parse all the images in the dataset and provide robust pairing results.
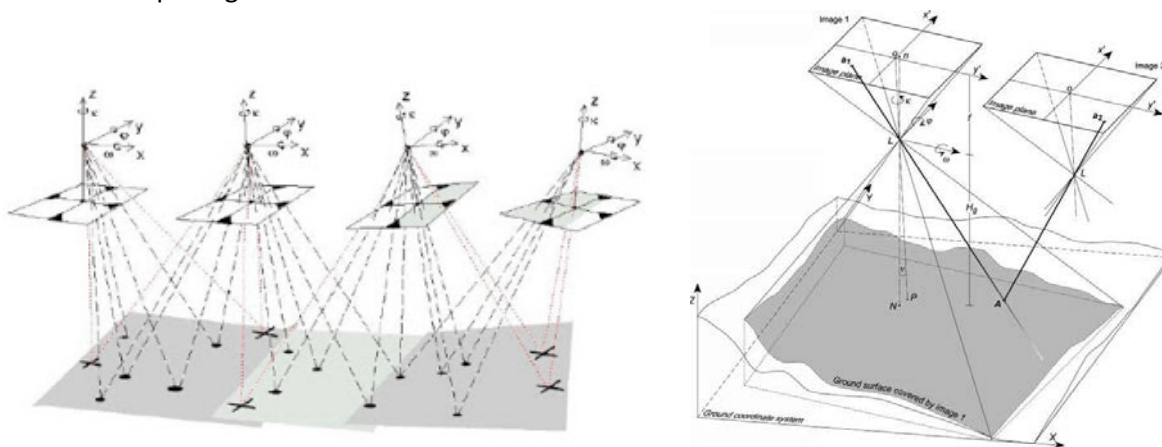
Figure 13: Aerotriangulation and tie-points (multiple sources[25])

Usually, and especially in the recent past, in order to construct a reliable georeferenced orthomosaic, a photogrammetrist would have to rely on precise geolocated Ground control points (GCPs) that would afterwards be used to bind the aerial photos by manually co-referencing the common GCPs between the photos, which then allowed automated image processing algorithms to find multiple other common

---

[24] Aerotriangulation: The Great Soviet Encyclopedia (1979)

[25] http://www.photogrammetrynews.com/2010/08/what-is-aerial-triangulation.html, https://www.tanguayphotomag.biz/aerial-photography/d-measurements-from-stereomodels.html

points while performing orthorectification of the aerial photos. Those discrete points hold three dimensional values and are usually called a point cloud, a set of data points in a three-dimensional coordinate system, defined by X, Y, and Z commonly referenced coordinates.

The resulting accuracy of the orthoimage is based on the accuracy of the triangulation due to the inherent GNSS positioning error and the photogrammetric software accuracy levels, the resolution of the source image, and the accuracy of the elevation model.

Today, the **photogrammetric software** like **Pix4D** that was used in the current experiment, do not need GCPs in order to accomplish very decent results (Küng et al., 2011).

The photogrammetric pipeline utilized through Pix4D consists with all the steps described, parametrized accordingly and conducted in maximum force in order to achieve best orthomosaicing results, using only geotags, even with the highly difficult to process thermal datasets.

Some indicative photogrammetric results from the pilot vineyard and Pix4D can provide some insight for the whole robust process, depicted in **Figure 14 and Figure 15**, displaying the geolocated camera shots and the billions of generated tie points for the orthoimage final construction:
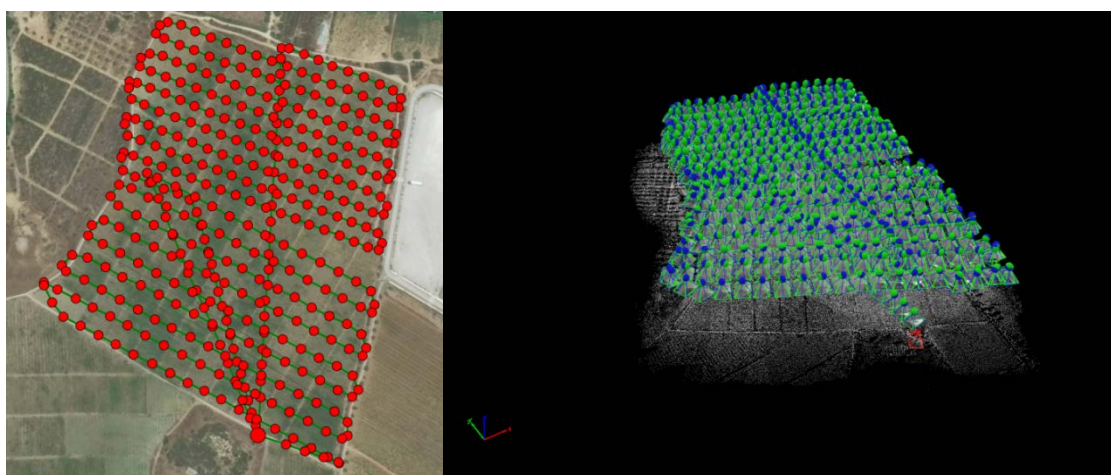
Figure 14: Multispectral dataset: Cameras, Tie Points
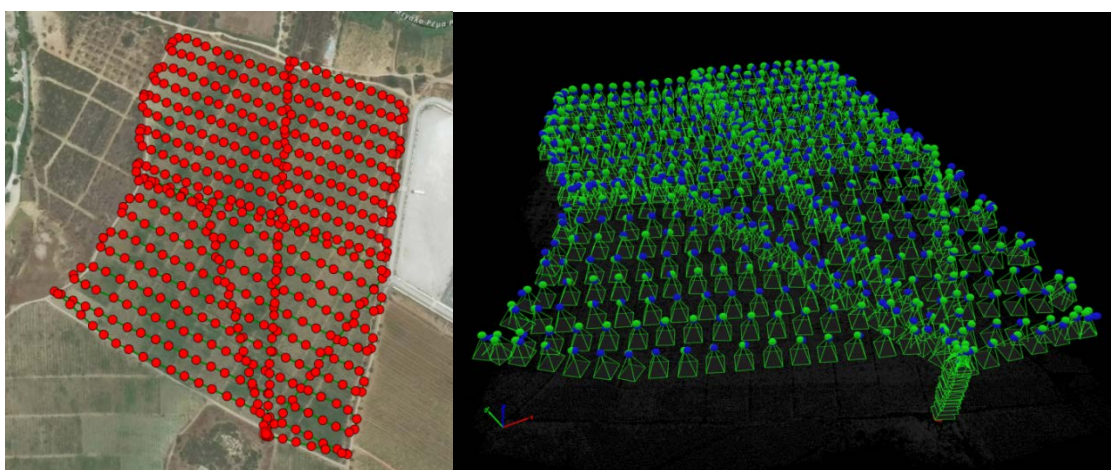
Figure 15: Thermal dataset: Cameras, Tie Points

37

3.3.2.2 Digital Surface Models (DSM)

A highly useful source of knowledge and information is the **elevation depiction in the area under inspection**. In the GIS realm the heightmap generation techniques are either raster grids with elevation data or vector-based (Triangulated Irregular Networks), while the interpretation of each varies (Li et al., 2004). Considering the most recognized approaches, a **digital elevation survey** can be either a Digital Terrain Model (DTM), a Digital Elevation Model (DEM) or a Digital Surface Model (DSM).

Usually, a **DTM** is considered to represent in three dimensions the Earth surface without any objects upon it: the bare earth referenced to a common vertical datum[26], a reference surface like mean sea level. A **DEM** is usually considered a synonym model with DTM for the Earth elevation in most countries, while in USA it has officially a slightly different terminology and methodology substance according to the USGS LiDAR Base Specification[27] .

A **DSM** is a highly different representation of the earth surface as it includes the objects upon it and measures elevation data along with the top surfaces of vegetation and manmade features (**Figure 16**). Lidars and Synthetic Aperture Radar (SAR) instruments are capable of such measurements along with aerial surveying, utilizing the photogrammetric methodology of using images from at least two different locations to generate stereopairs. Each cell of a DSM raster has a value corresponding to its elevation (z-values).

The UAV surveys conducted have been engineered in order to provide sufficient and redundant data in order to employ three-dimensional aerotriangulation stereo photogrammetry and allow the generation of the DSM of the area under inspection from both sensors.
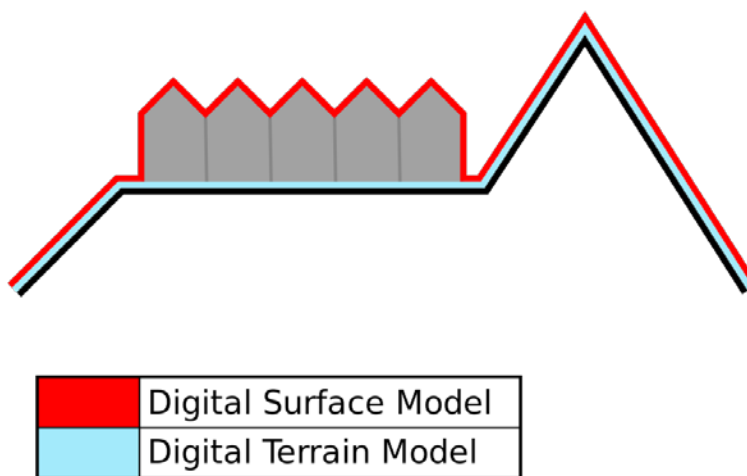
Figure 16: DSM versus DTM (source: Wikipedia[28])

---

[26] A datum is a reference point, surface or axis on an object (e.g. the Earth surface) against which common measurements are conducted. A vertical datum measures elevations or depths, while horizontal datums describe a point in a coordinate system (e.g. latitude/longitude).
[27] https://pubs.usgs.gov/tm/11b4/pdf/tm11-B4.pdf
[28] https://en.wikipedia.org/wiki/Digital_elevation_model

3.3.2.3 Hydrology maps

As the resolution is highly different between the sensors, the DSMs generated are different in the detail provided, but the overall knowledge is sufficient by both in order to understand the earth elevation details of the vineyard, the vegetation status and the hydrological behavior.

DSMs are the primary components for the hydrological and water-terrain analysis of the surface land. The current methodology employs the DSM and hydrology algorithms that perform deep pixel analysis in order to output the water flow (direction and accumulation) in regard to the specific surface morphology and define how the geographic range of an area interacts with water (Maidment and Djokic, 2000; Shamsi, 2005).

As a general principle, the **hydrological algorithms** simulate the water flow by determining the best route it would take, the flow from each grid cell to one or more of its neighbors, by determining for each surrounding pixel the elevation values and assessing the weights for the conceptual movement, flow route and accumulation (Garbrecht and Martz, 1997). Calculating the flow accumulation, these algorithms trace the flow of each cell in a DSM separately until it finally leaves the DSM or ends in a sink. This procedure also relies in the prerequisite that pits (low elevation areas in DSMs that are completely surrounded by higher terrain) are first removed, a terrain feature that does not exist in the surveyed area.

3.3.3   Satellite Data

In Precision Viticulture and generally for permanent crops, surveys during important growth stages have a significant agronomic value, however they are not enough. The spatial variabilities and features depicted during an aerial survey do not provide a fully consistent view of the crops and area status.

The temporal dimension in crop monitoring is invaluable for a complete systematic approach. The Sentinel-2 data were chosen to provide this dimension at about once per month for all available sequential months critical for the growth of the vine and its berries: May to August. In this manner the monitoring of vines can be consistent and a time series methodology can be constructed.

Copernicus Sentinel-2 mission is the most efficient open data policy source of agriculturally useful images worldwide. The 10 and 20 meters spatial resolution of the vegetation bands provide really useful input to the ~20 hectares area under inspection.

In order to study the area that contains the Region Of Interest (ROI), six(6) S2 images were acquired from the Hellenic National Sentinel Data Mirror Site from NOA.

Cloud coverage is a vital factor in EO and RS from satellites with multispectral instrumentation for vegetation and land cover uses, as the existence of clouds over any area will obscure it and no information can be extracted. Even shadows of the clouds that were encountered on top of a portion of the pilot vineyard in an otherwise fine multispectral dataset distorted the reflectance values and rendered the imagery useless.

The S2A L2A images used are shown in **Table 5**:

Date	Name
2017/04/26	S2A_MSIL2A_20170426T091031_N0204_R050_T34SGH_20170426T091828.SAFE
2017/06/05	S2A_MSIL2A_20170605T091031_N0205_R050_T34SGH_20170605T091810.SAFE
2017/06/15	S2A_MSIL2A_20170615T090551_N0205_R050_T35SKC_20170615T091937.SAFE
2017/06/25	S2A_MSIL2A_20170625T091021_N0205_R050_T35SKC_20170625T091829.SAFE
2017/07/05	S2A_MSIL2A_20170705T090551_N0205_R050_T34SGH_20170705T090814.SAFE
2017/08/04	S2A_MSIL2A_20170804T091031_N0205_R050_T35SKC_20170804T091836.SAFE

Table 5: Sentinel 2 imagery used

The Sentinel 2 bands used were the ones that were useful for the PV application. In this manner, the 10m and 20m resolution bands were transformed and formulated into VIs and band composites.

As the satellite data were retrieved and examined after the drone survey in the current study, the VIs were chosen to be the same for exhibition and comparison reasons. However, the MSI instrument holds much more potential in regard to crop monitoring than the specific usage of those bands in specific formulas. The multiple Red Edge and SWIR bands are valuable for the generation of tens of significant VIs like the Normalized Difference Water Index (NDWI) that can provide deeper results and the Red Edge bands are best suited for different crops in compliance with their specific Red Edge reflectance features.

The bands used are: Band 2 (Blue), Band 3 (Green), Band 4 (Red), Band 6 (Red Edge), Band 8 (NIR)

As shown in **Table 4**, Band 6 was chosen from the three Red Edge bands on the MSI instrument, as this band has the closest characteristics (central wavelength and bandwidth) to the UAS's Sequoia Red Edge sensor.

The satellite images were clipped to the extent of the vineyard under inspection with wide enough borders in order to include parts of the surrounding vineyards for comparison reasons and resemble the data received from the UAV flights. The clipping process was conducted through QGIS and the Saga tools.

As expected any finer satellite imagery resolution would provide more and deeper information on the vineyard and the vegetation status, however the 10m resolution provided for free is the best available tool and provides very decent intelligence.

More details on the satellite images used can be reviewed in **ANNEX 3 – Sentinel 2 datasets**.

4 Results

The vineyard under inspection is in the area of Spata, Greece. It is irrigated, agriculturally attended with plants of ~1-1.5m height, in the stage of setting for the berries, after a long period of high precipitation and humidity in the area before the acquisition of the aerial imagery.

Vine cultivation and wine production has been an old practice in the region along with other agricultural activities. The agrometeorological conditions in the particular area have been recognized for high quality wines from empirical past efforts, which identified the territory for ideal viticulture. Hillslopes, mesoclimatic conditions of irregular air currents, humidity and temperature along with excellent soil comprise the whole picture and are capable of providing high quality products.

Selected CRS: EPSG 32634, WGS 84 / UTM zone 34N

Extent with coordinates: North: 4208630.498570001, South: 4207949.445470001, East: 755413.9638200001, West: 754883.7138200001

Area under inspection: ~20 hectares

Strict borders of vineyard: ~15 hectares

The orthomosaics were generated by the specific photogrammetric pipeline explained, employing the Pix4D software.

The specific pilot vineyard has been selected for its PV exhibition potential derived from the high internal variabilities in both phenotypical and biochemical features and site specific characteristics like topography.

The vineyard pilot site can be described agriculturally as a moderately cultivated vineyard. In contrast to surrounding vineyards in the vicinity which can be seen in the orthomaps and are intensively cultivated and taken care of, the pilot site vineyard shows very high internal variability in multiple aspects that cannot be solely explained by its size even if it covers an area of ~15 hectares.

Extensive spots empty of vines or sparsely planted, huge areas of lower plant growth, unattended plants that are not pruned as commonly instructed by viticulturists, partial ploughing and other aspects, comprise a vineyard with very high potential but low farming attention.

4.1 Multispectral, Panchromatic orthomosaics and Index Maps

The specifics of the multispectral and panchromatic datasets are the following:

Date/Time: 2017/06/21; 18:00

UAV Flight Altitude: 100m

SEQUOIA images shot at survey mode 75% overlapping, both sidelap and overlap: 400 sets of 5 sensors geolocated images.

Table 6 shows the pixel sizes and the full sizes of the orthomosaics generated.

RGB orthomosaic (**Figure 17**) pixel size	0.02763m
Multispectral orthomosaics (**Figure 18**) and index maps pixel size	0.10605m
RGB orthomosaic size (X, Y)	17068x22823 pixels
Multispectral orthomosaics and index maps size (X, Y)	5000x6422 pixels

Table 6: SEQUOIA orthomosaic volumes

The index maps were constructed with QGIS.

The raster layer values were calculated from the spectral bands through Raster Calculator and classified in 5 classes in continuous mode using linear interpolation for the values, representing the data range from 2% to 98% of the data values.
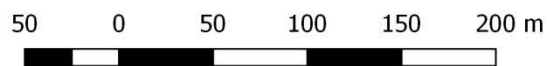
Figure 17: RGB orthomosaic

GREEN

RED

RedEdge

NIR

50 0 50 100 150 200 m
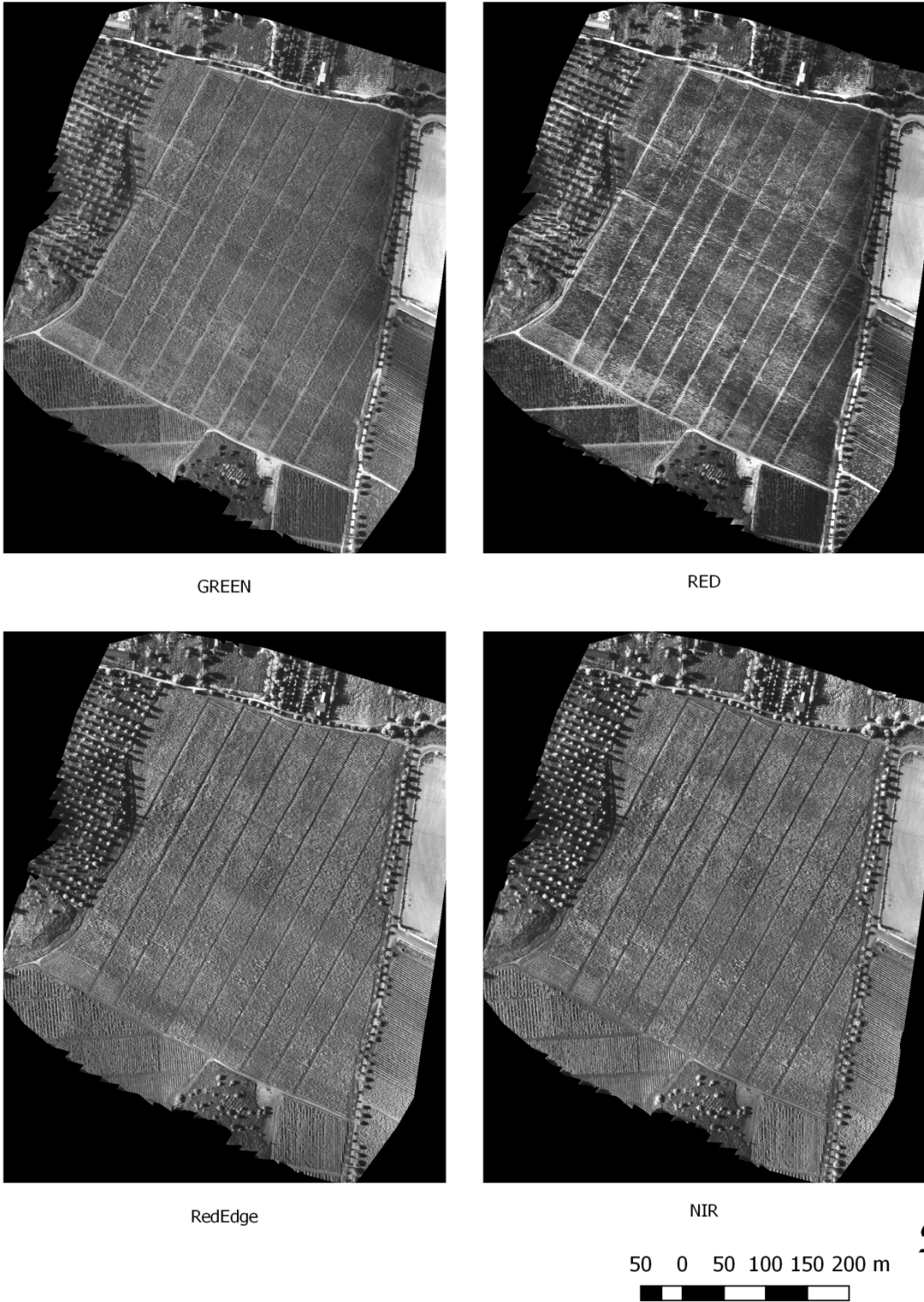
Figure 18: Four monochrome orthomosaics from each SEQUOIA sensor

A very interesting result is presented by **false multicolor composites**; images with three different bands from Red, Green and Blue, which are used in order to deliver a true colors composite image perceived to the human eyes. In the current experiment and under the availability constraints of certain bands with certain characteristics concerning vegetation, the richest false composite for agricultural purposes is the NIR, Red, Green (NIRRG) one.

Figure 19 depicts the NIRRG **false multicolor composite** of the pilot site and **Figure 20 and Figure 21** provide a comparative view of the orthomaps.
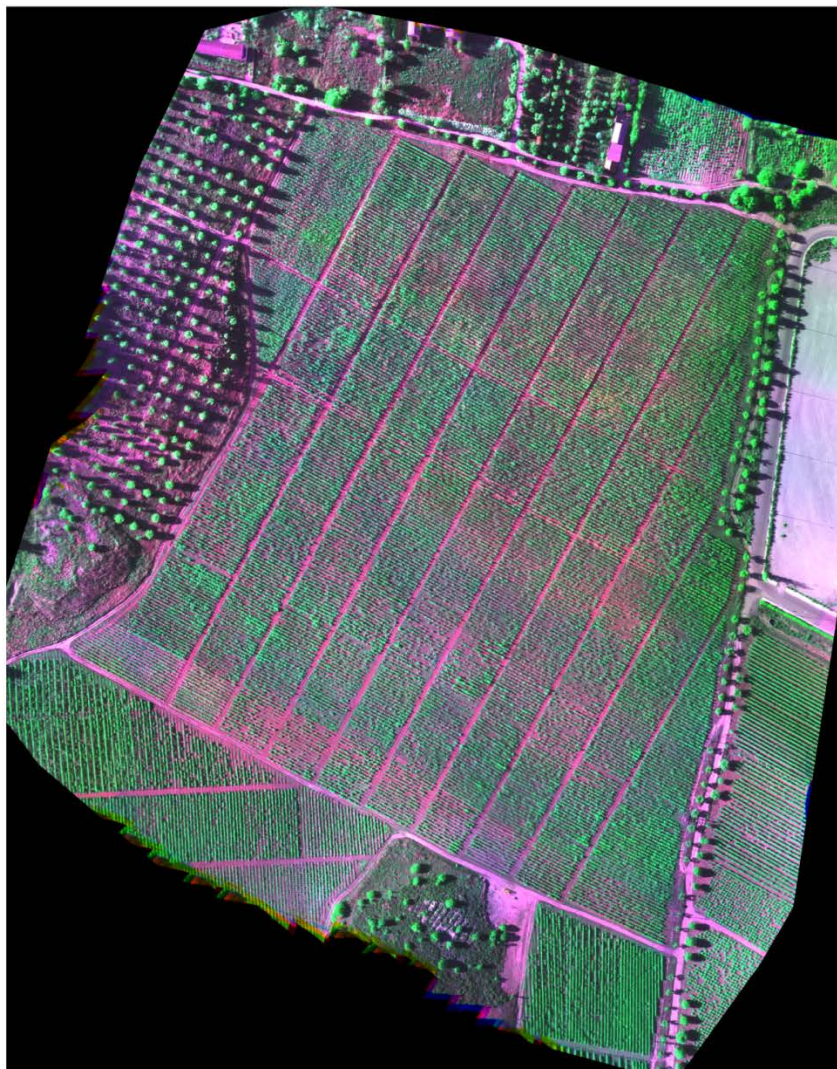
Figure 19: False color composite (NIR-R-G)
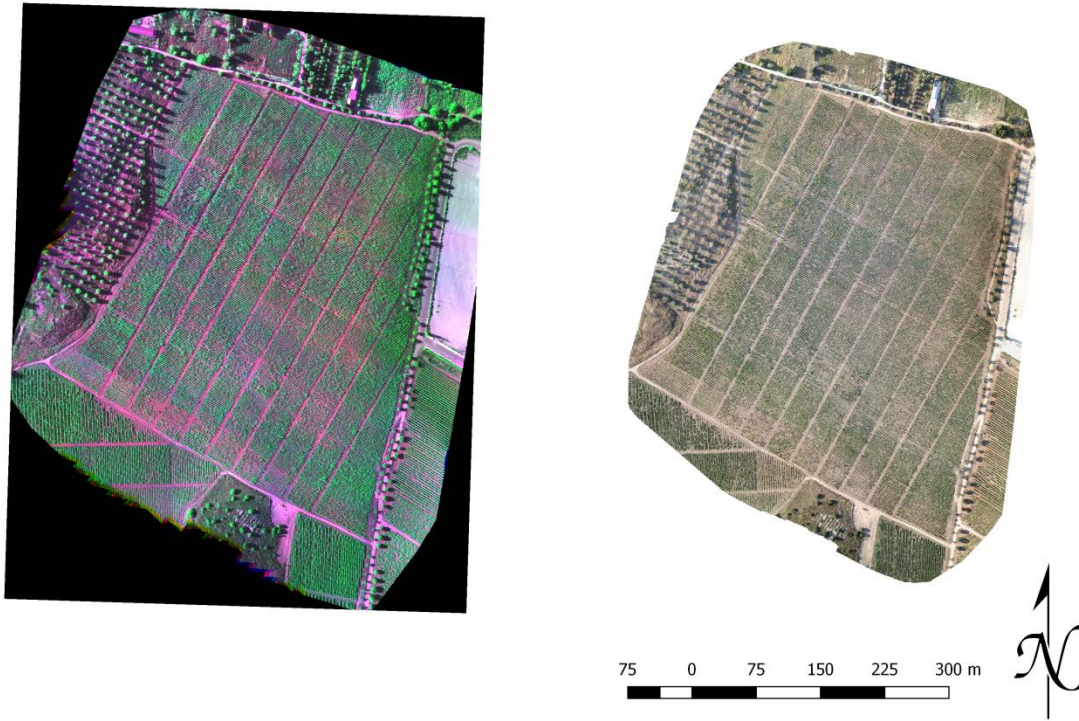
Figure 20: NIRRG false color composite versus the RGB panchromatic map
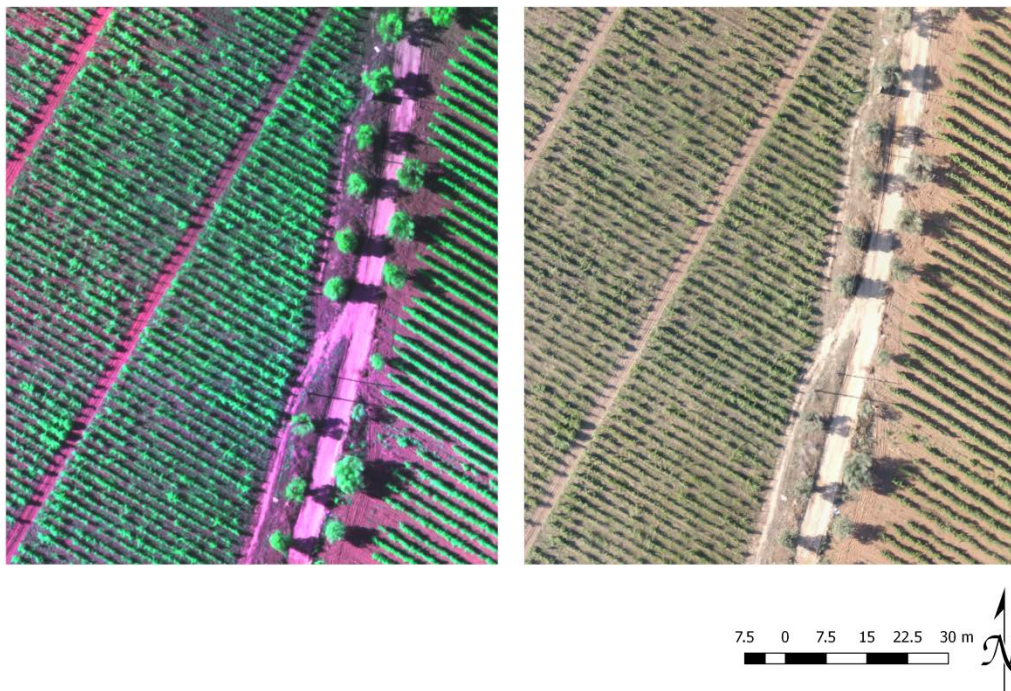
Figure 21: NIRRG false color composite and RGB details

The RGB orthomosaic (**Figure 17**) is literally a bird's eye view of the monitored area in regard to the human perception of the visible part of the electromagnetic spectrum. It is evident that some characteristics of the structural and generic status of the plants can be extracted, especially in comparison with nearby bordering vineyards that are clearly in a much better agronomical state.

The holistic view of the parcel, the comparison potential, the human cultivation impacts like ploughing and some internal visible variability is vines growth are already a very important potential of the panchromatic orthomapping of a vineyard of this size. As shown later however, this is still a quite poor source of agronomical information in comparison with the multispectral results. Invisible characteristics and aspects showing the plants' vigor and photosynthetic capacities, as well as potential unperceivable to the eye stress factors cannot be depicted through a usual RGB optical lens.

It is worth mentioning that the time of images acquisition in late afternoon is distorting the results to some extent due to the serious shadowing effects. However, the very high resolution and the multiple index transformations still provide the information needed.

To the human perception from the ground point of view when inspecting the vineyard even a highly experienced agronomist would be unable to understand the real nature of it. The vineyard seemed to be in a very good condition, with vivid vines and healthy leaves everywhere. Its true nature however, was revealed when depicted from above even from the panchromatic sensor, clearly contradicting the false panoramic human eye view.

The monochromatic sensor outputs from the multispectral payload shown in **Figure 18** are also poor sources of valuable knowledge by themselves. Even if the variation in reflectance values, especially in the NIR, could show internal vineyard spatial variabilities, the overall result is of little use. The orthomaps generated from each sensor from the multispectral sensor array are valuable mainly for the generation of VIs.

The shadowing effects are once more highly visible in each monochromatic orthomosaic, distorting the real reflectance values below the shadows and between the vines. This harsh effect is minimized once more through the VIs generation.

The **NIRRG false color composite** (**Figure 19**) exhibits a highly vivid environment, with detail and much less noise from external factors to vegetation, mainly due to the high NIR and Green reflectance from the plants. In comparison with an RGB image (**Figure 20, Figure 21**), the false NIRRG composite has much more information, it is a finer way to depict vegetation and provides clearer results.

It is very interesting that the higher vegetation detail is evident in the light of the fact that the NIRRG false color composite image has a much lower resolution (5000x6422 pixels at 0.10605m pixel size) than the RGB one (17068x22823 pixels at 0.02736m pixel size), due to different resolutions of the monochromatic and panchromatic sensors.

Indicatively, in **Figure 21** one can easily discriminate shadows from trees and plants canopies, the internal parasitic vegetation -if existent-, the underlying soil against the overlying vegetation. Even in the qualitative realm for the vines, the portion captured from the neighboring eastern vineyard shows

clearly a uniformity in its cultivation and agricultural attention, higher vigor and clean underlying soil in comparison with the pilot site partly shown west of the bordering road and trees.

In a hypothetical scenario of monitoring very dark colored plants where shadows could be difficult to discriminate from the canopies or inside the canopies, the NIRRG false composite would immediately show the true nature of the plants.

Figure 22: NDVI map

Legend

SAVI

■ -0.594
■ -0.244
□ 0.105
■ 0.454
■ 0.804
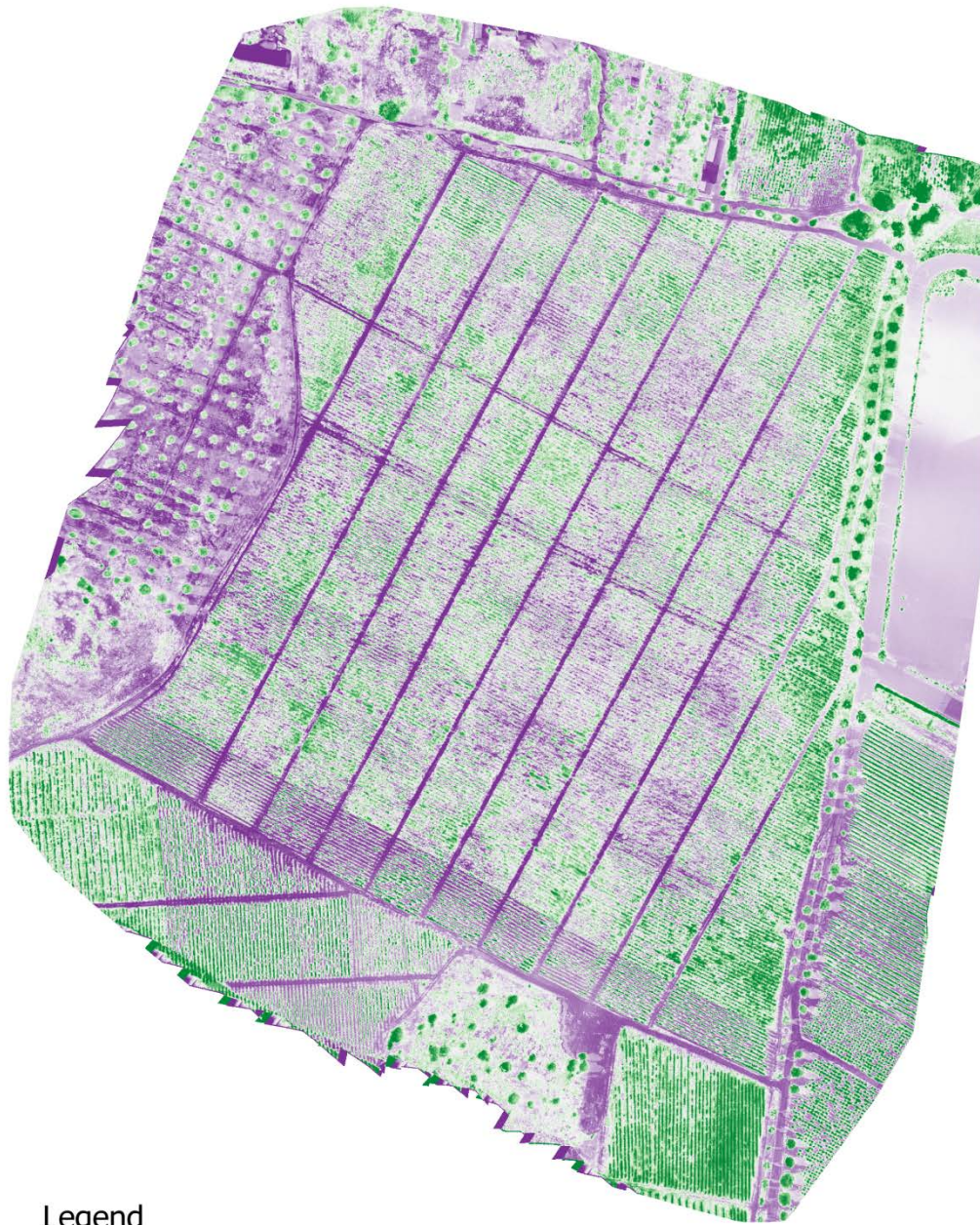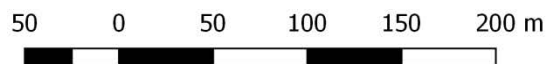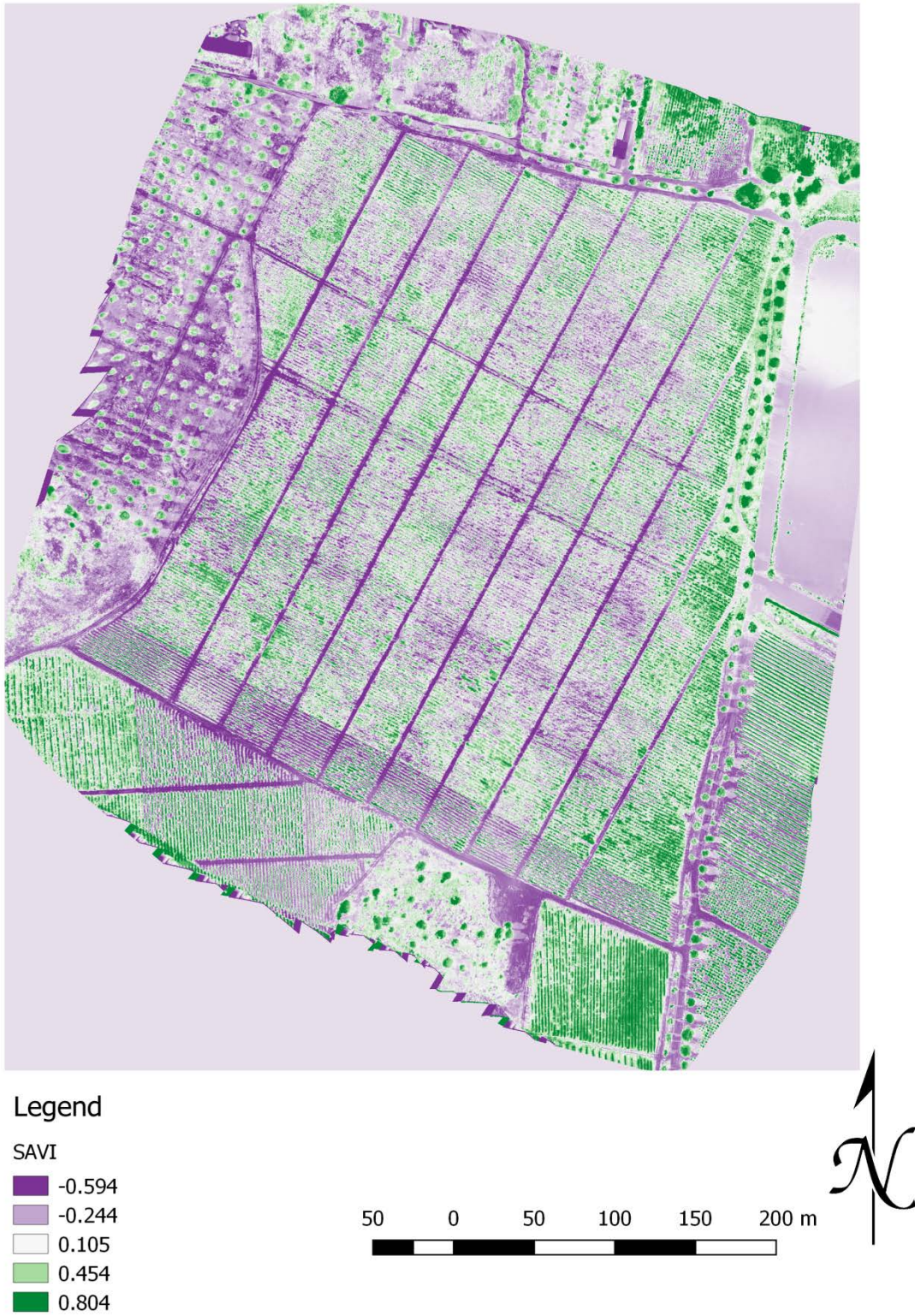
Figure 23: SAVI map

The **NDVI index map** (**Figure 22**) has been linearly classified in 5 classes. The negative and near zero values classified in the first two classes show the bare soil and soil with very little vegetation. NDVI values greater than zero reaching the upper unity limit depict vegetation with the values variability characterizing the vigor and health of vines while being subject to the leaves concentrations due to the vines layered structure.

It can be easily observed that lower index values as classified in the first two classes mostly contain the soil information and reflectance uniqueness. The next 3 classes that contain the continuous indices' values most certainly contain the valuable information on the plants' status. In this context, it is worth mentioning that around the NDVI and SAVI values concentrations which occur in dense vegetation like trees outside the vineyard borders and the canopy of the vines inside the vineyard it can be distinguished that a medium index values **corona** exists. This white corona which is depicted like white pseudocolor borders of the vines and trees is the result of the outermost layer of leaves from each vine. As the vines hold multiple internal layers of leaves, the centrally concentrated chlorophyll and the consequent strong reflectance is distinguishable from the outer layers which naturally display lower index values. Hereafter, **the "white corona" effect** is interpreted in the same manner for all VIs and the thermal datasets.

Additionally, the rows of vines are clearly discriminated in the surrounding bordering vineyards and the southernmost part of the pilot site as they are ploughed and the soil is clean of interfering vegetation while the plants exhibit a high level of uniformity. On the contrary, the pilot vineyard shows a high level of mixture between the vine rows and in-between spacing which is dominated by underlying vegetation that generally has NDVI values lower than the vines' canopies.
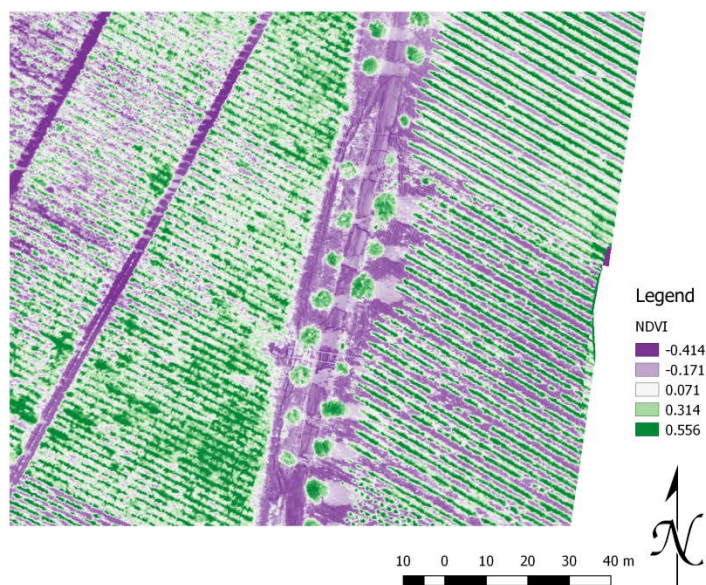

Figure 24: NDVI indicative part

As described in the previous maps, the shadowing effect is evident, but homogeneously and proportionally its impact is minimized by the indices mathematical nature. The difference in shadows interference on the left where underlying vegetation reflectance is mixed with the soil under shadow reflectance, and the right well attended vineyard, is vividly shown in **Figure 24**.

In regard to the **SAVI index map** (**Figure 23**), the results are almost identical for the interpretation of the values and the discriminatory capabilities for a zonal approach and the extraction of critical vines or the vineyard's features internally. This behavior is probably the result of the relatively low resolution, detail needed and the specific characteristics of the underlying soil in conjunction with the low vegetation which makes no real difference in the soil adjustment factor introduced by SAVI to the NDVI.

The **NDVI and SAVI index maps** (**Figure 22 and Figure 23**) are theoretically and practically considered close members of the same indices family. As explained in the relevant chapter, SAVI easily reduces to NDVI when the adjustment factor L is set to 0.

Legend

CI_RedEdge

- ■ -0.243
- ■ -0.105
- □ 0.0318
- ■ 0.169
- ■ 0.306

50   0   50   100   150   200 m
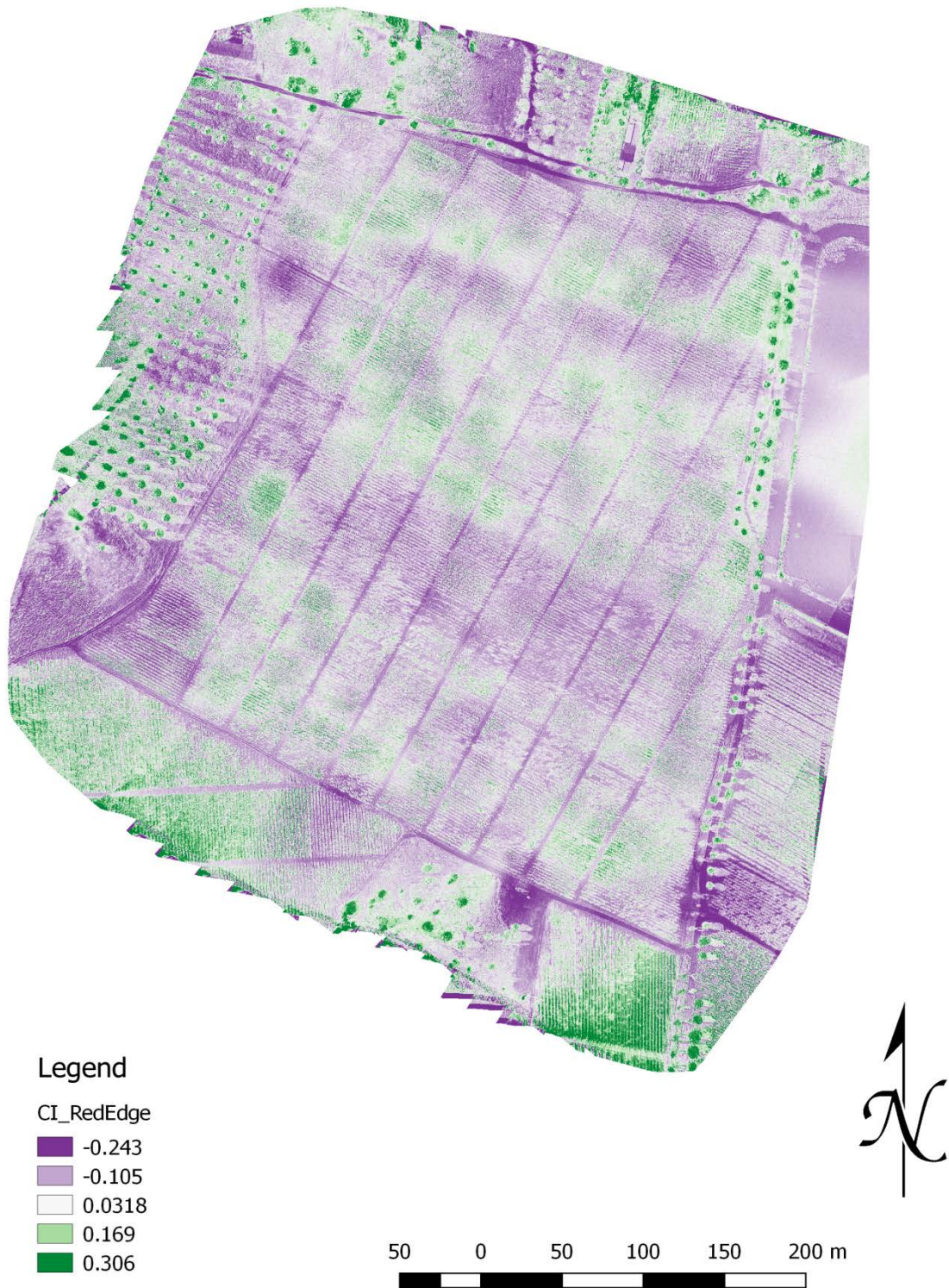
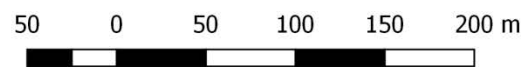**Figure 25: CI-RedEdge map**
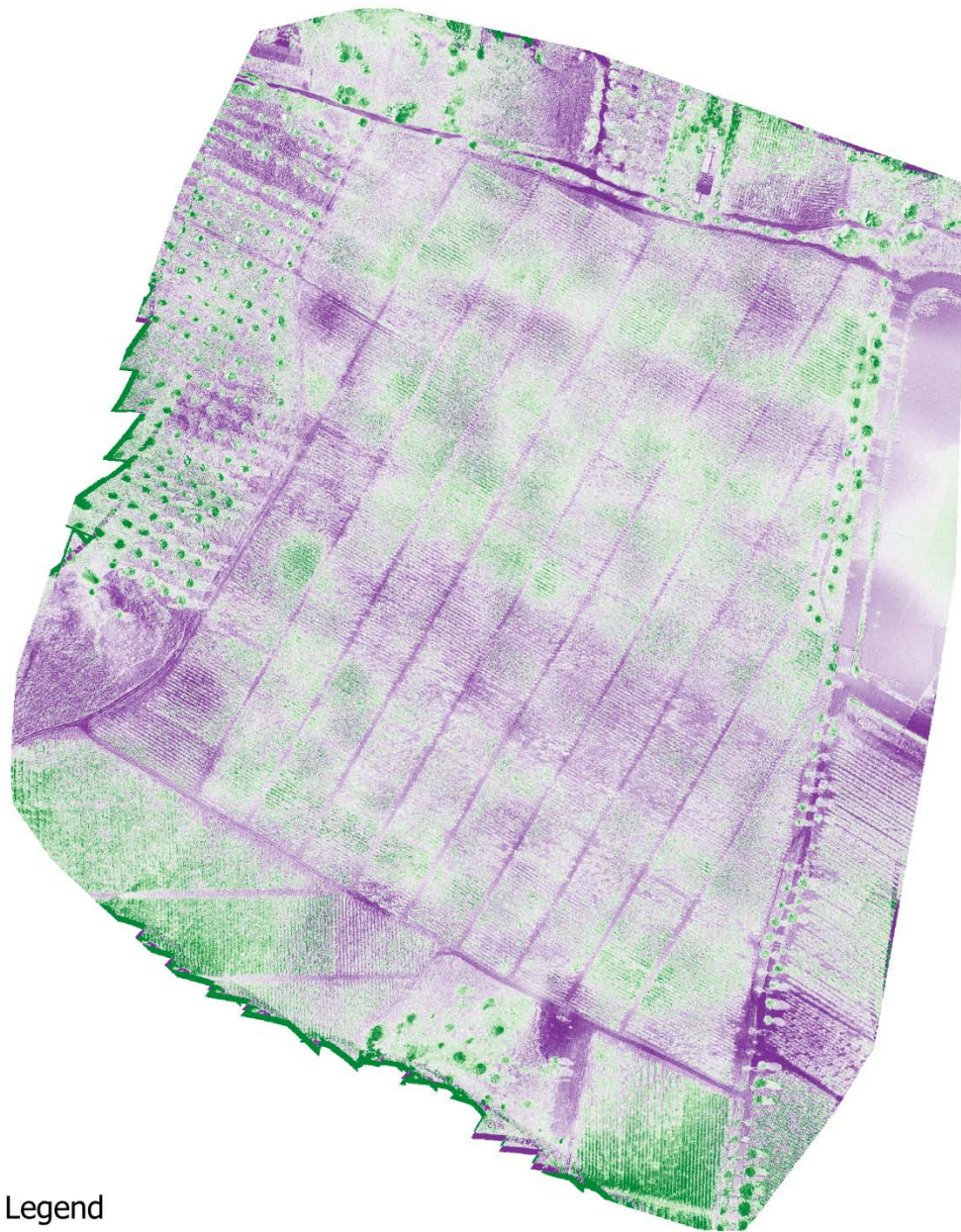
Figure 26: RENDVI map

The Red Edge Chlorophyll index map (**Figure 25**) and the **Red Edge NDVI index map** (**Figure 26**) both utilize the red-edge band to provide the most useful knowledge estimating the chlorophyll content and photosynthetic capability of the vineyards.

Through these two index maps it is evident that zones of higher photosynthetic capacity are existent within the pilot vineyard and the bordering vineyards.

Those zones are hardly visible to the NDVI or SAVI index maps and their highest values concentration are the healthiest and most efficient vines. Even in the very well attended **bordering vineyards** in the southern and southeastern parts of the map, there exist clear variabilities and differentiations that are clear when inspecting the chlorophyll content but not so clear in any other depiction like the NDVI.

Differences depicted in a 5 class discriminatory scheme as conducted in the current study are already enough to reach useful conclusions about the status of a vineyard and clearly indicate the regions of interest and even individual vines that are in the best or worst state in order to indicate potential stress, different growth stages, irrigation problems and nutrient deficiencies.

Additionally, as the photosynthetic capacity is most influenced by the leaf area index and the vigor of the plants, underlying vegetation noise is highly reduced even if it reflects highly in the NIR and thus contributes to VIs like NDVI.
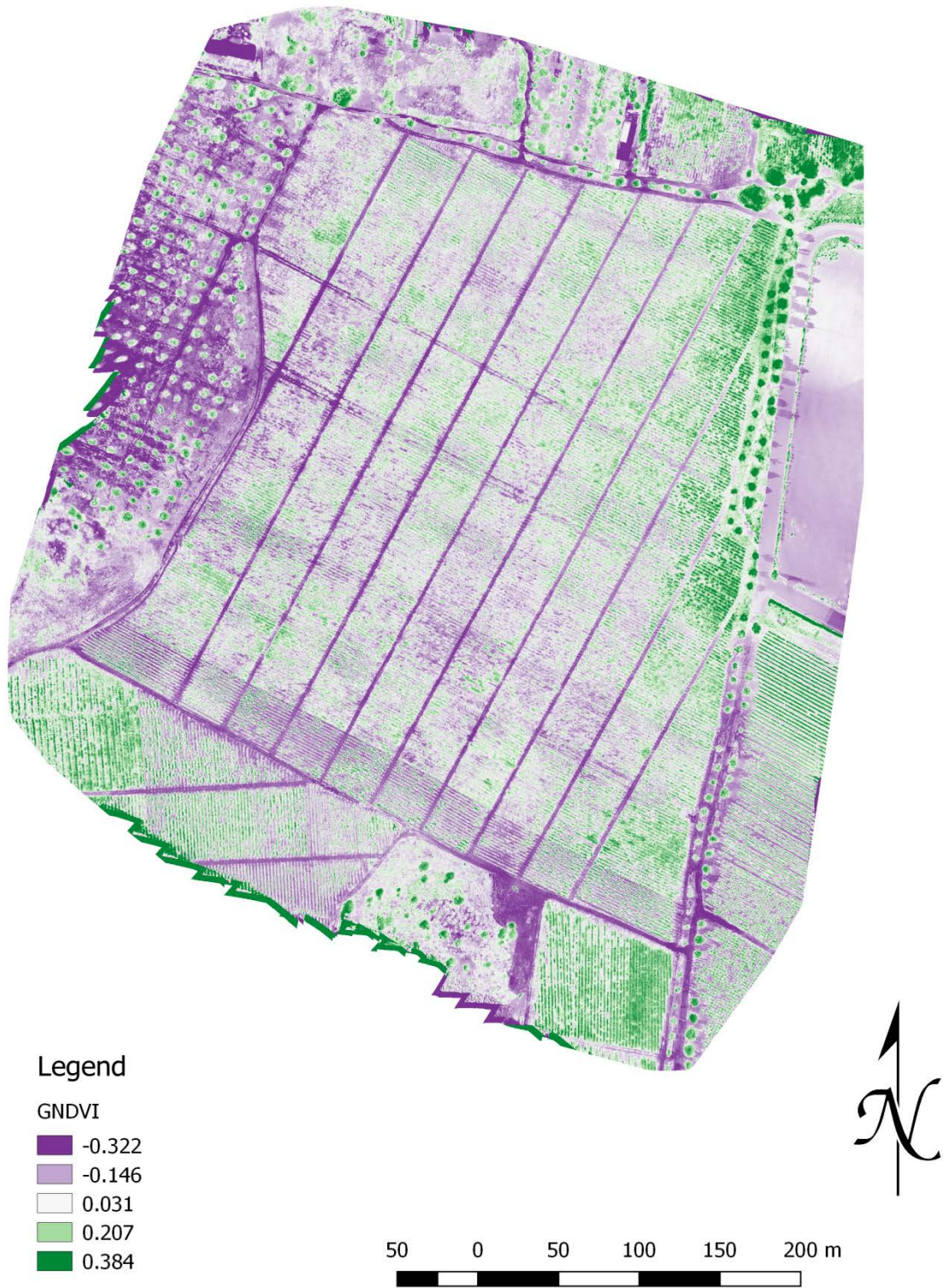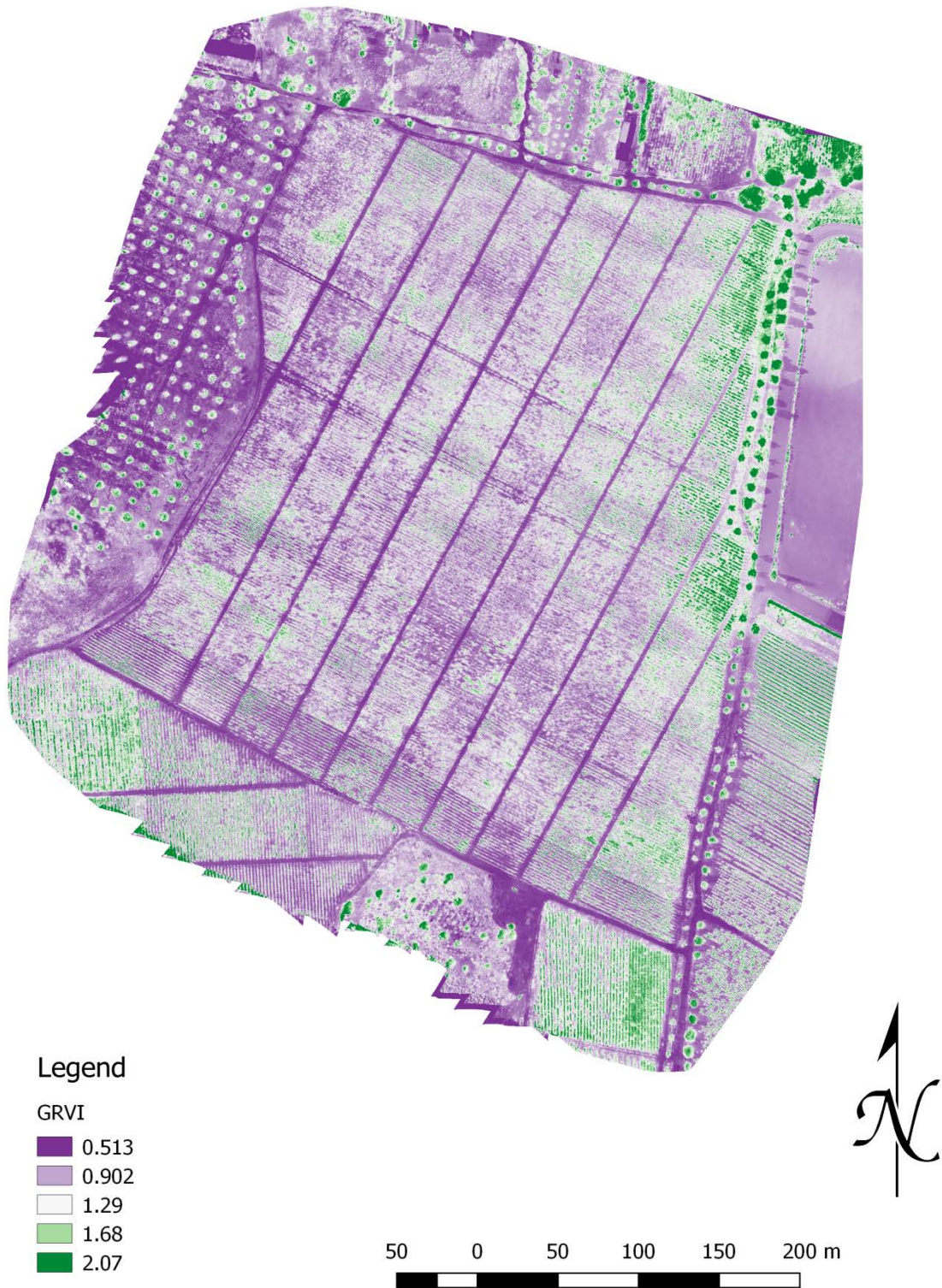
Figure 27: GNDVI map

Figure 28: GRVI map

Legend

GRVI
- 0.513
- 0.902
- 1.29
- 1.68
- 2.07

50 0 50 100 150 200 m

GNDVI and GRVI index maps (**Figure 27, Figure 28**) are linearly classified in 5 classes as well for comparison reasons as all of the index maps and provide evidently less information that the NDVI and the Red Edge index maps.

GNDVI values extend from -1 to +1 like the NDVI index translating into relative results in concern to the interpretation of the map and the zonal approach. However, the information derived from the Green band holds less information in general and the details are more vague, mainly under the contribution of the NIR band.

Soil reflectance transformation values are very distinct in the Green indices, offering the potential for specific knowledge extraction like trees in the vicinity which are greatly discriminated by those indices making them possibly valuable in assessing the vigor of tree canopies and the counting them.

Comparing the Red Edge maps with the Green and NIR derived ones, one can see that the photosynthetic capacity of a zone under inspection is not always linear to its greenness, thus making the **chlorophyll red edge reflectance most valuable** when available.

Figure 29 shows all the index maps in one comparative view. The generation of multiple indices has been executed in order to evaluate the most efficient ones in concern of the knowledge extraction potential, the portion of overlapping information between the VIs themselves and their suitability for vineyards.
The current vineyard is large enough in order to provide the needed spatial variability and the different internal zones for presentation purposes. Those zones can be discriminated by agricultural actions taken, the plantation variability and the vitality of the vines themselves.

Interpreting the results and the indices transformation outputs, it can be concluded that some of them provide subsets of useful knowledge when compared even if their general value is profound in other cases. Considering vineyards and the specific area under the specific conditions the indices omitted will be the SAVI, as it contains almost identical information with the NDVI, the GRVI as it contains much less useful information than the other indices and the GNDVI as it provides noisy information concerning the vines. Finally, RENDVI seems to be more sensitive to noisy underlying vegetation while overlapping with CI_RedEdge, keeping the latter under closer inspection for the higher detail and well-documented potential as well.
**The useful indices that show in the most evident way the state of the vineyard, the internal variability and the plants condition have been chosen to be the widely used NDVI and the CI_RedEdge.**
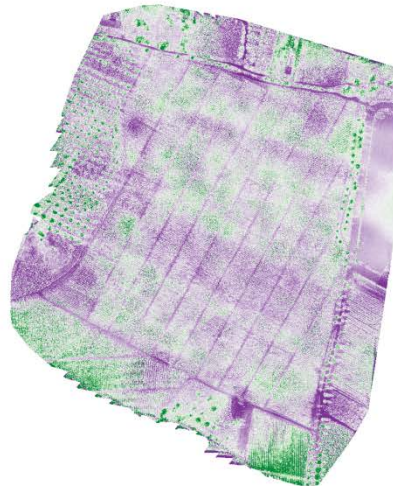
Legend

NDVI
-0.414
-0.171
0.071
0.314
0.556

SAVI
-0.594
-0.244
0.105
0.454
0.804

CI_RedEdge
-0.243
-0.105
0.0318
0.169
0.306

RENDVI
-0.142
-0.071
0
0.071
0.142

GNDVI
-0.322
-0.146
0.031
0.207
0.384

GRVI
0.513
0.902
1.29
1.68
2.07
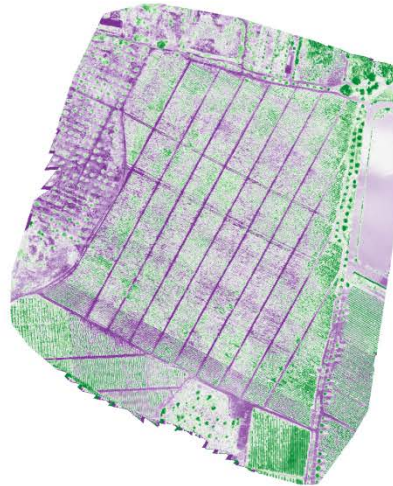
NDVI
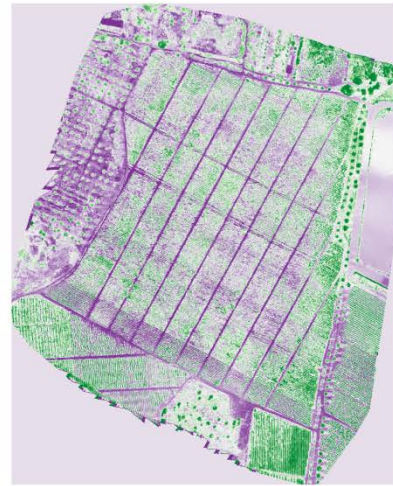
SAVI

CI_RedEdge

RENDVI

GNDVI

GRVI

75 0 75 150 225 300 m
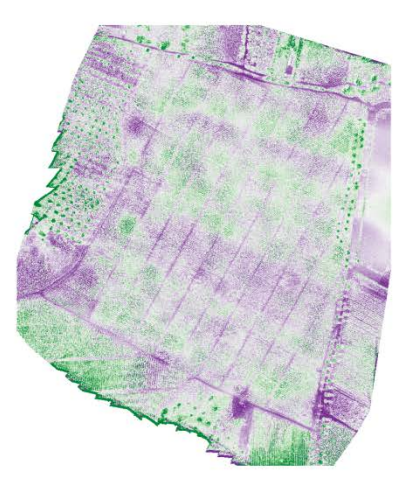
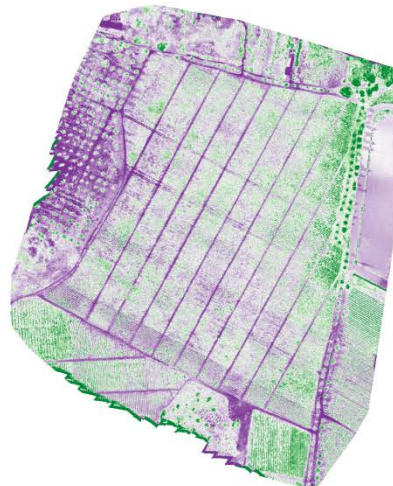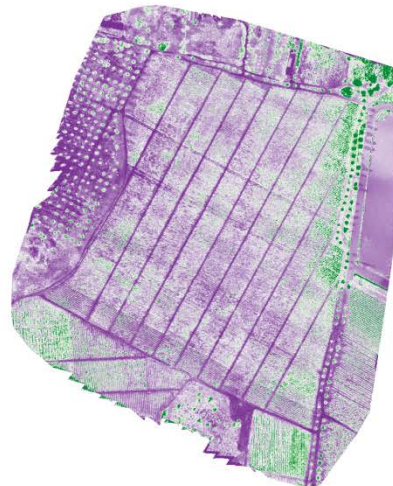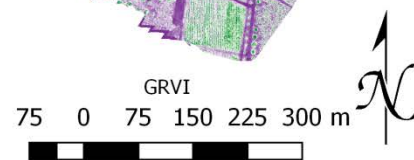**Figure 29: All index maps**

4.2   Thermal Infrared orthomosaics

The specifics of the 1st thermal dataset are the following:
Date/Time: 2017/06/21; 18:00
UAV Flight Altitude: 100m
Pixel size: 0.13381
Orthomosaic size (X, Y): 3838x4660 pixels
Flir Vue Pro R images shot at survey mode 75% overlapping, both sidelap and overlap: 581 geolocated images in JPEG format. This has resulted in a mosaic by Pix4D that does not keep the radiometric values for each pixel and depicts the vineyard in a specific thermal colormap.

The specifics of the 2nd thermal dataset are the following:
Date/Time: 2017/06/26; 13:00
UAV Flight Altitude: 100m
Pixel size: 0.13312
Orthomosaic size (X, Y): 3741x4628 pixels
Flir Vue Pro R images shot at survey mode 75% overlapping, both sidelap and overlap: 729 geolocated images in TIFF format.
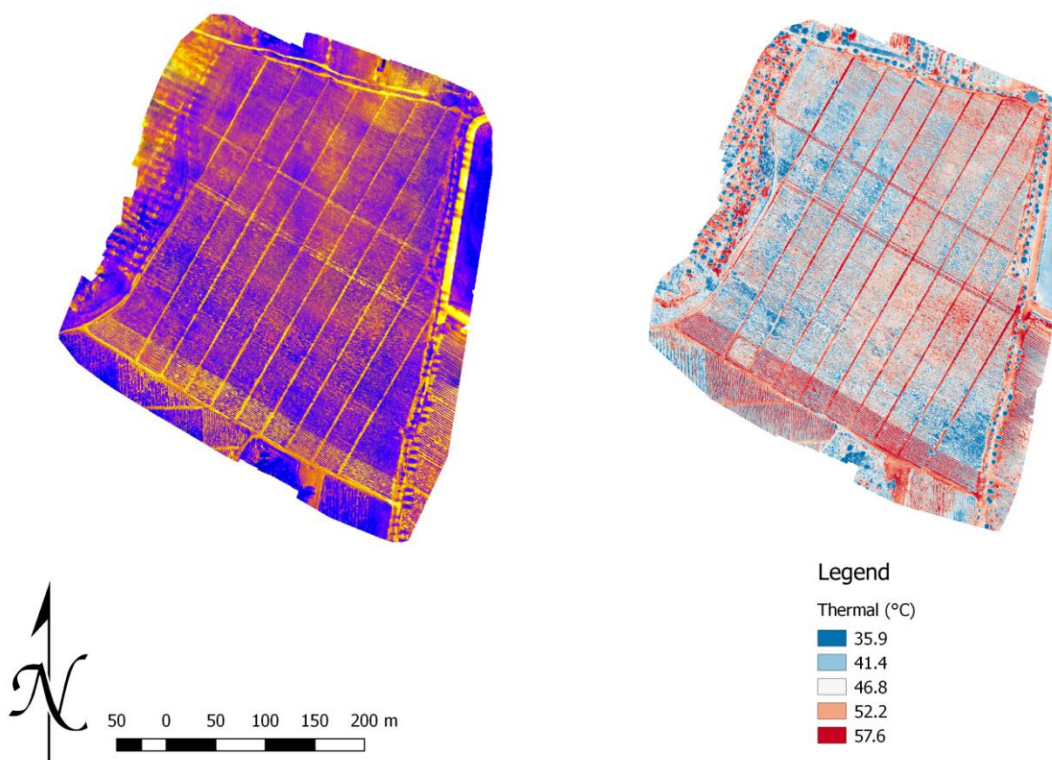The values were classified in 5 classes in continuous mode using linear interpolation, representing the data range from 2% to 98% of the data values.

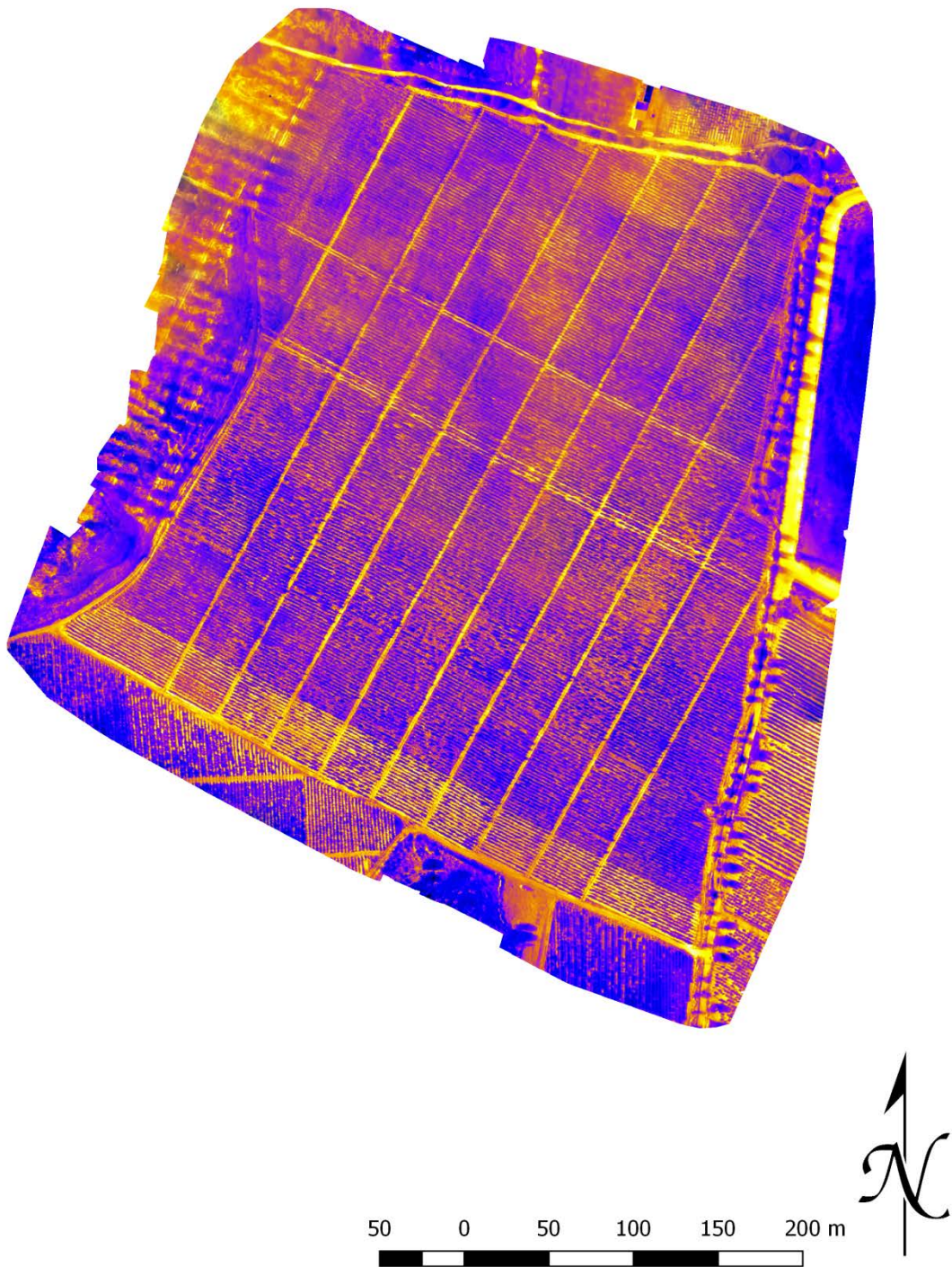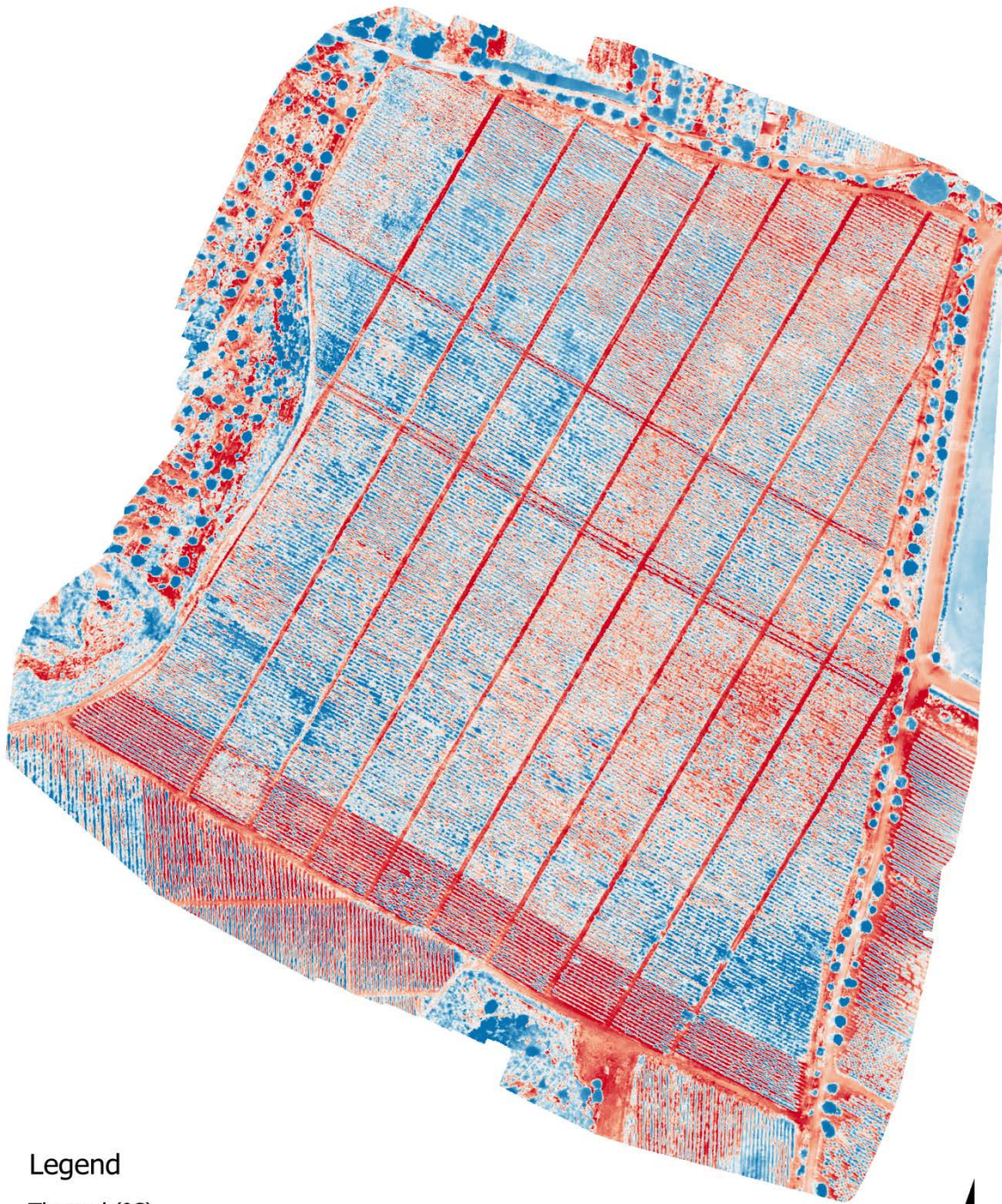Figure 30: Thermal orthomosaics

Figure 31: First thermal orthomosaic

Legend

Thermal (°C)

■	35.9
■	41.4
□	46.8
■	52.2
■	57.6

50 0 50 100 150 200 m
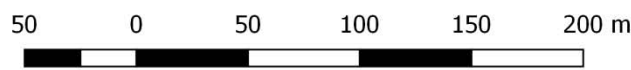
Figure 32: Second thermal radiometric orthomosaic

Figure 30 provides a comparative view of two thermal datasets shot within 5 days at different times. Both of them have been shot with the radiometric thermal payload , however the first one which was shot at 18.00 in the afternoon was set to store the images in JPEG format providing the default colormap and not the exact values inside each image metadata.

For the first thermal dataset (**Figure 31**), as the time was late afternoon like the multispectral sensor, the shadowing effects are very strong. For the thermal survey of the vineyard this poses a real issue. Shadowing in thermal data greatly distorts the results as shadows cast on vegetation reduce its overall temperature, thus providing significantly less accurate readings for the vegetation status and real temperatures than under zenith sun conditions. Even under these shadowing conditions, as the field is wholly depicted, still a zonal approach is achievable without taking into account the precise radiometric values and the variations in shadows from one plant or tree to the other or the lower vegetation.

This is the reason that a second flight would have to take place in a suitable timeslot. **Figure 32** shows the result of the second flight at almost midday and the thermal orthomosaic generated. This dataset was shot under TIFF format for the images allowing an even better and more suitable processing of the images and the final product.

It has been argued that orthomosaicing thermal radiometric datasets is a very difficult task, as overlapping photos may provide different temperatures for the same pixel. This endeavor has been left in the hands of Flir and Pix4D for the accuracy of the methods used internally, however a robust result is generated that appears very close to the reality of the vines as both thermal mosaics correlate greatly between themselves and with the multispectral and panchromatic evidence. In the current context, the absolute temperature is not considered a priority or as valuable as in other applications and a proximity orthomosaicing strategy is sufficient.

In regard to the temperature readings and the continuous linear classification in 5 classes, multiple vegetation aspects can be derived.

In a matter of principle, the higher a plant's temperature the higher the possibility to be subject to a stressful factor like drought, infestation etc. as described earlier. Bare soil and very low vegetation have the highest temperature values around 60°C while the mid class temperature values at ~55°C are the result of very low vegetation or few leaf layers at the vines disturbed thermally by the soil below, comprising the vines' "white corona" effect.

The healthiest vines show temperature values around 35 degrees Celsius. Soil vegetation underlying at the vineyard rows has a few degrees higher temperature at ~40-45°C.

4.3 Digital Surface Models (DSM)

Digital Surface Models were generated by both sensors through the Pix4D software: the panchromatic SEQUOIA and the thermal Flir datasets.

The two DSMs (**Figure 33, Figure 34**) map each pixel altitude from the sea surface and have the same characteristics as the two sensors datasets they were constructed from as shown in **Table 7**.

The DSM elevation values were classified in 5 classes in continuous mode using linear interpolation.

SEQUOIA Panchromatic DSM pixel size	0.02763m
SEQUOIA Panchromatic DSM size (X, Y)	17068x22823 pixels
Flir Thermal DSM pixel size	0.13312m
Flir Thermal DSM size (X, Y)	3741x4628 pixels

Table 7: DSM specifics

Legend

SEQUOIA_DSM (m)
- 124.6
- 129.1
- 133.6
- 138
- 142.5

50   0   50   100   150   200 m
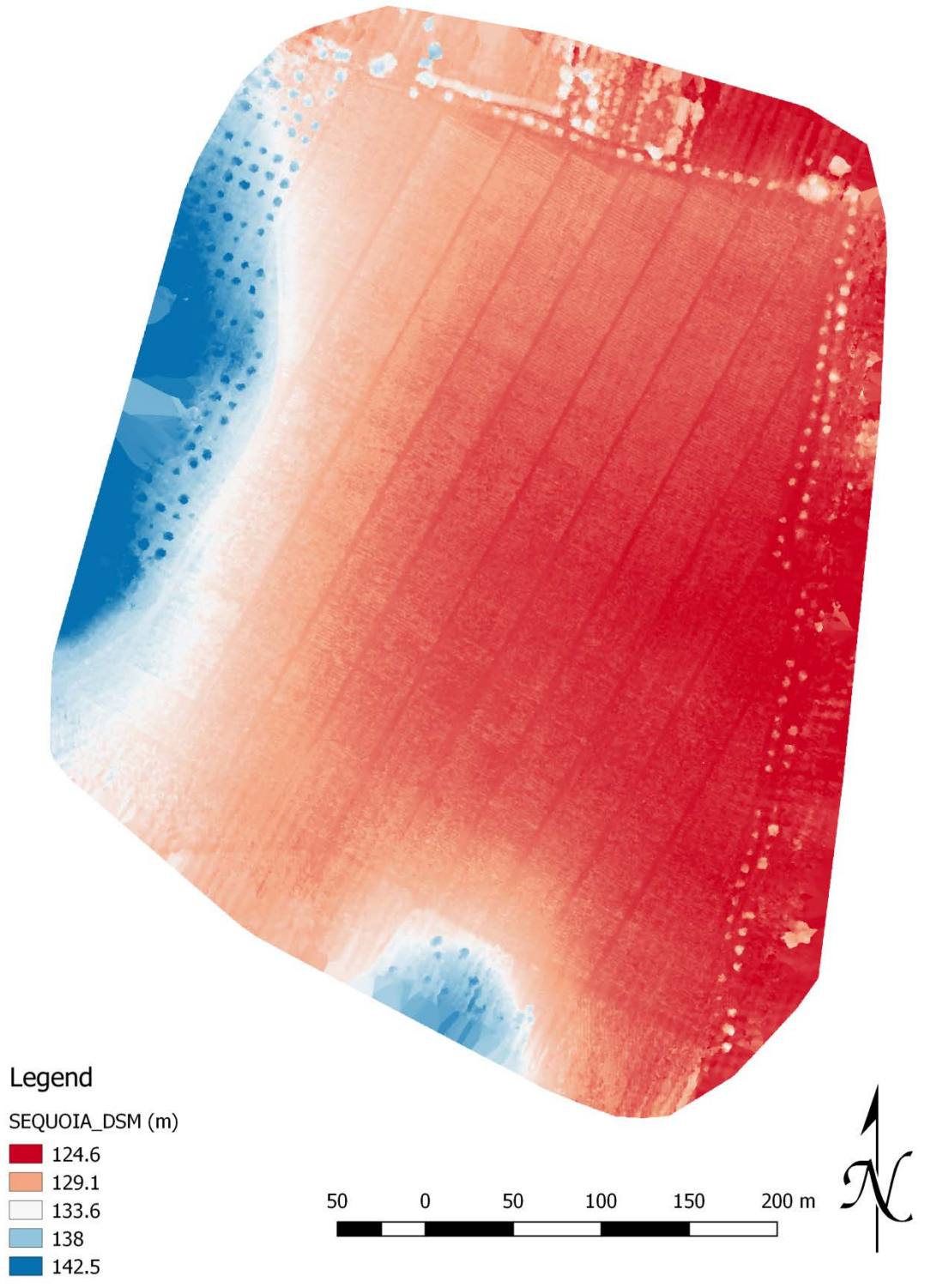
Figure 33: SEQUOIA DSM
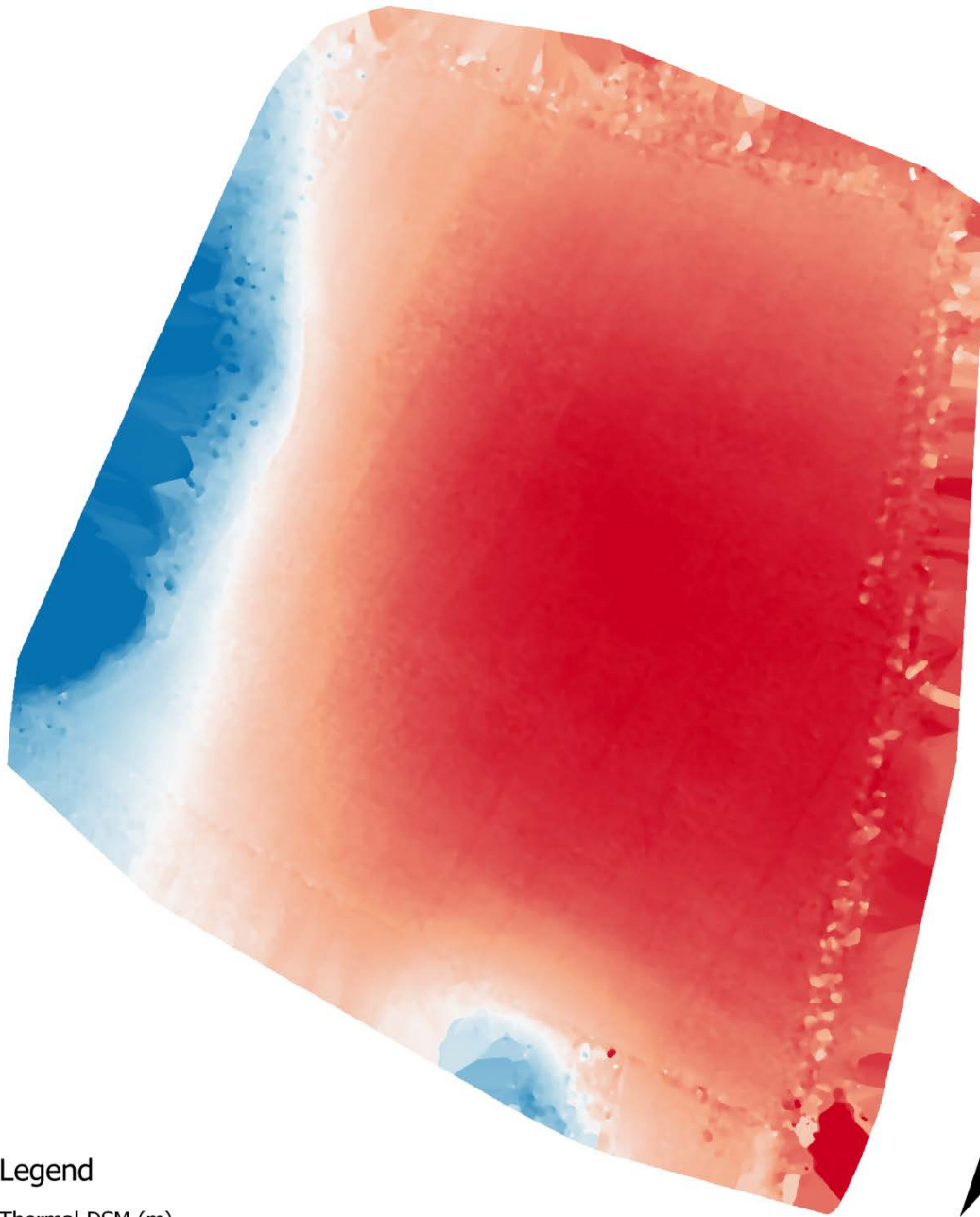
Legend

Thermal DSM (m)

🟥	122.9
🟧	127.8
⬜	132.6
🟦	137.4
🟦	142.2
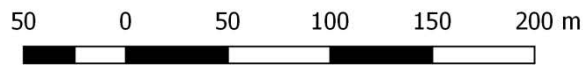
Figure 34: Flir Vue Pro R Thermal DSM

The Digital Surface Models generated are the result of the elevation data from each image shot from the UAV, geolocated, in the process of photogrammetric orthomosaicing.

The first DSM (**Figure 33**) is the mosaic product of the Sequoia panchromatic sensor and its spatial resolution is very high. It can easily be observed that clear elevation differences are visible and computed even between the vines and the underlying soil and vegetation. Trees are clearly distinct as well, providing a method of distinction through height and canopy cover and naturally, the potential to count them.

The second DSM (**Figure 34**) is the product of the orthomosaic generated by the 2nd dataset of thermal camera images, in the same manner as the panchromatic one, and the lower sensor resolution resulted in a DSM of lower spatial resolution, which, however is most useful.

The north-western and south-western hills are clearly depicted in both DSMs as elevation differences from the main vineyard below. This knowledge can only be derived from DSMs as the panchromatic, multispectral and thermal orthomosaics do not show this kind of information at all. The higher the resolution of the DSM, the better the knowledge extracted, as small differences in land height and even plant height may provide agronomic information on irrigation and surface water flow, plants growth comparison and other hidden characteristics to the optical instruments.

The values depicted on the DSM is height above the sea surface as computed by the UAV and the Sequoia GNSS receivers.

The DSM maps were classified in 5 classes in continuous mode using linear interpolation for the values. A higher number in classes e.g. 10 classes in continuous mode at 2m intervals, did not result in more information in discriminating better the vines or other features.

4.4   Hydrology maps

Two algorithmic processes have been employed in order to examine and provide the best results for water flow tracing provided by the QGIS SAGA Flow Accumulation (Flow Tracing) tool. The algorithms used are Rho8 (Fairfield and Laymarie, 1991) and the DEMON algorithm (Costa-Cabral and Burges, 1994) (**Figure 35, Figure 36**).
The hydrology flow values were classified in 5 classes in continuous mode using linear interpolation for best depiction purposes, representing the data range from 2% to 98% of the data values.
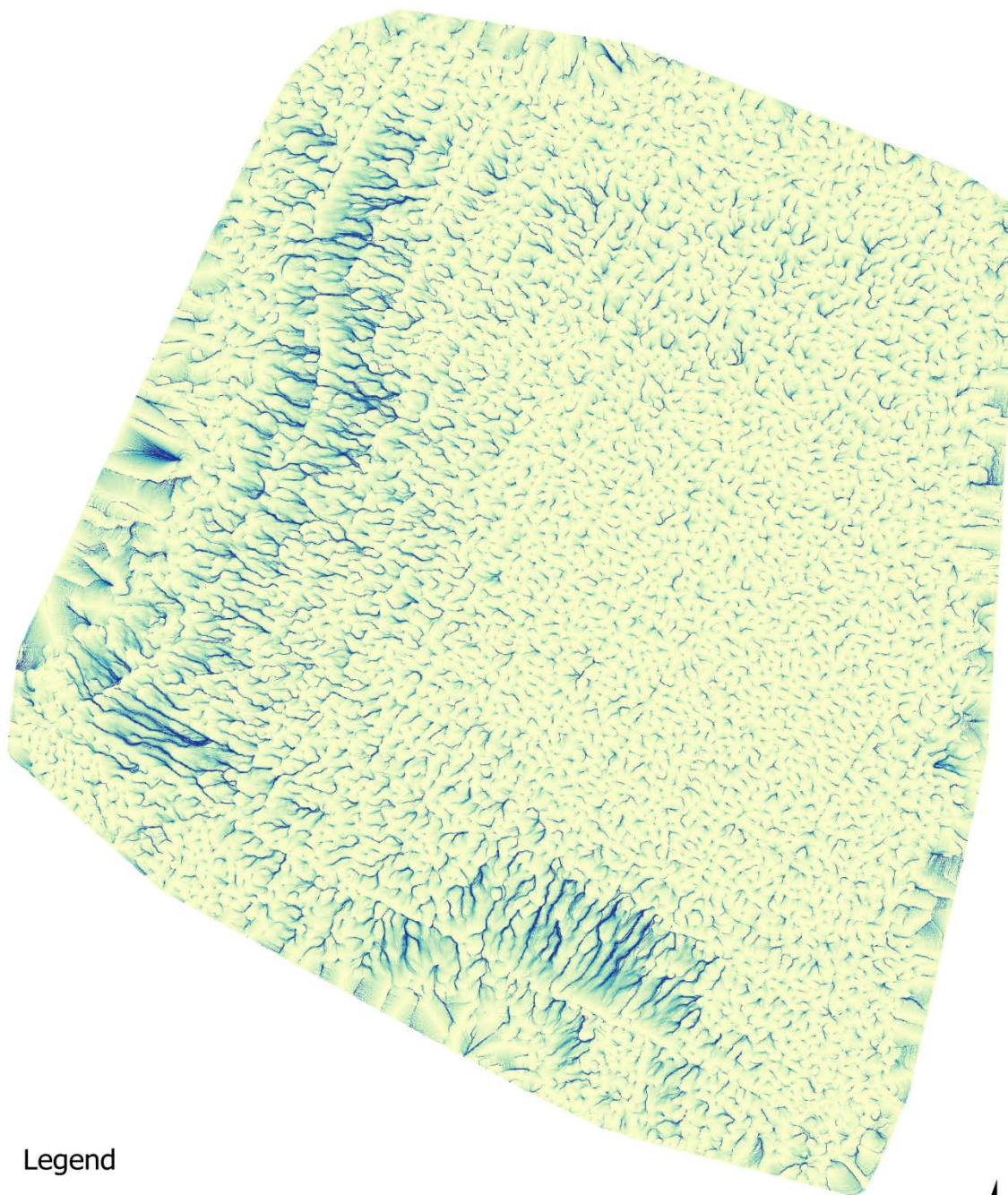
Legend

DEMON flow

	0.0177
	2.15
	4.29
	6.43
	8.56

50   0   50   100   150   200 m
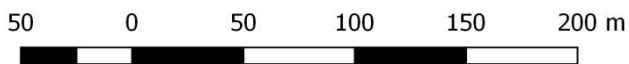
Figure 35: Flir DSM Hydrology map

Legend

Hydro_pan

- 0.000749
- 0.0111
- 0.0215
- 0.0319
- 0.0422
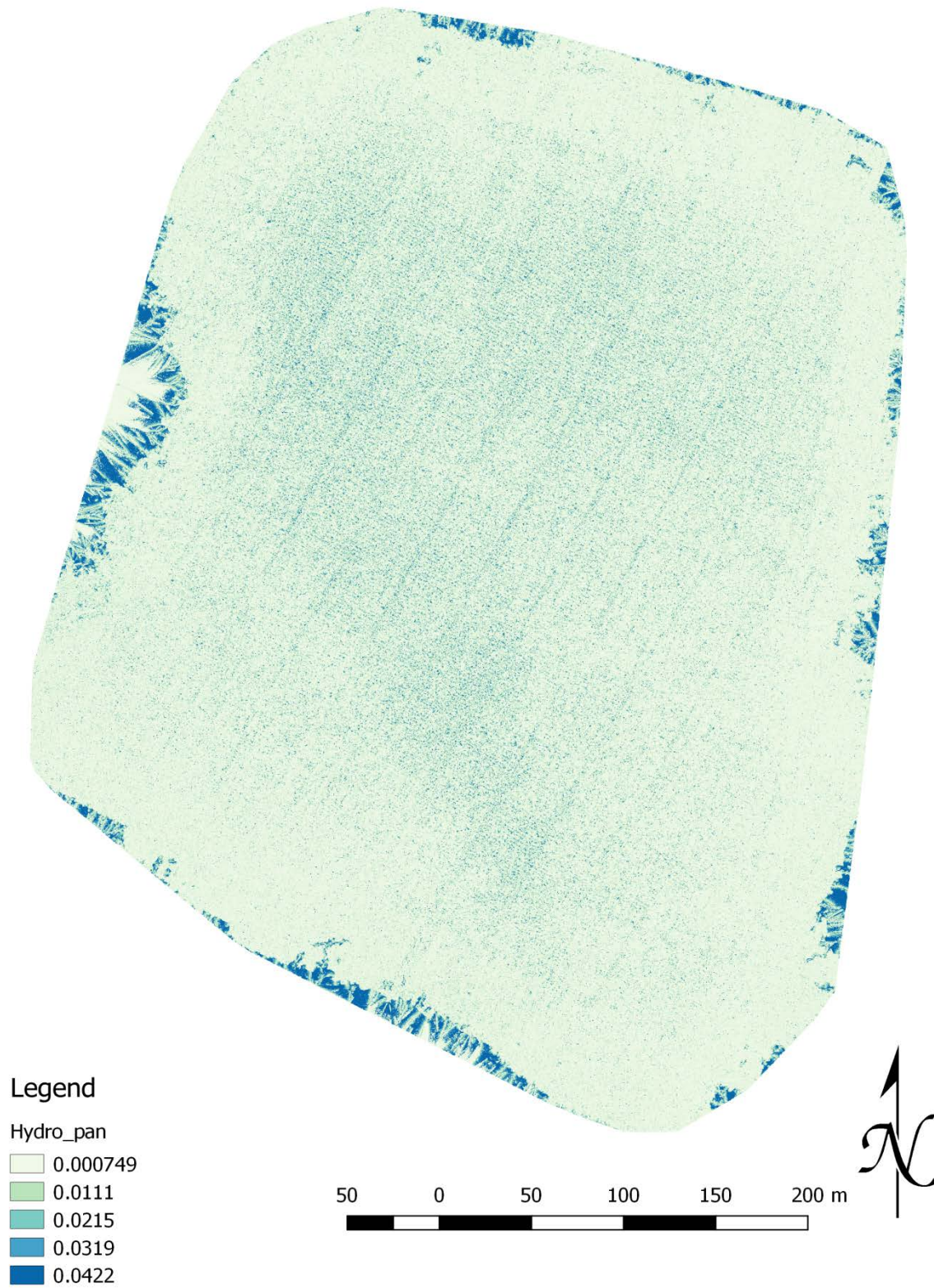
Figure 36: SEQUOIA DSM Hydrology map

Hydrology map from thermal DSM

10 0 10 20 30 40 m
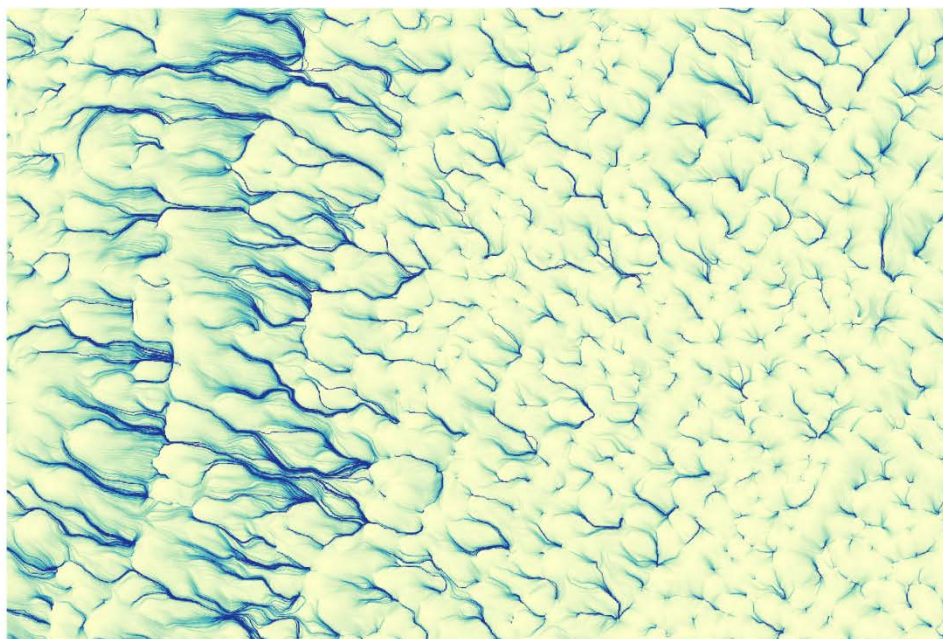
Hydrology map from panchromatic DSM

10 0 10 20 30 40 m
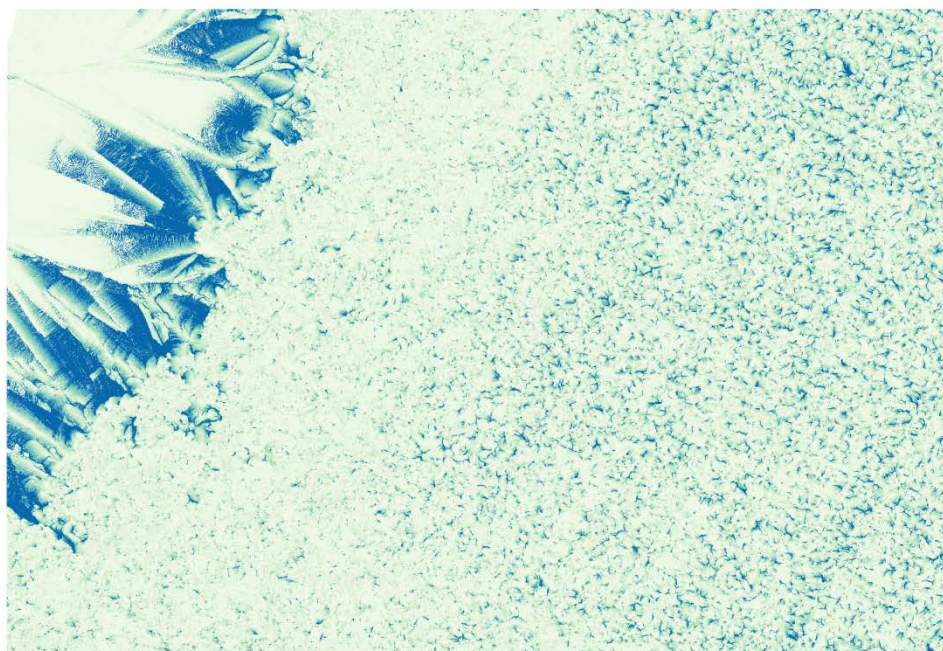
Legend

Hydro_thermal	Hydro_pan
0.0177	0.000749
2.15	0.0111
4.29	0.0215
6.43	0.0319
8.56	0.0422

Figure 37: Detail of the two hydrological maps

The DEMs generated from the panchromatic and thermal orthomosaics are the principle inputs to the **hydrology map generation algorithms**.

Due to different resolutions of the DSM inputs to the hydrology algorithms, the output resolution is also much different. As algorithms use each pixel's elevation data and the neighboring ones to calculate the flow routes and accumulation, the more the pixels, the higher the flow details depicted.

However, the very high resolution of the panchromatic DSM does not allow the clear interpretation of the hydrology map (**Figure 36**). The lower resolution thermal DSM derived hydrology map provides a better view of the hydrological behavior of the area as the pixel elevation data do not make clear differential distinctions between e.g. soil and plants. **Figure 37** shows some detail on the resolution and information difference of the two hydrology maps generated.

The higher resolution SEQUOIA generated DSM also provides the same information, but in detail that is useful only when inspecting subsets of the vineyard.

The fact that the area has two hills surrounding the vineyard was the main reason that in order to provide a consistent water flow map of the entire vineyard as a basin, one would need to depict them as well through the UAV flights.

Examining **Figure 35** of the lower resolution map, it can be shown that rainwater and irrigation water drainage within the vineyard is concentrated in the middle-east part of the vineyard. This feature may be an advantage for the vines in this area, or a disadvantage under specific conditions. For example, high volumes of rainfall during berry growth may result in favorable conditions for the development of fungi or other pathogenic organisms in the roots or the leaves, concentrated in the main area of higher water concentration. Additionally, lower precipitation rates may indicate that vines at the northern and eastern parts of the vineyard might need less watering that the rest, thus managing irrigation accordingly.

Such site-specific features and their correlations with potential hazardous or beneficial impacts, are valuable in decision-making and the management of a vineyard or a future site for a new vines plantation.

4.5 PV Zonal interpretation with ROIs

Analyzing the pilot site maps by photointerpretation and the VIs' values, 10 indicative big regions/zones (**Figure 38, Figure 39**) can be identified with potential issues, some of which can be recognized. Due to the very high resolution and the size of the vineyard, it is possible and useful to inspect and review fragmented areas inside those zones that are hotspots for possible stress identification, optimization or other agricultural care. Those hotspots are exhibited in a selective exemplary manner.
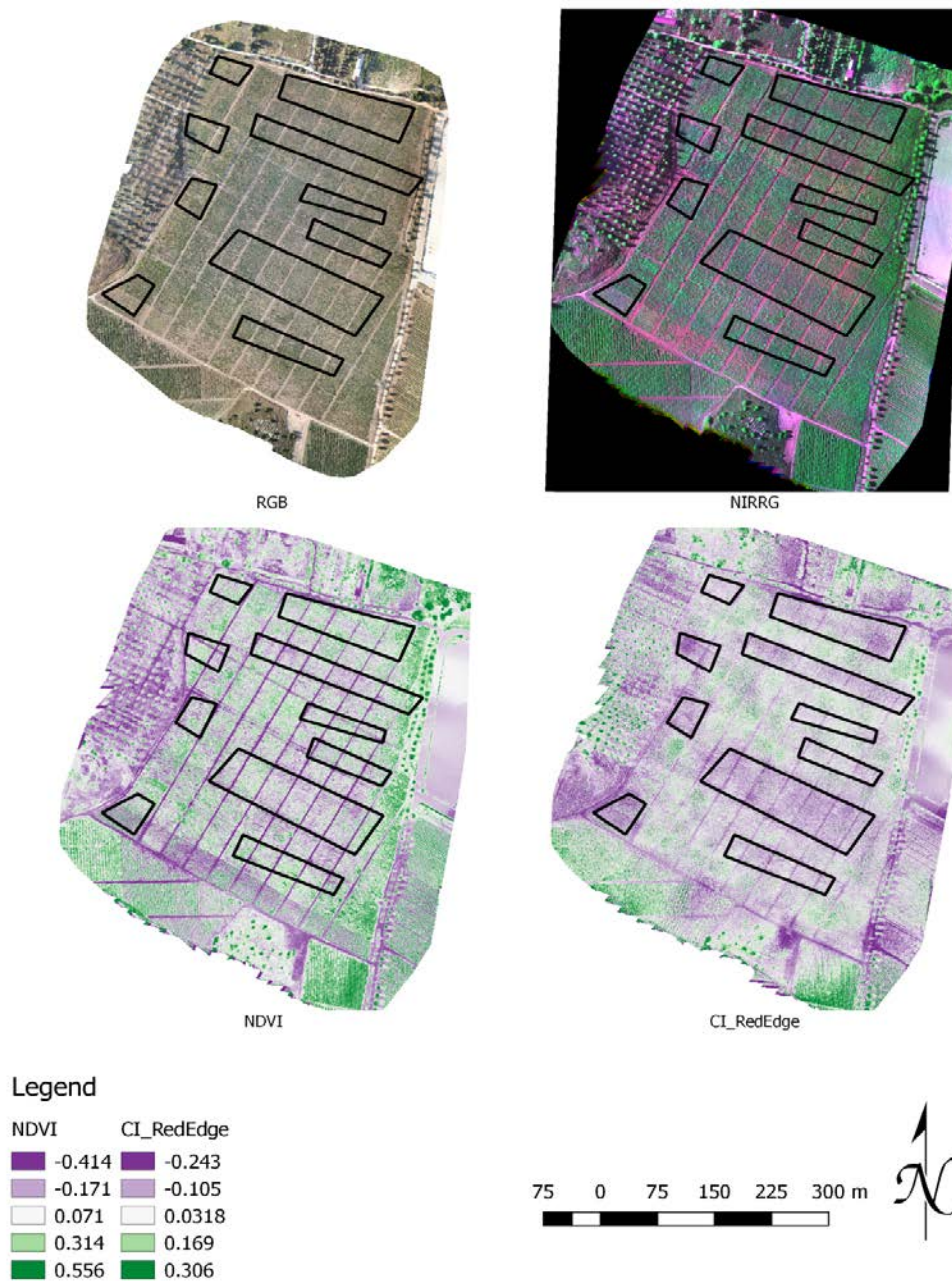
Figure 38: RGB, NIRRG, NDVI, CI-RedEdge orthomosaics with polygons
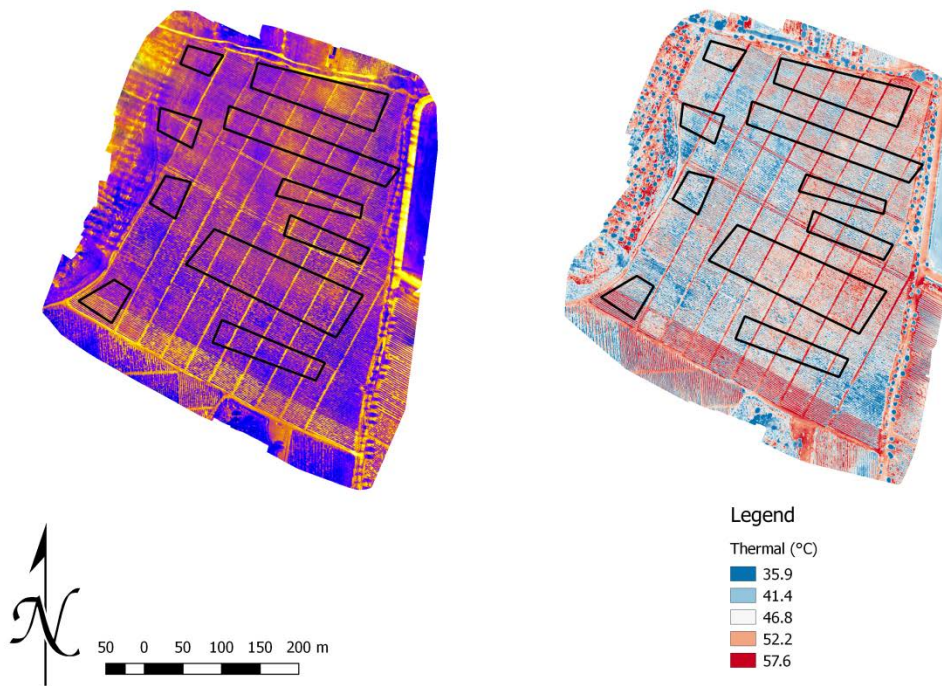
Figure 39: Thermal orthomosaics with polygons
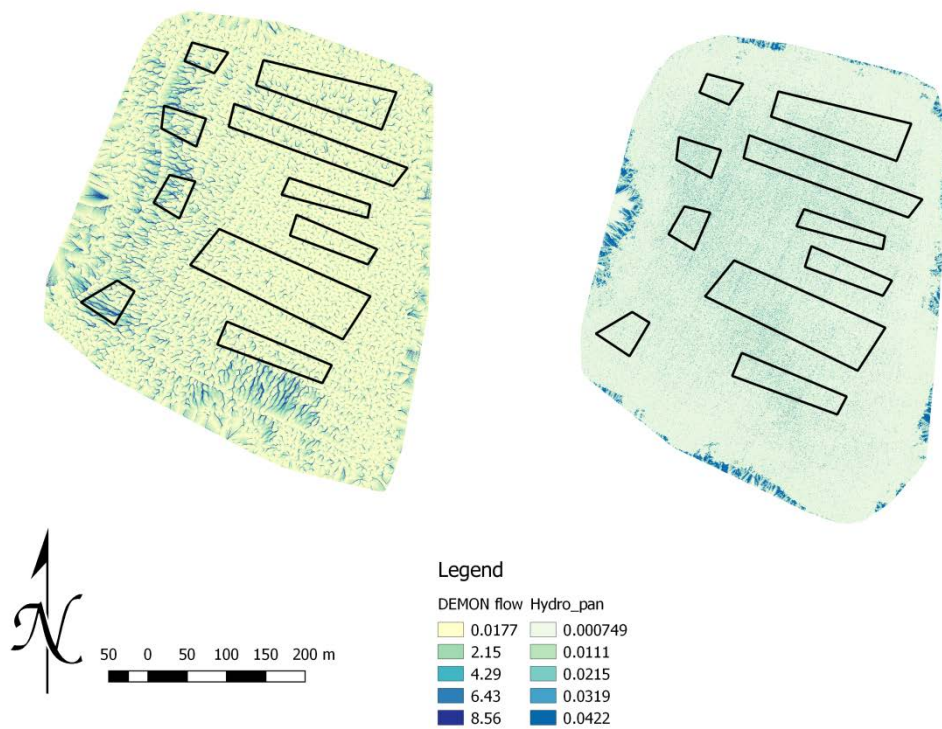
Figure 40: Hydrology maps with polygons
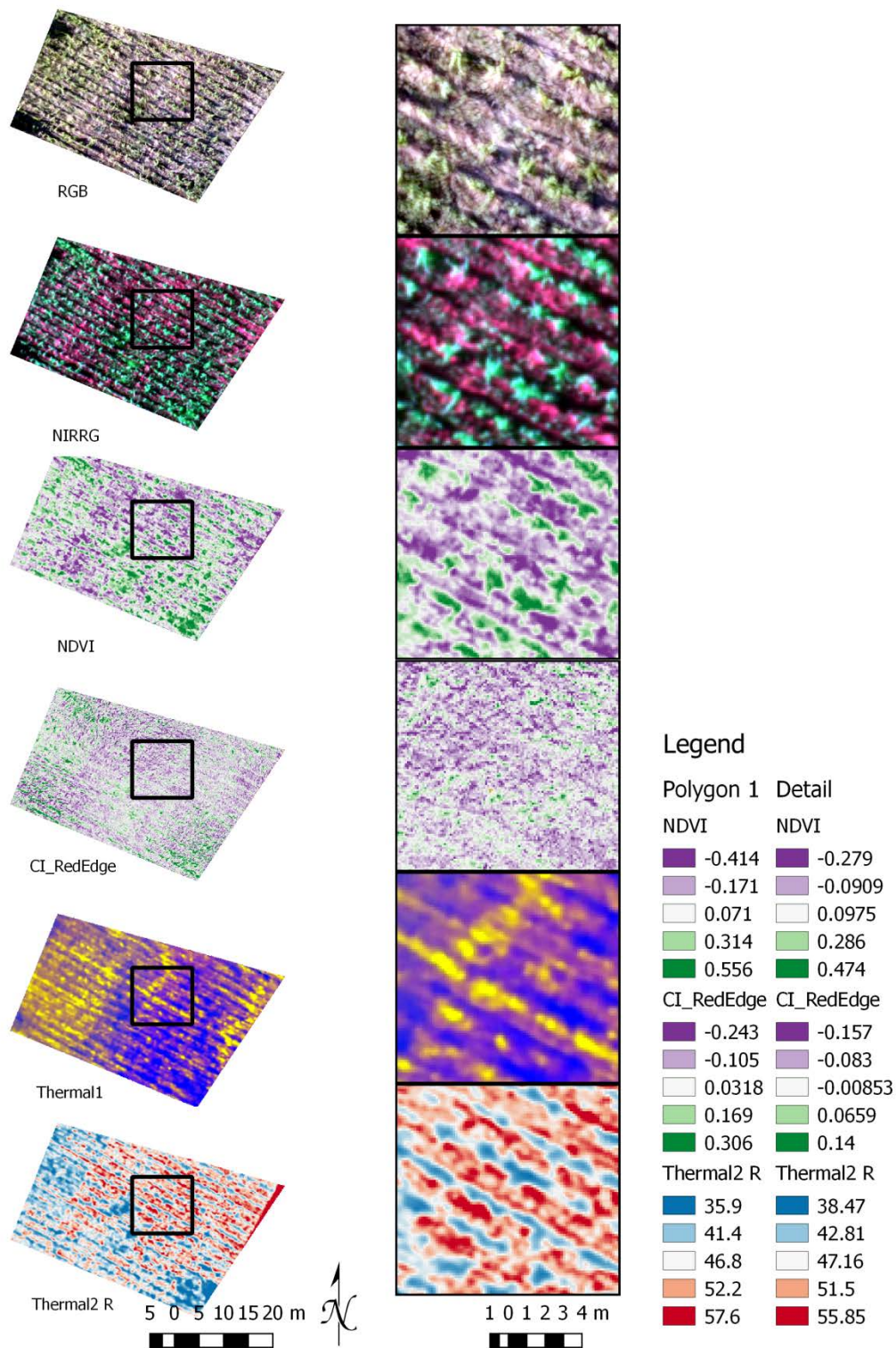
Figure 41: Polygon01 indicative details

RGB

NIRRG

NDVI

CI_RedEdge

Thermal1

Thermal2 R

20 0 20 40 60 80 m

N

1 0 1 2 3 4 m

Legend

Polygon 2

NDVI
- -0.414
- -0.171
- 0.071
- 0.314
- 0.556

CI_RedEdge
- -0.243
- -0.105
- 0.0318
- 0.169
- 0.306

Thermal2 R
- 35.9
- 41.4
- 46.8
- 52.2
- 57.6

Detail

NDVI
- -0.309
- -0.104
- 0.101
- 0.307
- 0.512

CI_RedEdge
- -0.238
- -0.131
- -0.0234
- 0.0839
- 0.191

Thermal2 R
- 39
- 43.6
- 48.2
- 52.8
- 57.4
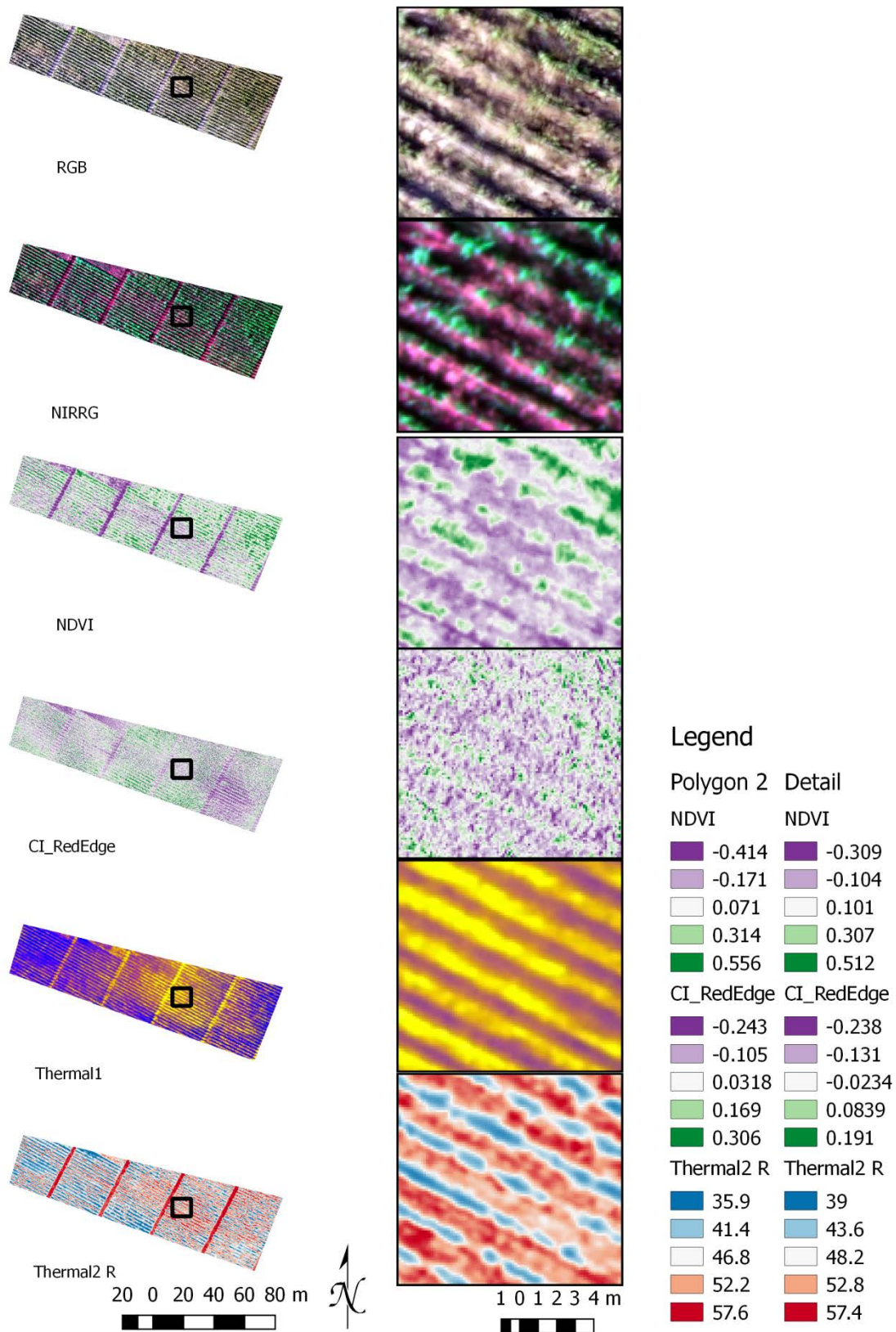
Figure 42: Polygon02 indicative details
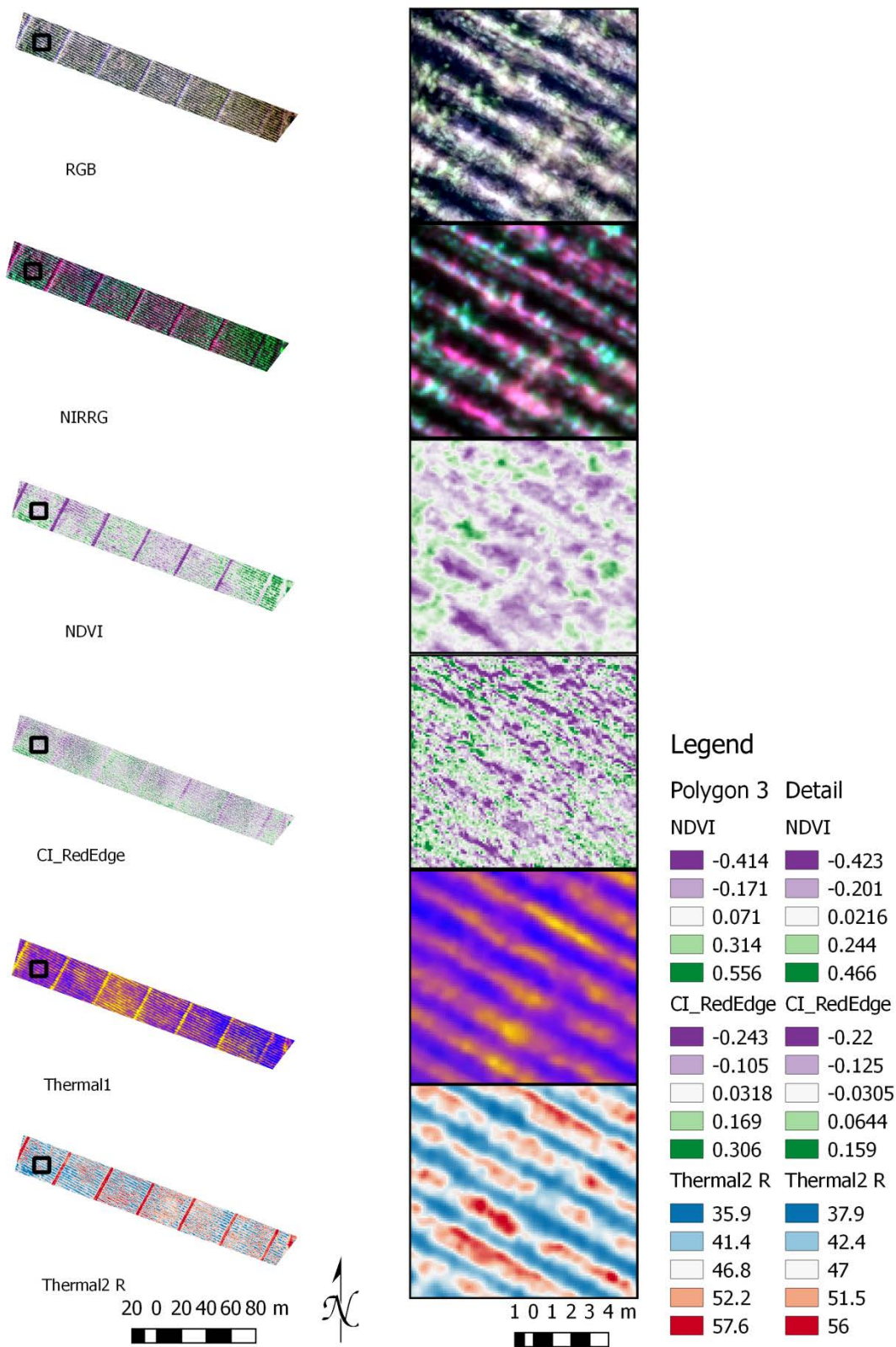
Figure 43: Polygon03 indicative details
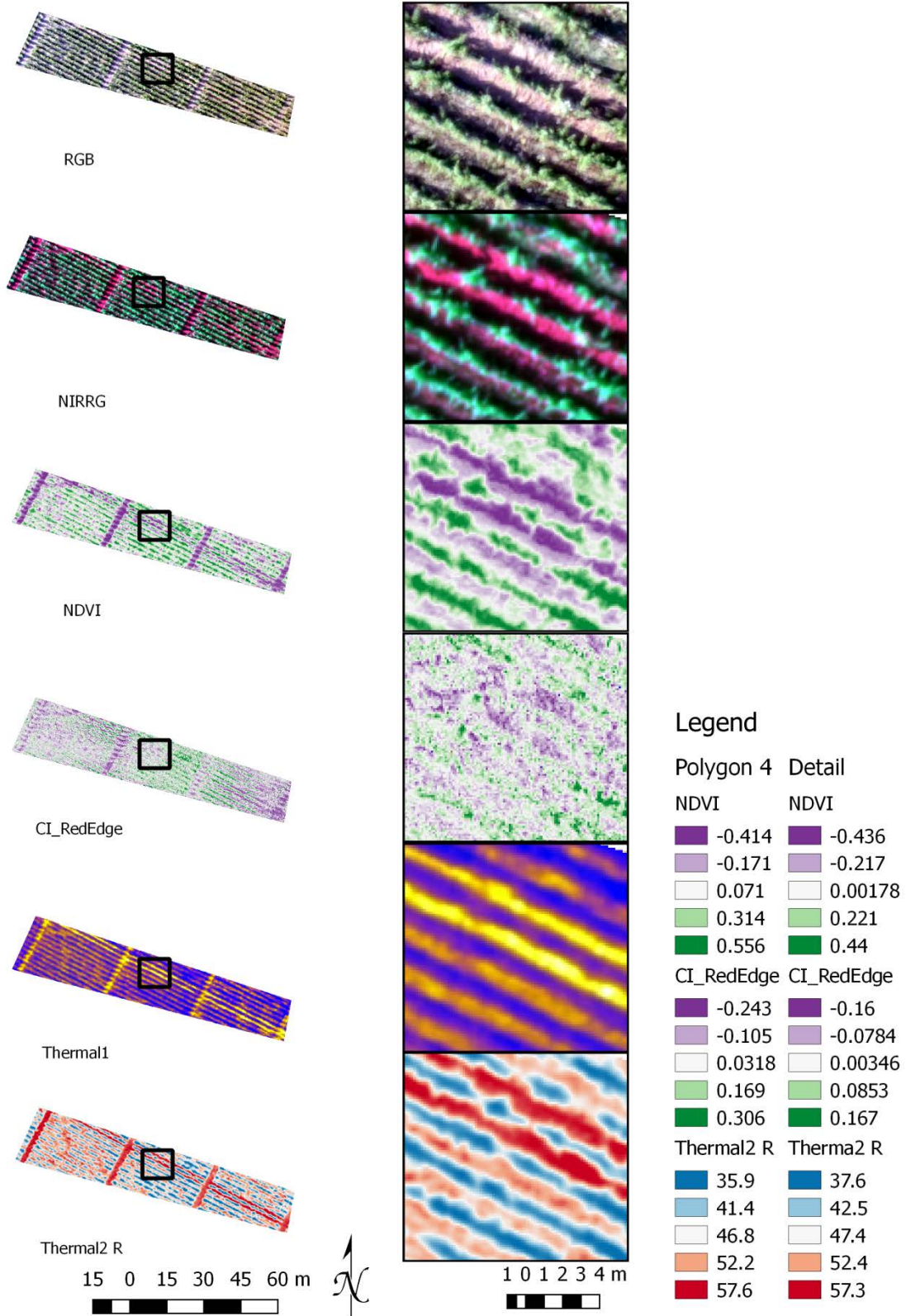
Figure 44: Polygon04 indicative details
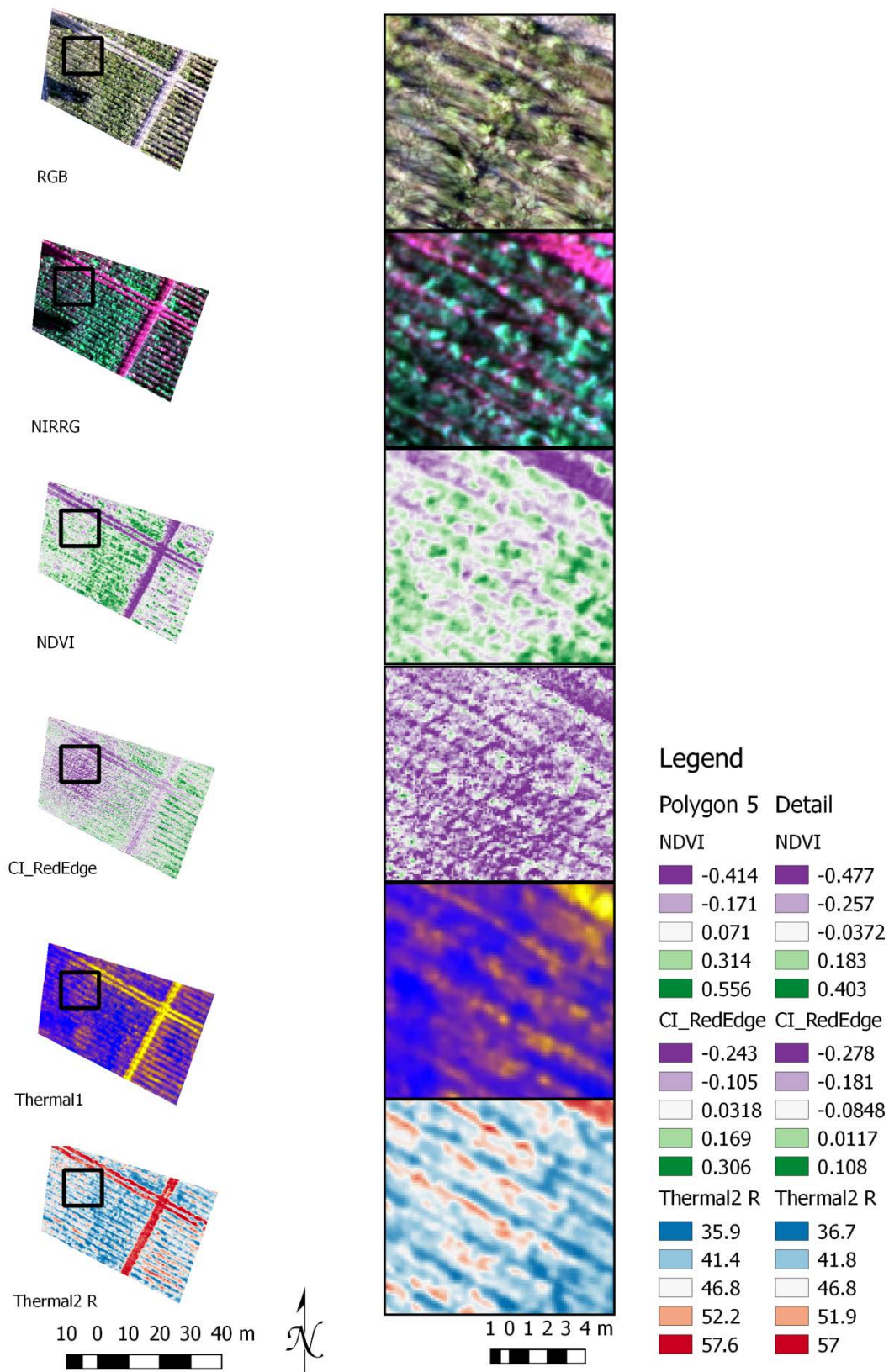
Figure 45: Polygon05 indicative details

RGB

NIRRG

NDVI

CI_RedEdge

Thermal1

Thermal2 R

10 0 10 20 30 40 m

1 0 1 2 3 4 m

Legend

Polygon 5　Detail

NDVI　NDVI

Polygon 5	Detail
-0.414	-0.477
-0.171	-0.257
0.071	-0.0372
0.314	0.183
0.556	0.403

CI_RedEdge　CI_RedEdge

Polygon 5	Detail
-0.243	-0.278
-0.105	-0.181
0.0318	-0.0848
0.169	0.0117
0.306	0.108

Thermal2 R　Thermal2 R

Polygon 5	Detail
35.9	36.7
41.4	41.8
46.8	46.8
52.2	51.9
57.6	57

79
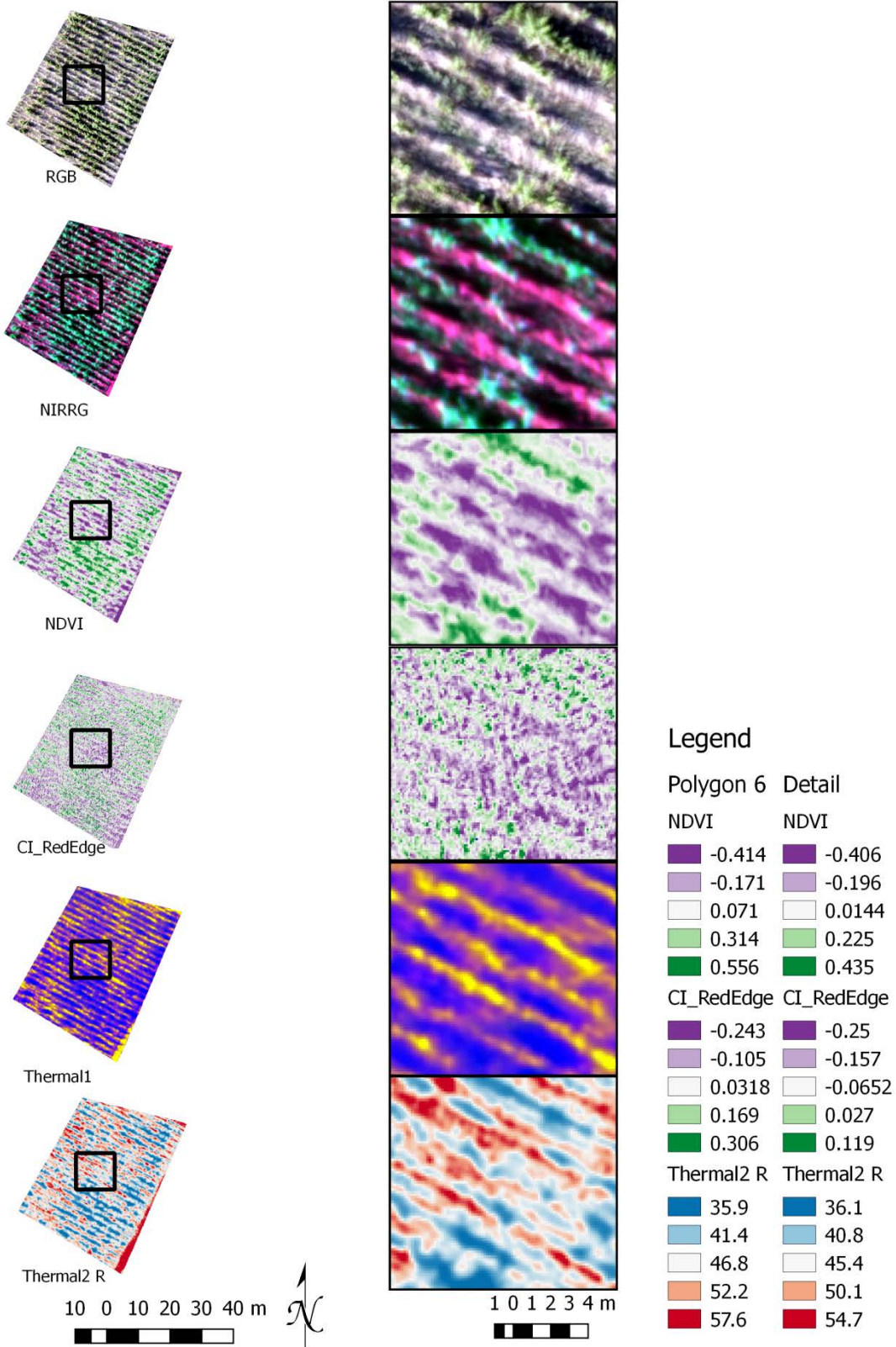
Figure 46: Polygon06 indicative details

RGB

NIRRG

NDVI

CI_RedEdge

Thermal1

Thermal2 R

10 0 10 20 30 40 m

Legend

Polygon 7   Detail

NDVI   NDVI

-0.414   -0.433
-0.171   -0.207
0.071   0.0187
0.314   0.245
0.556   0.471

CI_RedEdge   CI_RedEdge

-0.243   -0.176
-0.105   -0.0878
0.0318   -3.6e-05
0.169   0.0878
0.306   0.176

Thermal2 R   Thermal2 R

35.9   36.6
41.4   41.8
46.8   46.9
52.2   52.1
57.6   57.3

1 0 1 2 3 4 m
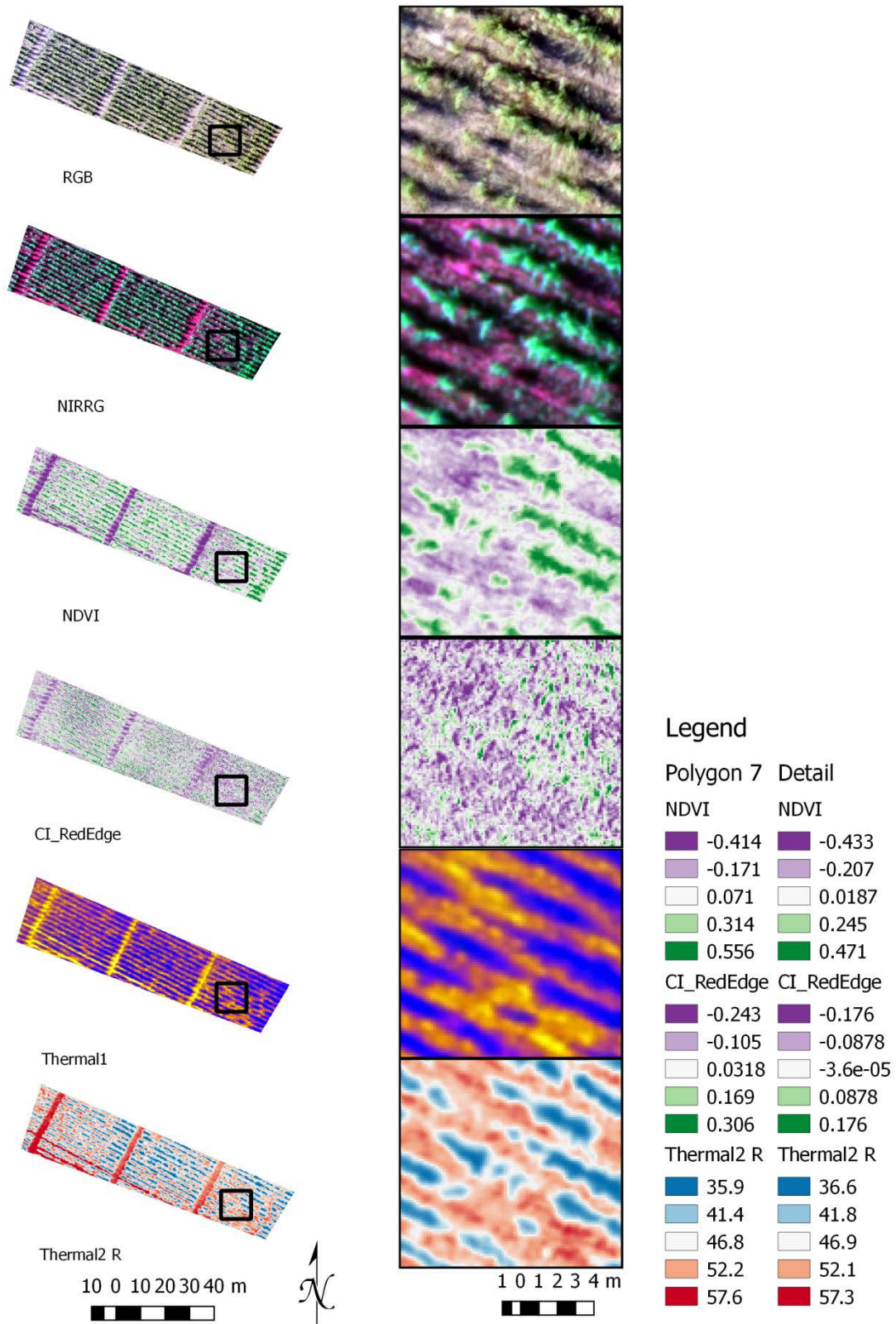
Figure 47: Polygon07 indicative details

RGB

NIRRG

NDVI

CI_RedEdge

Thermal1

Thermal2 R

20 0 20 40 60 80 m

3 0 3 6 9 12 m

Legend

Polygon 8   Detail

NDVI   NDVI
-0.414   -0.452
-0.171   -0.231
0.071   -0.0104
0.314   0.21
0.556   0.431

CI_RedEdge   CI_RedEdge
-0.243   -0.227
-0.105   -0.137
0.0318   -0.0463
0.169   0.0442
0.306   0.135

Thermal2 R   Thermal2 R
35.9   38.2
41.4   42.9
46.8   47.7
52.2   52.4
57.6   57.2
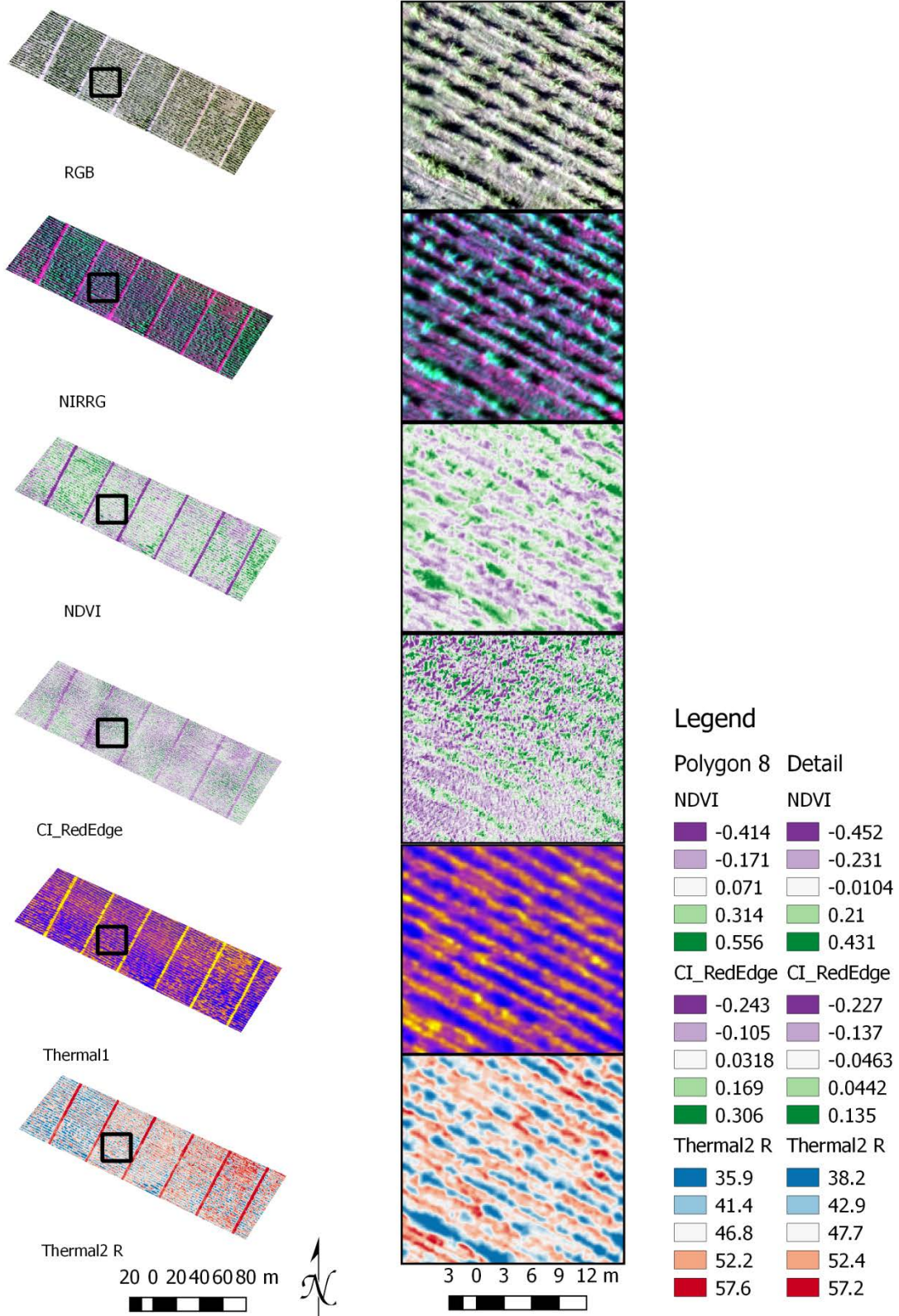
Figure 48: Polygon08 indicative details
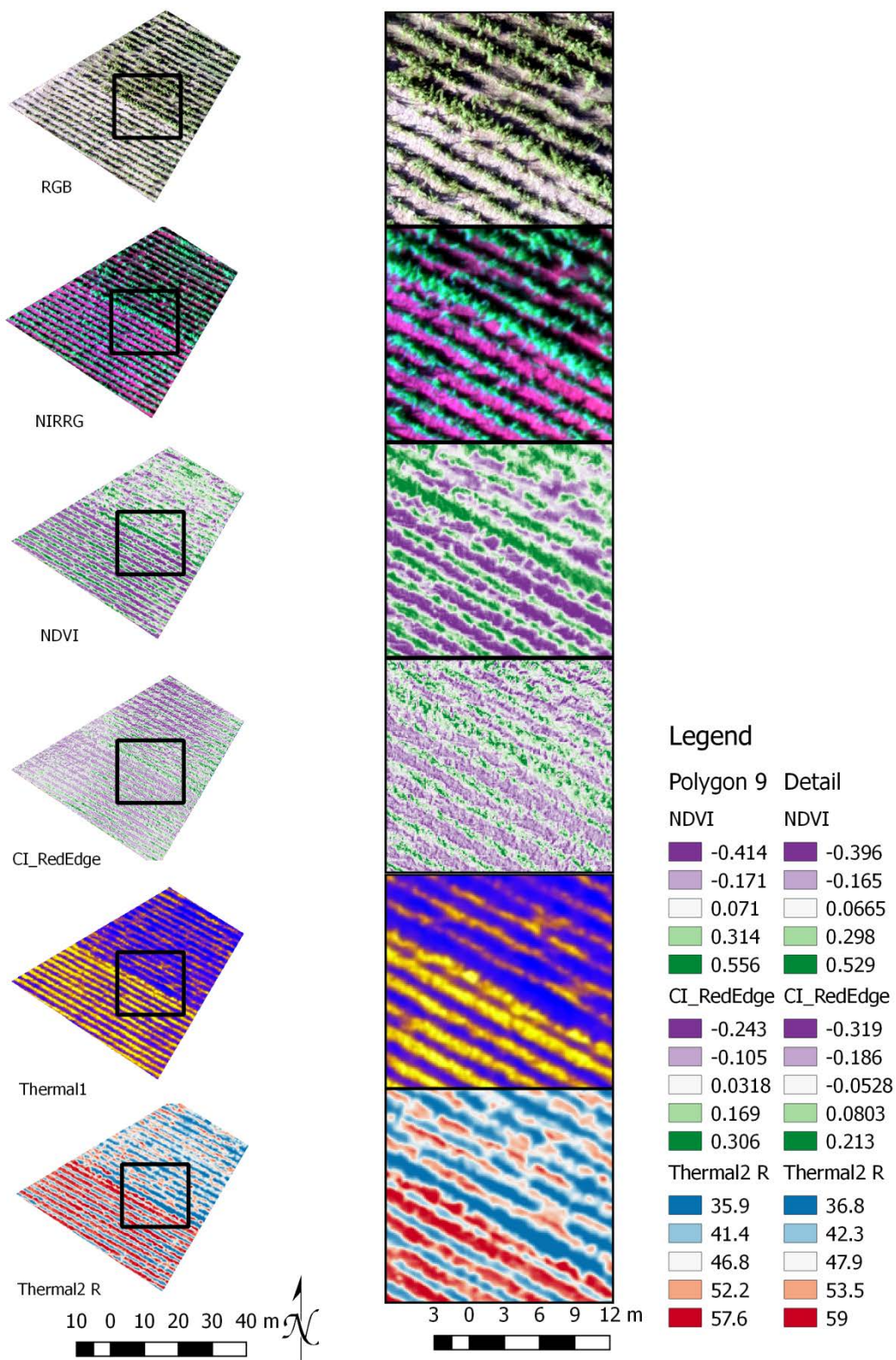
Figure 49: Polygon09 indicative details

RGB

NIRRG

NDVI

CI_RedEdge

Thermal1

Thermal2 R

15 0 15 30 45 60 m

2 0 2 4 6 8 m

Legend

Polygon 10 Detail

NDVI		NDVI	
■	-0.414	■	-0.441
■	-0.171	■	-0.213
□	0.071	□	0.016
■	0.314	■	0.245
■	0.556	■	0.473

CI_RedEdge		CI_RedEdge	
■	-0.243	■	-0.193
■	-0.105	■	-0.103
□	0.0318	□	-0.0141
■	0.169	■	0.0753
■	0.306	■	0.165

Thermal2 R		Thermal2 R	
■	35.9	■	36.9
■	41.4	■	41.7
□	46.8	□	46.5
■	52.2	■	51.2
■	57.6	■	56
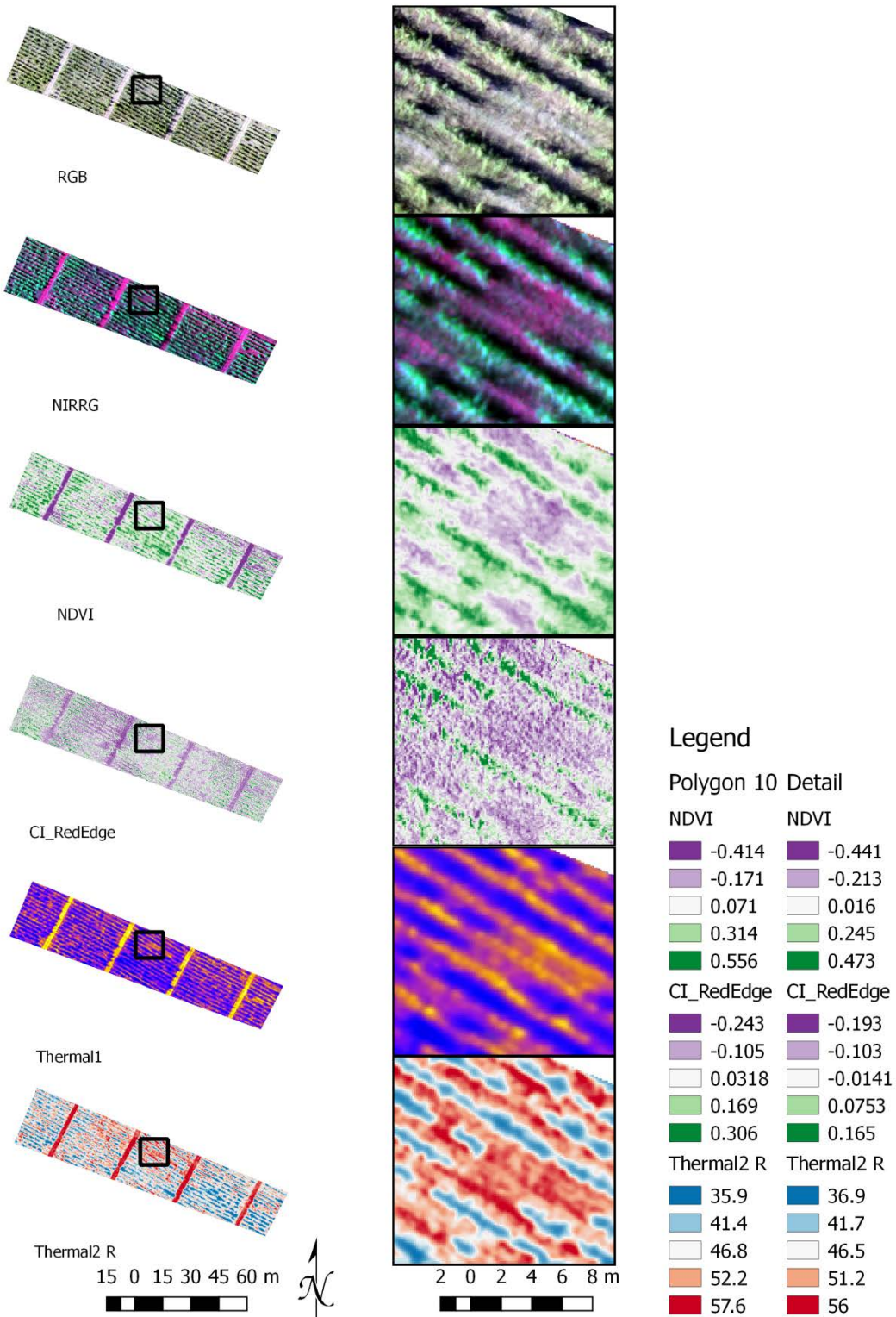
Figure 50: Polygon10 indicative details

4.5.1 Qualitative interpretation

The 10 zones (**Figure** 41**, Figure 42, Figure 43, Figure 44, Figure 45, Figure 46, Figure 47, Figure 48, Figure 49 and Figure 50**) are classified in the same manner as the original orthomosaics, in 5 classes, linearly interpolated in continuous mode, representing the data range from 2% to 98% of the data values. The square hotspots in the highest detail view are also classified in the same manner with the difference that the lowest and highest values represented are the ones inside the square itself. This allows a better viewing condition with higher distinguishing results between the different classes, and thus features under observation. Higher upper and lower limits as calculated in both VIs in the full extent of the area depicted would provide more obscure optical results.

The regions under detailed observation and the corresponding polygons generated have been chosen mainly by observing the Red Edge Chlorophyll Index orthomosaic, as it provides the most valuable quality of vegetation knowledge: The photosynthetic ability of the plants.
The assessment of the CI_RedEdge as the most potent VI to indicate the zones to be further examined, involves the correlation with the corresponding information shown in the other orthomaps: the RGB and NIRRG composites, the NDVI and the thermal maps.

Throughout the identified zones, the variability factors under consideration vary greatly. Usually a combination of these factors comprise the remotely sensed output.

- Missing vines:
  It can be easily seen that there is a great extent of areas with missing plants. A moderate estimation could claim that the vineyard has a missing potential of a tens of hundreds extra vines. This is easily translated in a serious amount of productivity loss;

- Lower vine growth rate or senescence due to watering, fertilization, infestation and other stress factors, as shown by the VIs;

- Younger vines, planted later than others. Usually, there can be a zonal discrimination in vines' age as they are planted in different times regionally within a vineyard;

- Higher soil vegetation under the vines and between the vineyard planted rows;

- Anthropogenic activities like ploughing and pruning:
  A small portion of the vineyard has been ploughed and taken care of underlying parasitic vegetation, a very clear aspect shown through all of the aerial maps. The parts that have clean soil and lack any other vegetation than vines, show clearly the status of the plants and provide high quality results in order to assess even each plant by itself or multiple ones in the same area.

Figure 51: Ploughed and untreated areas

In **Figure 51**, the distinctions are clear: At the southernmost part some rows have been ploughed, while on the rest of the central vineyard, the vegetation between the vine rows is high and flourishing. Additionally, one can observe surrounding vineyards which enjoy a very high level of attention and compare the different cultivation practices or the lack of them. Ploughing and pruning have been exercised professionally and in a homogeneous and rational manner.

- Irrigation, precipitation and hydrological features:

The hydrology maps show that the naturally formed water basin leads the water flow and drains from the western and southern hills surrounding the vineyard towards the center and the furthermost eastern and northern parts. This particular observation could possibly add some insight towards the explanation of the vigor of the sentinel vines in the eastern and northern sides of the vineyard, while lacking such vegetation growth elsewhere.

The critical months for vineyard growth in spring and early summer have been characterized by heavy and periodical rainfall without periods of drought or high temperatures, providing a promising environment for vegetation growth.

In the current vineyard under inspection there is artificial irrigation. However, due to the continuous spring rainfall, almost in every area in Greece and the specific region, viticulturists did not irrigate the grapevines both because of the necessity lack and because it would probably harm or cause potential complications to the plants health from e.g. fungi development and as a result inferior products in quality and quantity.

- Topography: Some parts of the vineyard are on hillsides which may pose irrigation issues through soil imperviousness and water runoffs and higher (or lower) exposure to weather elements.

- Plants and vegetation thermal conditions. In the ROIs and generally within the inspected area, the variabilities in temperature mapped can provide multiple indications. The parasitic vegetation within the vineyard inserts a serious noise factor to the thermal readings and the discrimination of vines as the temperatures of high vegetation has close or identical values with that of vines. In this manner, the best way to thermally depict a vineyard is past a complete ploughing. The example of **Figure 52** shows vividly the scales of the discernable depiction levels as determined by the different ploughing status.
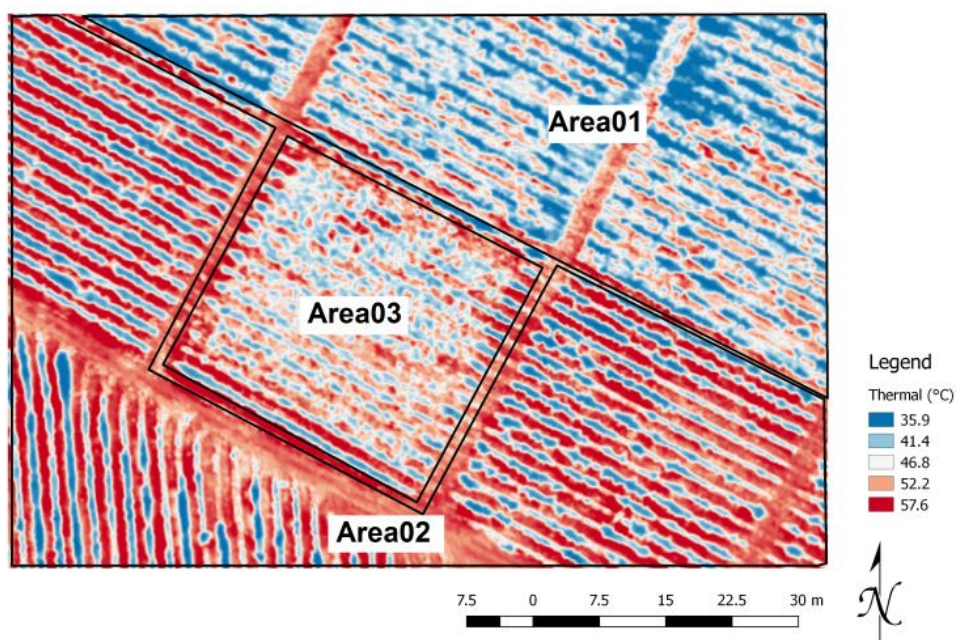
Figure 52: Thermal dataset fragment

Area01 is evidently non ploughed in terms of recognizable recent activities. Herbs, plants and vines are hardly discriminated except for the bare soil areas or soil with very few plants that show a few degrees higher temperature. In such specific areas remotely sensed agronomical information is difficultly derived and uncertain. However, when interpreted in a zonal approach, areas with higher vegetation temperatures in general may indicate irrigation issues, insect infestations etc. or even the need for ploughing and agronomical care, especially after the application of fertilizers.

Area02 has been very recently ploughed and the results are very comprehensible. The vigor differentiation from size and temperature greatly depicted and even a vine-specific approach could be delivered.

Area03 shows better discriminating features than Area01, like a relatively clear view of the vine rows and their thermal characteristics. The parasitic vegetation shows higher temperatures due to the mixture with soil temperatures probably due to ploughing prior to Area02.

4.5.2 Quantitative interpretation

A quantitative process has been employed in order to explore the transformed knowledge from the indices generation into graphs that embody the difference representation between the whole vineyard and the chosen ROIs under inspection.
The whole vineyard was extracted from the full area surveyed by its **exact borders**.

A **Python** script was written in order to extract the polygon with the 10 ROIs from each VI (**ANNEX 2 – Python script**).
A script in **R programming language**, which can be used in GIS environments for data analytics and statistical information extraction, was written in order to generate comparative graphs and value representations for each ROI individually and for the full polygon area (**ANNEX 1 – R script**).

The whole process was performed through the QGIS platform and the graphs generated are:
- Density graph of the total NDVI values of the vineyard versus the NDVI values of the total 10 ROIs values; Density graph and values frequency histogram of the vineyard's NDVI values (First row of **Figure 53**);
- Density graphs of the NDVI values of the vineyard versus the NDVI values of each individual ROI values (3 last rows of **Figure 53**);
- Density graphs and values frequency histograms for each ROI NDVI values (**Figure 54**);
- Density graph of the total CI_RedEdge values of the vineyard versus the CI_RedEdge values of the total 10 ROIs values; Density graph and values frequency histogram of the vineyard's CI_RedEdge values (First row of **Figure 55**);
- Density graphs of the CI_RedEdge values of the vineyard versus the CI_RedEdge values of each individual ROI values (3 last rows of **Figure 55**);
- Density graphs and values frequency histograms for each ROI CI_RedEdge values (**Figure 56**).

It has to be mentioned that the **optimal process** for these comparative representations would be after an extraction with strict borders of the vines rows within the vineyard. In this manner, the values compared would be only between the vines vegetation indices values and the noisy vegetation would be excluded. This could be achieved through the classification of the highest values from the VIs or the

lowest from the thermal datasets under specific thresholds, while a ploughed vineyard would make this process a lot more robust and accurate.

However, even without the extraction and comparison of the vines alone, most of the comparative value density graphs show clear shifts towards reduced values both for the NDVI and the CI_RedEdge VIs. The differences are small both due to the parasitic vegetation concentrations and because of the relatively large polygons.

This comparative representation has the potential to be manually deployed in one map for the recognition of the zones and then applied to multiple other maps in an automatized way evaluating:

1. The initial choice of the zones under consideration
2. The correlations between the generated results
3. A time consistent perspective to the zonal approach
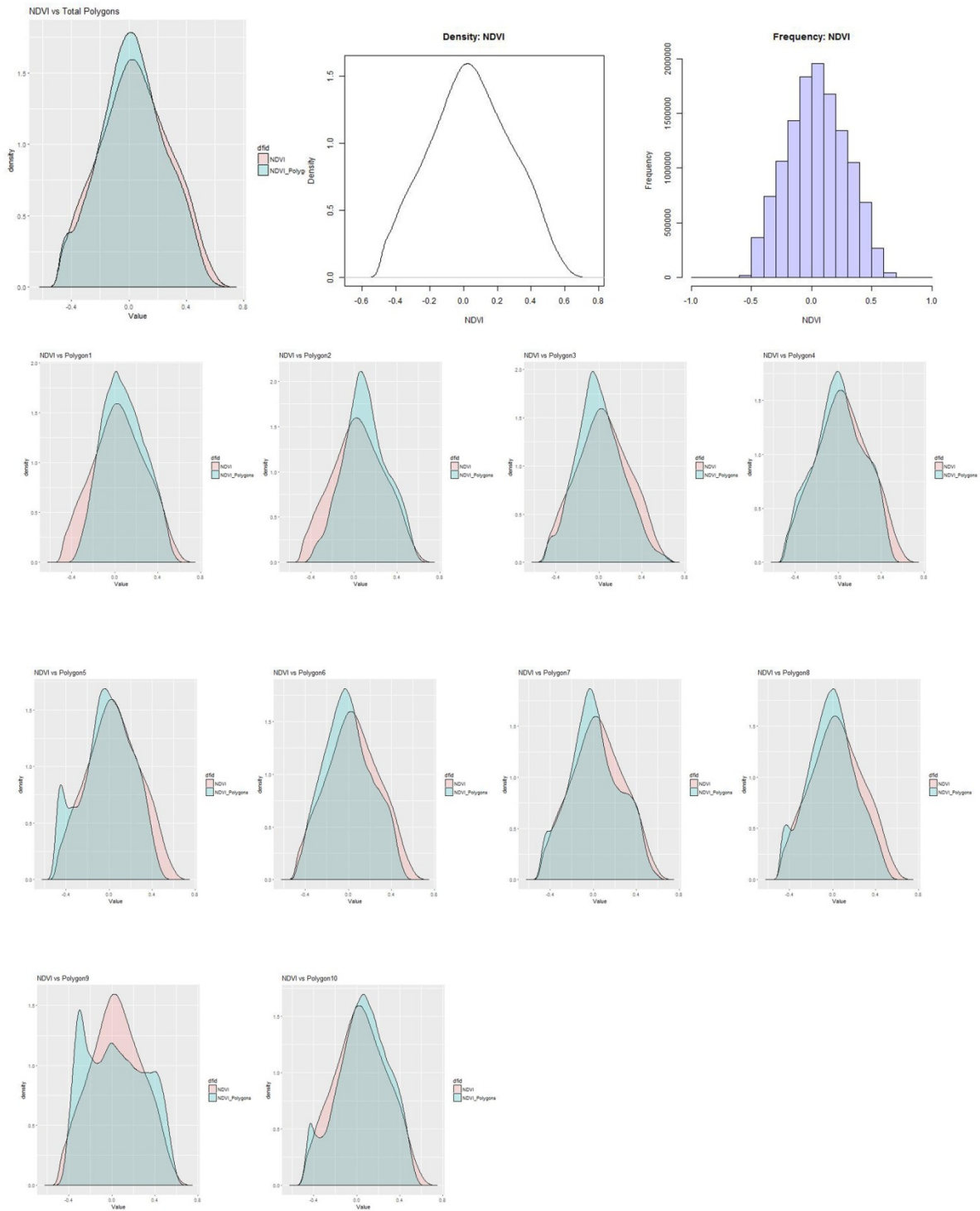
Figure 53: Comparative density graphs for the NDVI values
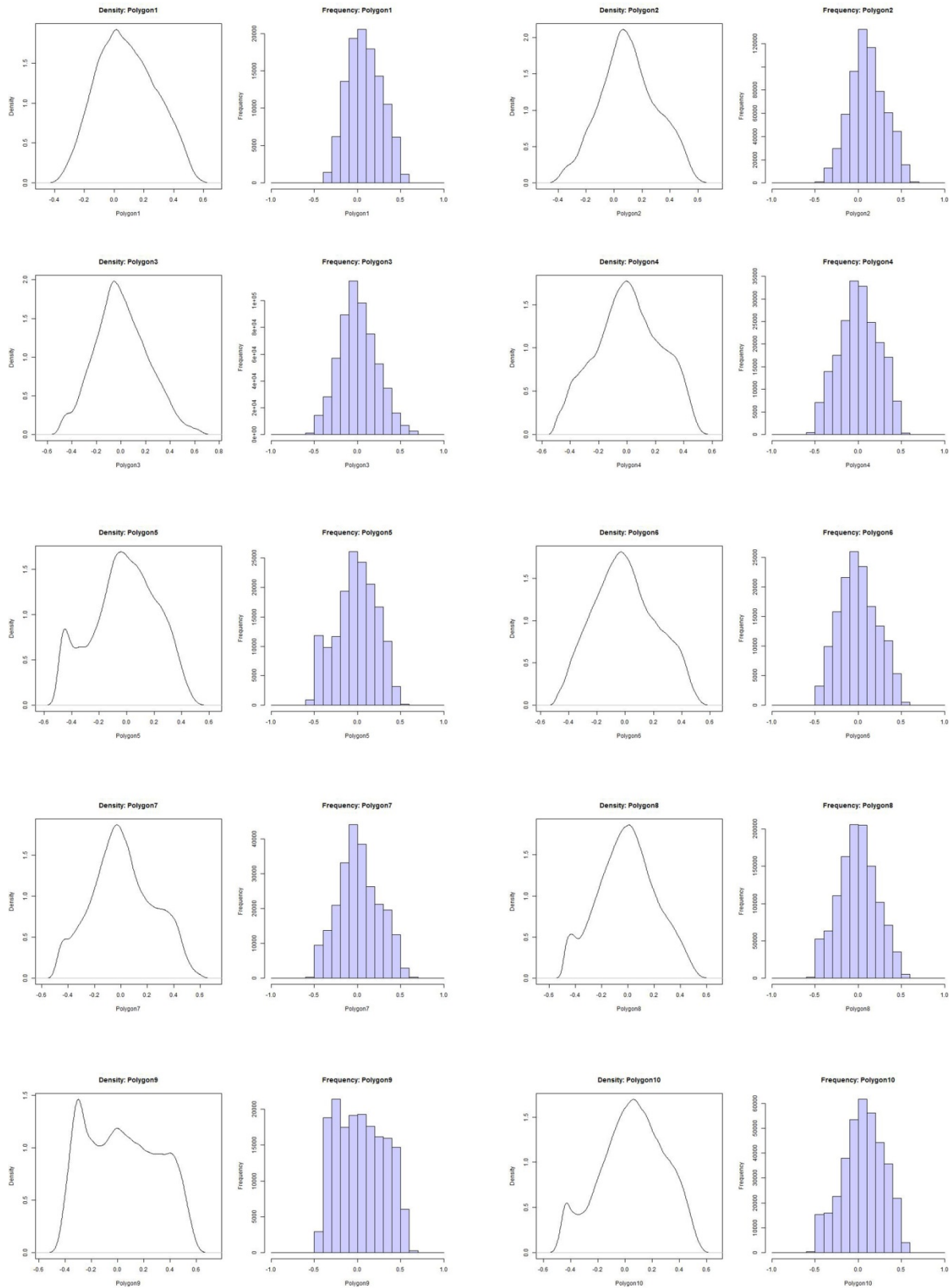
Figure 54: Density graphs and frequency histograms for each ROI NDVI values
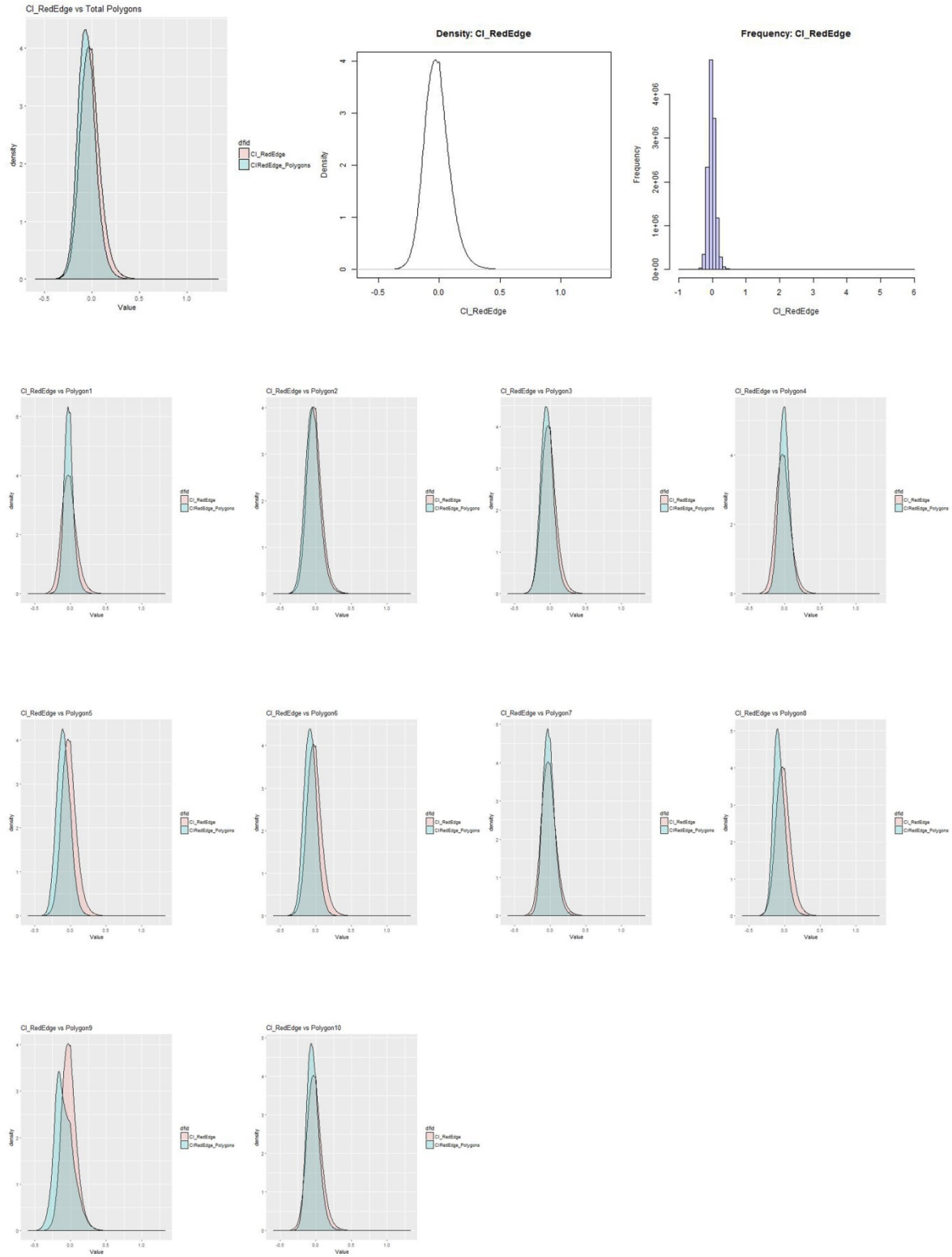
Figure 55: Comparative density graphs for the CI_RedEdge values
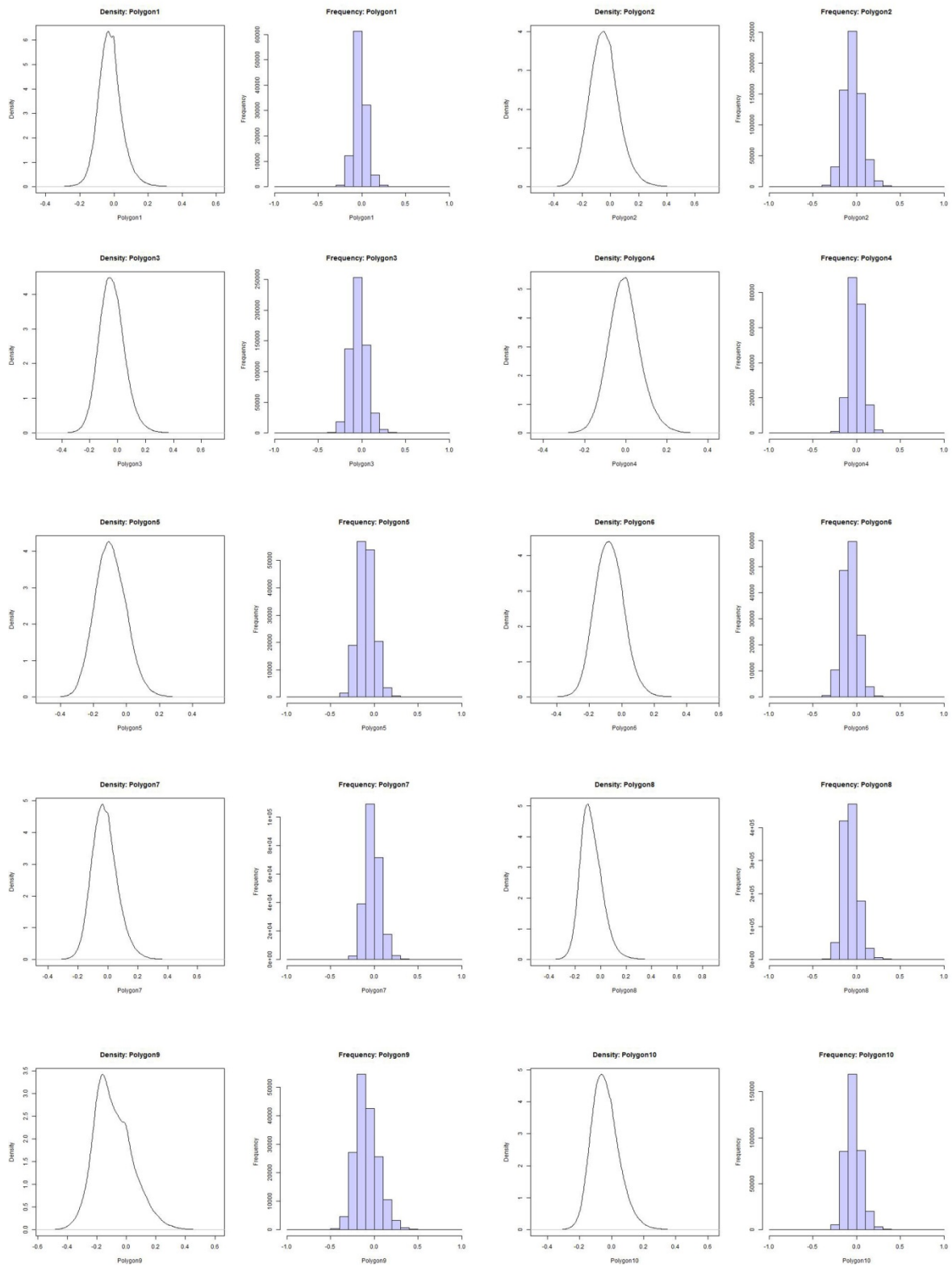
Figure 56: Density graphs and frequency histograms for each ROI CI_RedEdge values

4.6 Sentinel-2A data

The evaluation of the Sentinel-2 MSI payload capacity in the vineyard observation is exhibited through the generation of a time series products throughout summer 2017, when the vines are already blooming, anthropogenic activities are mainly executed and it is the most important period for vines.

The products presented in **Figure 57 and Figure 58** are the RGB true color composite, the NIR-Red-Green false color composite and the two VIs utilized for the UAS imagery, the NDVI and the Red Edge Chlorophyll Index (CI_RedEdge).

For CI_RedEdge, the 20m resolution data from the Red Edge band were resampled to 10 meters pixel size in order to compute the index to the best resolution available. Resampling the 20m products is possible as the 10m pixels size is a multiple of the 20m pixel size. The resampling is performed with the nearest neighbor algorithm.

The NDVI and CI_RedEdge values were classified in 5 classes in continuous mode using linear interpolation for best depiction purposes, representing the data range from 2% to 98% of the data values.
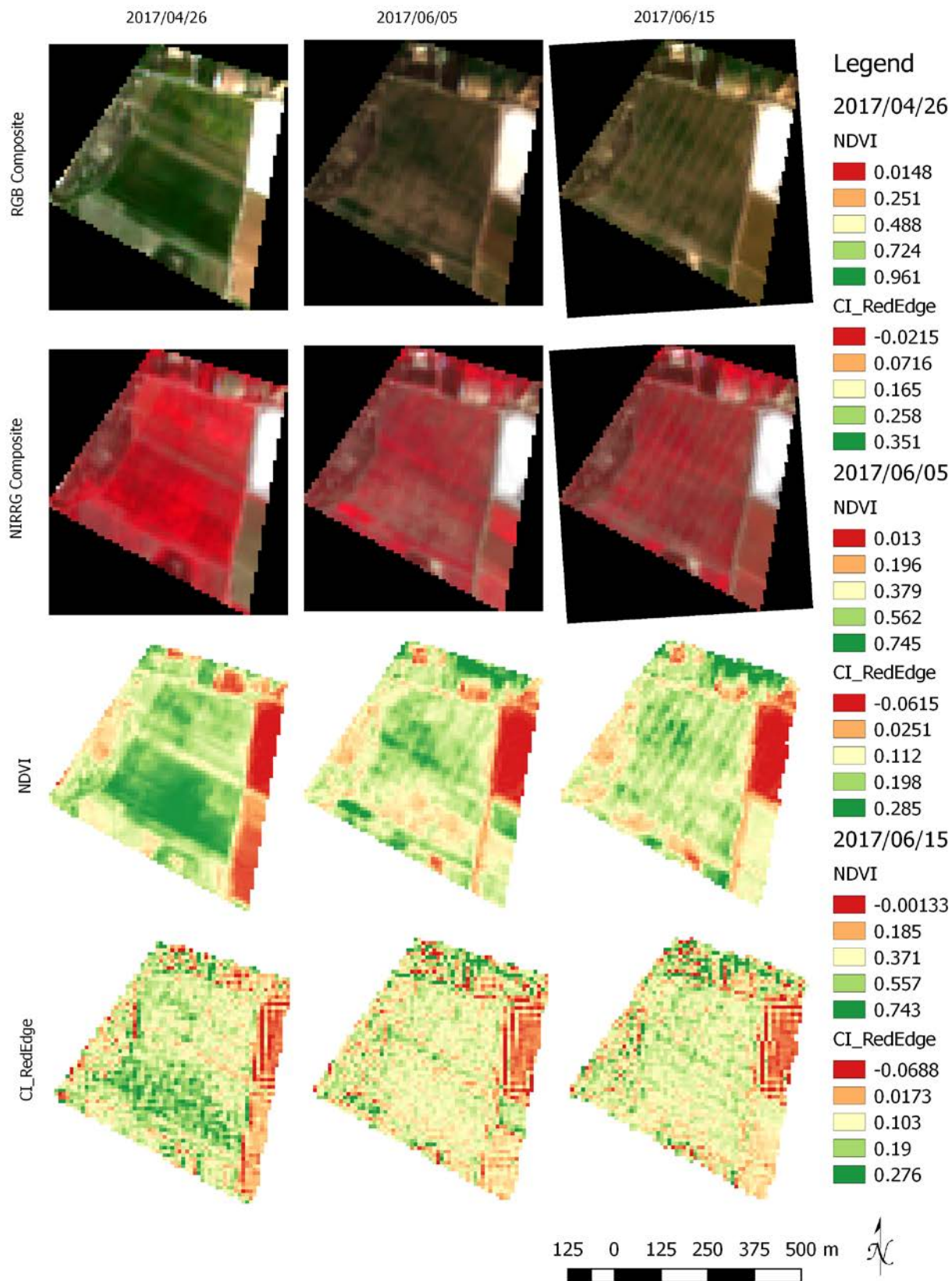
Figure 57: S2 VIs and band composites from 2017/04/26, 2017/06/05 and 2017/06/15
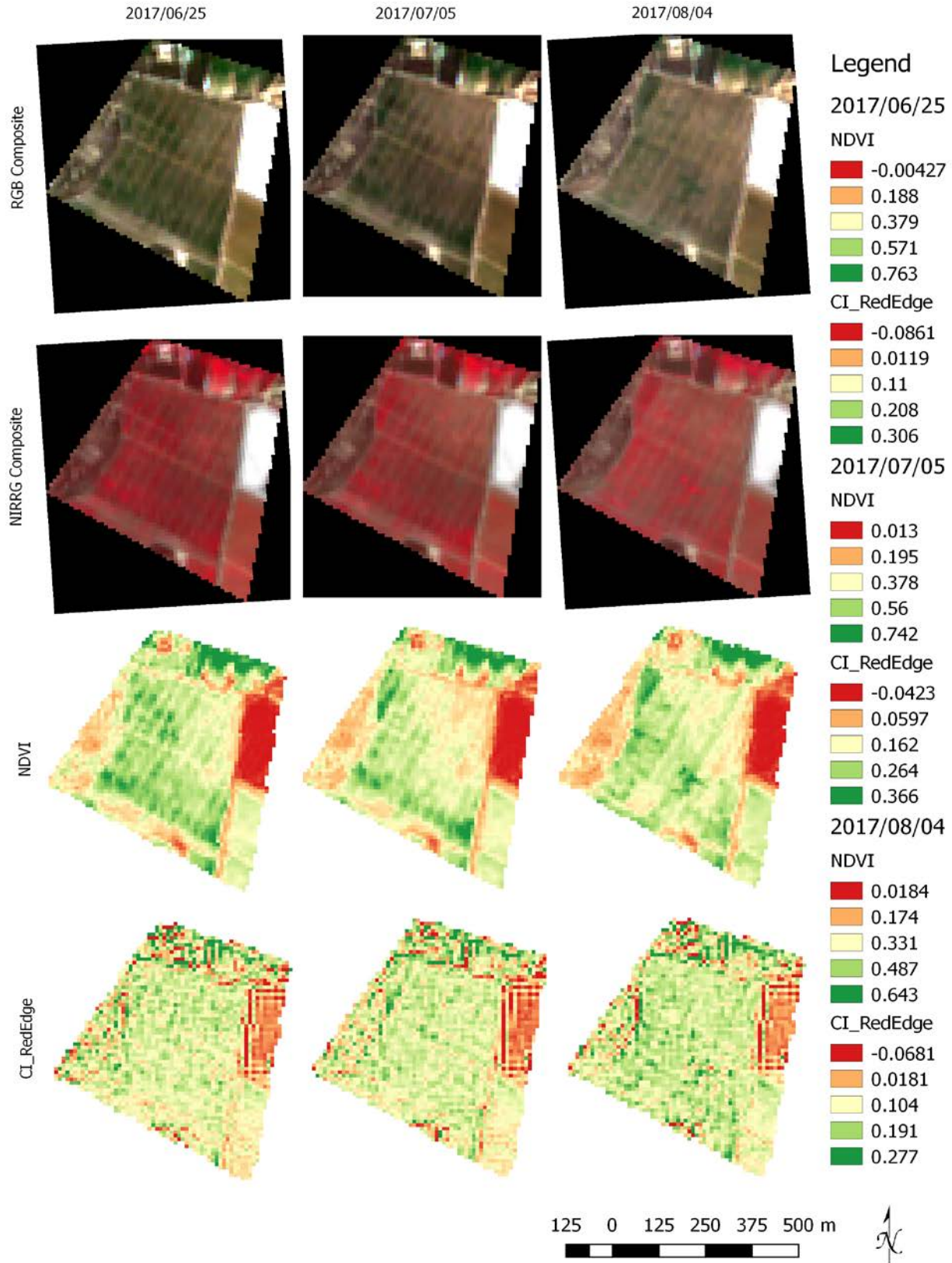
Figure 58: S2 VIs and band composites from 2017/06/25, 2017/07/05 and 2017/08/04

The area monitored through the satellite images is roughly 20ha in total. It is evident that the 10 meter spatial resolution RGB true color composite, NIRRG false color composite and the VIs generated NDVI and CI_RedEdge can indeed provide some insight into the status and the activities within the vineyard under observation, which has an area of ~15ha within the clipped region.

The Red Edge Chlorophyll Index maps that provide the photosynthetic capacity of the vineyard are proven to be the least informative and useful between the satellite products mainly due to the vineyard's state and condition.
Only a vague insight for the photosynthetic ability of the vineyard and the zones can be derived in times of vigorous vegetation in general, including parasitic plants and herbs before the evident ploughing of the area. As a result, the CI_RedEdge VI is found to contain a poor information subset of the NDVI and will not be taken under further consideration in the current interpretation of the Sentinel data.

The Sentinel imagery from 2017/04/26 is in the middle of springtime and just before the beginning of intensive care practices of the vines. In spring, ploughing is a common practice, and usually it is the first time of the year after the final ploughings during mid-winter.

Ploughing is exercised mainly in May, June and July in order to:
- reduce or eliminate the need for herbicides;
- aerate and oxygenate the soil for favorable microorganisms;
- insert surface beneficial features from the natural mulch deeper, thus reducing the need for nitrogen fertilizers which also strengthens the parasitic vegetation;
- allow surface water to reach deeper depths in order to hold reserves;
- cut the lateral roots to encourage the principal roots to go deeper.

As of **2017/04/26** the vineyard was not ploughed and the wild vegetation blooming is evident. This was also the result of recent high temperatures and excessive precipitation as a general meteorological observation in the vicinity of Attica. The intense vegetation and the wild state of the vineyard is clear from the RGB composite, the very high NDVI values and the strong NIR reflectance depicted in the NIRRG false color composite by the dominant Red band which is replaced by the very high reflectance values of the NIR S2 band.
The southeastern vineyard in the borders of the pilot site is also of particular interest as it exhibits only soil reflectance values in all composites and the NDVI. It is assumed that the cultivation practices in this vineyard are much more intense and that ploughing was already done throughout the filed. Higher NDVI values are detected in the mid-eastern vineyard part which indicated mainly soil with some parasitic vegetation after relatively recent ploughing.
Vines are not visible at this resolution as they are mainly comprised of the permanent trunk and the main branches that will support and provide the leaves and fruits of the plant in the following months.

The next image data available from S2 is taken in **2017/06/05**, in the end of spring and the beginning of summer. In this dataset, one month later, it is clear the ploughing and possibly pruning has been

exercised. The vine rows are discriminated and the most vivid area in the center of the southern part of the vineyard as seen in the 2017/04/26 imagery is most taken care of. Higher soil reflectance values with some vegetation is dominant in this area. Due to the ploughing, the average and peak values of the NDVI are lower in general.

For comparison reasons, the partial southeastern vineyard shows some vegetation growth and the mid-eastern one is showing clearly high NDVI values with blooming vines underlying vegetation.

The following S2 image dataset at **2017/06/15**, 10 days later than the previous one, provides some deeper comprehension of the vines condition and the agricultural practices. The previously ploughed part of the main vineyard shows superior vegetation features that are the product of both the initial vines blooming and the herbs below. Ploughing has been conducted in the rest of the vineyard in a more complete way, highlighting the vines rows and discriminating the potential zones for monitoring. However, it has to be mentioned that the vegetation below the vines are not managed at all, an aspect that is made distinct by the eastern vineyards which were recently ploughed and maybe herbicides or some other method was used for the soil management. The mid-eastern vineyard has been ploughed in the 10 past days as clearly shown by the NIRRG composite and the lower homogeneous NDVI values while the southeastern one does not show any visible anthropogenic changes, just a growth in the overall vegetation from crops and herbs.

The following two S2 image datasets with 10 days interval at **2017/06/25** and **2017/07/05** are found to provide some insight in the continuum of the crop status features as the overall growth of the vines is evident and **approaches the very high resolution UAS data from 2017/06/21 and 2017/06/26**.
One can correlate the ploughing activity evident at the UAS data in the southernmost part of the main vineyard, which is visible at the satellite data as well, thus also providing a clue to the S2 depiction of ploughed land for this specific site.
The homogeneity of the eastern bordering vineyards that are shown in the UAS imagery also provides insight for the real difference between S2 depicted vineyards in 10m resolution that are well managed and the pilot vineyard under monitoring which is moderately cultivated. The much higher and denser concentrated NDVI values do indicate the underlying and between vine rows vegetation, which obscure the true vines reflectance. As a result, only vague observations can be made in order to examine the crops health and vigor through NDVI or other VIs.

The final S2 imagery from **2017/08/04** provides some more information. The vineyard has undergone some more ploughing and agronomical activities while the vines in the eastern vineyards seem to be growing due to the higher NDVI values. In the mid-southwestern part of the main vineyard, a selective portion seems to have been very recently ploughed. This is a particular portion of the site that has been deliberately cultivated in a different manner than the rest of the vineyard. It is safe to assume that it is a small testing or practicing site.

Throughout all of the S2 time-series datasets at **2017/04/26, 2017/06/05, 2017/06/15, 2017/06/25 and 2017/07/05 and 2017/08/04** it can be observed that the northeastern part of the main vineyard shares

a common feature; it is underdeveloped and it is possibly under some stress factors. This phenomenon seems to have a time consistent evolution throughout the consecutive S2 images.

Some possible interpretations of this observation are the following either individually or as a combination:

- Artificial irrigation issues;
- Surface water flow issues due to topography as seen in the high resolution DSM and hydrology maps from the UAS;
- Younger vines;
- Less general agronomical attention;
- Pathogenic issues from a developing situation like *Plasmopara viticola* infestation. In 2017, due to heavy precipitation and high temperatures, vineyards in most areas of Greece were infested by this oomycete, which is one on the most lethal grapevine enemies;
- Less or nil nitrogen, potassium or other fertilizers application.

5 Conclusions

The execution of the experiment has been taken under multiple stages. The main purpose in the current context is a showcase, an exhibition, a proof of concept and a preliminary analysis of the remotely sensed results. The multiple different components utilized within the current experiment and pilot vineyard were chosen under specifications for best vegetation and crop monitoring practices in remote sensing and a well-established techniques bundle. However it has to emphasized that as always and even more importantly for vines, ground truth and validation is required by agriculturists, agronomists and in-vitro analyses.

The Precision Viticulture oriented surveys conducted with the UAS equipped with the crop specific multispectral Sequoia sensor array and the radiometric Flir Vue Pro R camera are highly satisfying in quality and richness, while demonstrating the potential of such a systematic monitoring formula.
The very high resolution true and false color composites and the VI orthomaps emphasizing the NDVI and Red Edge Chlorophyll Index VIs have provided the transformations needed to assess the photosynthetic capacity and thus provide measures of stress estimation and possible causes for the vineyard along with the distinction of site-specific features. The radiometric thermal orthomaps additionally provide a very high resolution portrait of the thermal capacities and variabilities in the surveyed area, indicating clearly stressed zones and possible irrigation concerns.

The open Sentinel-2 satellite data also provide sufficient and valuable input to the temporal dimension needed for a complete PV approach. The high spatial, temporal (Sentinel-2 A and B constellation coverage) and radiometric resolutions of the MSI are invaluable tools for agricultural driven EO services and data acquisition.
Utilizing the bands needed for the construction of the same VIs as the UAS derived ones, there was a direct comparison and time consistent evaluation of the vineyard status. However, due to the coarser spatial resolution, only a few useful observations can be made in the magnitude allowed through the 10 meters pixel size.

In general, the frequency of cloud-free data availability, the resolution and the cost are the limiting factors to crop monitoring from space. The Sentinel-2 data can typically provide alerts for possible issues and cannot provide a highly detailed overview. Today, EO commercial non-military satellites can provide continuous global coverage of down to 30cm spatial resolution with multispectral instruments for vegetation monitoring, unfortunately at a relatively high cost. Even this lowest threshold for spatial resolution is the limit for public and commercial use due to the relevant legislation.

In regard to a future perspective, it is well defined and a priority that remotely sensed datasets should be validated and confirmed in a detailed way through ground truth data and near-future observation and measurements.
Combining satellite imagery from Sentinel-2 and UAV mosaics and analysis are the first chain components of a holistic robust procedure that integrates:

- Space-borne: Satellites with multispectral and hyperspectral optical payloads in high and very high resolutions, SAR instruments;
- Airborne: UASs, Aircraft campaigns with vegetation monitoring instrumentation like thermal, multispectral and hyperspectral optical sensors, Radars;
- Ground in-situ measurements:
  - ICT sensor grids for the vineyards
    - local meteorological monitoring: precipitation, temperature, humidity, wind etc.
    - soil characteristics like humidity, salinity and temperature,
    - PAR monitoring etc.;
  - Berry, leaf samples and biochemical analyses;
  - Non-destructive hand held tools for e.g. LAI and chlorophyll content measurements as the in vivo state of the biochemicals may significantly differ from their in vitro state. Isolated biochemicals may be physically altered by isolation processes such as oxidation, hydrolysis or denaturation.
- Citizen observatories, crowdsourcing and generally citizen science and involvement which have been exhibiting a great potential for scientific and practical use by contributing data or massively elaborating on them.
- Information Technology platforms synthesizing the above data streams to automatically extract and transform the useful agronomical knowledge from all the available inputs. Such transformed information could be input to variable rate technology agricultural machines, GNSS enabled farming robots and change the human perspective through decision support systems with direct impact in costs, quantities, qualities and sustainability factors.

Such an agronomical engineering multidisciplinary approach to vineyards cultivation utilizing multiple layers of treasured information, would provide consistent and trustworthy knowledge to science, the farming community, government and other interested parties.

Furthermore, it has to be mentioned that very small sized vineyards provide suitable conditions for very low altitude flights resulting in ultra-high resolution mapping and site-specific management of the utmost detail and variability identification.

Common sense implying that a very small farming activity can be easily inspected in-vivo by experts lack the scientific view that site specific management with remote sensing techniques can predict, optimize and identify factors that may deeply affect the plants and the yield before they can be recognized by agronomists, agriculturists or empiricism. RS techniques however cannot substitute the in situ analysis needed and the well exercised agricultural knowledge, but can supplement them in various ways and provide unique features and analytical tools.

ANNEX 1 – R script for statistics and plotting

```r
# Author: Vlachopoulos Odysseas #
# R script for basic statistics and plots of indice values #
# extracted from the corresponding rasters generated in QGIS #

library(raster)
library(ggplot2)

# BLOCK1: Extract all pixel values from full index raster
# with exact full vector shapefile of vineyard
r <- stack('C:\PilotSite\SEQUOIA_FULL_1\CI_RedEdge.tif')
poly <- shapefile('C:\PilotSite\FullPolygon.shp')
val <- extract(r,poly)
listnames <- poly$full
valList <- list()
for(i in 1:length(val)){
  valList[[i]] <- data.frame(ID=listnames[[i]],Value = val[[i]][,1])
}
write.csv(do.call(rbind.data.frame,valList),"CI_RedEdge.csv")
#END OF BLOCK1

# BLOCK2: Extract all pixel values from inspected areas in index raster
# with vector shapefile of those areas of interest in the vineyard
r <- stack('C:\PilotSite\clipped_CIRedEdge_Polygons.tif')
poly <- shapefile('C:\PilotSite\Polygons.shp')
val <- extract(r,poly)
listnames <- poly$Polygon
valList <- list()
for(i in 1:length(val)){
  valList[[i]] <- data.frame(ID=listnames[[i]],Value = val[[i]][,1])
}
write.csv(do.call(rbind.data.frame,valList),"CIRedEdge_Polygons.csv")
#END OF BLOCK2

# BLOCK3: Make histogram and density plots of the whole index map
df = read.csv('C:/PilotSite/CSVs/NDVI.csv')
range <- seq(-1,6,0.1)
d <- density(df[,'Value']) # returns the density data
jpeg('NDVI_density.jpg')
plot(d, main="Density: NDVI", xlab="NDVI") # plots the results
dev.off()
jpeg('NDVI_hist.jpg')
hist(df[,'Value'], breaks=range, col="#CCCCFF", main="Frequency: NDVI",
xlab="NDVI")
# Histogram properties: light blue #CCCCFF, Use "range" number of bins
dev.off()
# END OF BLOCK3

# BLOCK4: Index histograms and densities after polygon mask and value
extraction for each polygon
df2 = read.csv('C:/PilotSite/CSVs/NDVI_Polygons.csv')

# Factorize and extra column for ggplot purposes
```

```r
df2$ID <- factor(df2$ID)
df$dfid <- 'NDVI'
df2$dfid <- 'NDVI_Polygons'

# Co-plot full index map statistics with full polygons statistics
jpeg('NDVI_both_withAllPolygons.jpg')
both <- rbind(df, df2)
ggplot(both, aes(x=Value, fill = dfid)) + geom_density(alpha = 0.2) +
ggtitle("NDVI vs Total Polygons")
dev.off()

# Co-plot full index map statistics with each polygon statistics
for (i in 1:10){
  subsetPoly <- subset(df2, df2$ID==i)
  forjpeg <- paste("NDVI_Polygon", as.character(i), "_density.jpeg", sep="")
  forgg <- paste("NDVI vs Polygon", as.character(i), sep="")
  jpeg(forjpeg)
  both <- rbind(df, subsetPoly)
  pl <- ggplot(both, aes(x=Value, fill = dfid)) + geom_density(alpha = 0.2)+
ggtitle(forgg)
  print(pl)
  dev.off()

  d1 <- density(subsetPoly$Value) # returns the density data
  title <- paste("Density: Polygon", as.character(i), sep="")
  subtitle <- paste("Polygon", as.character(i), sep="")
  forjpeg <- paste(subtitle, "_NDVI_density.jpeg", sep="")
  jpeg(forjpeg)
  plot(d1, main=title, xlab=subtitle) # plots the results
  dev.off()
  range <- seq(-1,1,0.1)
  title2 <- paste("Frequency: Polygon", as.character(i), sep="")
  forjpeg2 <- paste(subtitle, "_NDVI_histogram.jpeg", sep="")
  jpeg(forjpeg2)
  hist(subsetPoly$Value, breaks=range, col="#CCCCFF", main=title2,
xlab=subtitle)
  dev.off()

  }
# END OF BLOCK4
```

ANNEX 2 – Python script for raster clipping and generation

```python
# Author: Vlachopoulos Odysseas #
# Python script for raster clipping by polygon and new raster generation #

import os
from osgeo import gdal, ogr

def ClipRasterWithPolygon(rasterPath, polyPath, outPath):
    os.system("gdalwarp -dstnodata -0 -q -cutline " + polyPath + " -
crop_to_cutline " + " -of GTiff " + rasterPath + " " + outPath)

def CreateClippingPolygons(inPath, rast, field):
    driverSHP = ogr.GetDriverByName("ESRI Shapefile")
    ds = driverSHP.Open(inPath)
    if ds is None:
        print 'Layer not open'
    lyr = ds.GetLayer()
    spatialRef = lyr.GetSpatialRef()

    for feature in lyr:
        fieldVal = feature.GetField(field)
        os.mkdir("C:/PilotSite/ClippingFeatures" + rast.split("_",2)[1] + "/"
+ str(fieldVal))
        outds = driverSHP.CreateDataSource("C:/PilotSite/ClippingFeatures" +
rast.split("_",2)[1]  + "/" + str(fieldVal) + "/clip.shp")
        outlyr = outds.CreateLayer(str(fieldVal) + "/clip.shp",
srs=spatialRef, geom_type=ogr.wkbPolygon)
        outDfn = outlyr.GetLayerDefn()
        ingeom = feature.GetGeometryRef()
        outFeat = ogr.Feature(outDfn)
        outFeat.SetGeometry(ingeom)
        outlyr.CreateFeature(outFeat)

def ClipRasters(inPath, rast, field):
    driverSHP = ogr.GetDriverByName("ESRI Shapefile")
    ds = driverSHP.Open(inPath)
    if ds is None:
        print 'Layer not open'
    lyr = ds.GetLayer()
    for feature in lyr:
        fieldVal = feature.GetField(field)
        ClipRasterWithPolygon(rast, "C:/PilotSite/ClippingFeatures"+
rast.split("_",2)[1] + "/" +str(fieldVal), "C:/PilotSite/ClippingFeatures"+
rast.split("_",2)[1] + "/" +str(fieldVal)+"/"+rast.split("_",2)[1]
+str(fieldVal)+"out.tif")

#Run
rasters = ["" for x in range(6)]
rasters[0] = "C:/PilotSite/Full_RGB_Polygons.tif"
rasters[1] = "C:/PilotSite/Full_NIRRG_Polygons.tif"
rasters[2] = "C:/PilotSite/Full_NDVI_Polygons.tif"
rasters[3] = "C:/PilotSite/Full_CIRedEdge_Polygons.tif"
rasters[4] = "C:/PilotSite/Full_FlirSRGB_Polygons.tif"
```

```python
rasters[5] = "C:/PilotSite/Full_FlirTIF_Polygons.tif"
for raster in rasters:
    os.mkdir("C:/PilotSite/ClippingFeatures"+raster.split("_",2)[1] )
    poly = "C:/PilotSite/Polygons.shp"
    CreateClippingPolygons(poly, raster, "Polygons")
    ClipRasters(poly, raster, "Polygons")
```

ANNEX 3 – Sentinel 2 datasets

Image ID	S2A_MSIL2A_20170426T091031_N0204_R050_T34SGH_20170426T091828.SAFE
Product Level	Level 2A
Product Type	S2MSI2Ap
Collection Date	2017/04/26
Ellipsoid Type/Projection	WGS-84/UTM, N34
Format	JPEG 2000
Bits/Pixel	12

Image ID	S2A_MSIL2A_20170605T091031_N0205_R050_T34SGH_20170605T091810.SAFE
Product Level	Level 2A
Product Type	S2MSI2Ap
Collection Date	2017/06/05
Ellipsoid Type/Projection	WGS-84/UTM, N34
Format	JPEG 2000
Bits/Pixel	12

Image ID	S2A_MSIL2A_20170615T090551_N0205_R050_T35SKC_20170615T091937.SAFE
Product Level	Level 2A
Product Type	S2MSI2Ap
Collection Date	2017/06/15
Ellipsoid Type/Projection	WGS-84/UTM, N35
Format	JPEG 2000
Bits/Pixel	12

Image ID	S2A_MSIL2A_20170625T091021_N0205_R050_T35SKC_20170625T091829.SAFE
Product Level	Level 2A
Product Type	S2MSI2Ap
Collection Date	2017/06/25
Ellipsoid Type/Projection	WGS-84/UTM, N35
Format	JPEG 2000
Bits/Pixel	12

Image ID	S2A_MSIL2A_20170705T090551_N0205_R050_T34SGH_20170705T090814.SAFE
Product Level	Level 2A
Product Type	S2MSI2Ap
Collection Date	2017/07/05
Ellipsoid Type/Projection	WGS-84/UTM, N34
Format	JPEG 2000
Bits/Pixel	12

Image ID	S2A_MSIL2A_20170804T091031_N0205_R050_T35SKC_20170804T091836.SAFE
Product Level	Level 2A
Product Type	S2MSI2Ap
Collection Date	2017/08/04
Ellipsoid Type/Projection	WGS-84/UTM, N35
Format	JPEG 2000
Bits/Pixel	12

References

Antropov, O., Rauste, Y., Hame, T., 2011. Volume Scattering Modeling in PolSAR Decompositions: Study of ALOS PALSAR Data Over Boreal Forest. IEEE Transactions on Geoscience and Remote Sensing 49, 3838–3848. doi:10.1109/TGRS.2011.2138146

Arii, M., van Zyl, J.J., Kim, Y., 2011. Adaptive Model-Based Decomposition of Polarimetric SAR Covariance Matrices. IEEE Transactions on Geoscience and Remote Sensing 49, 1104–1113. doi:10.1109/TGRS.2010.2076285

Arii, M., van Zyl, J.J., Kim, Y., 2010. A General Characterization for Polarimetric Scattering From Vegetation Canopies. IEEE Transactions on Geoscience and Remote Sensing 48, 3349–3357. doi:10.1109/TGRS.2010.2046331

Arno, J., Mart?nez Casasnovas, J.A., Ribes Dasi, M., Rosell, J.R., 2009. Review. Precision viticulture. Research topics, challenges and opportunities in site-specific vineyard management. Spanish Journal of Agricultural Research 7, 779. doi:10.5424/sjar/2009074-1092

Ballester-Berman, J.D., Lopez-Sanchez, J.M., 2010. Applying the Freeman–Durden Decomposition Concept to Polarimetric SAR Interferometry. IEEE Transactions on Geoscience and Remote Sensing 48, 466–479. doi:10.1109/TGRS.2009.2024304

Ballester-Berman, J.D., Vicente-Guijalba, F., Lopez-Sanchez, J.M., 2013. POLARIMETRIC SAR MODEL FOR SOIL MOISTURE ESTIMATION OVER VINEYARDS AT C-BAND. Progress In Electromagnetics Research 142, 639–665. doi:10.2528/PIER13071702

Bannari, A., Morin, D., Bonn, F., Huete, A.R., 1995. A review of vegetation indices. Remote Sensing Reviews 13, 95–120. doi:10.1080/02757259509532298

Barnes, E.M., Clarke, T.R., Richards, S.E., Colaizzi, P.D., Haberland, J., Kostrzewski, M., Waller, P., Choi, C., Riley, E., Thompson, T., others, 2000. Coincident detection of crop water stress, nitrogen status and canopy density using ground based multispectral data, in: Proceedings of the Fifth International Conference on Precision Agriculture, Bloomington, MN, USA.

Baup, F., Villa, L., Fieuzal, R., Ameline, M., 2016. Sensitivity of X-Band (σ0, γ) and Optical (NDVI) Satellite Data to Corn Biophysical Parameters. Advances in Remote Sensing 5, 103.

Bioucas-Dias, J.M., Plaza, A., Dobigeon, N., Parente, M., Du, Q., Gader, P., Chanussot, J., 2012. Hyperspectral unmixing overview: Geometrical, statistical, and sparse regression-based approaches. IEEE journal of selected topics in applied earth observations and remote sensing 5, 354–379.

Borengasser, M., Hungate, W.S., Watkins, R., 2007. Hyperspectral remote sensing: principles and applications. Crc Press.

Bramley, R.G.V., 2005. Understanding variability in winegrape production systems 2. Within vineyard variation in quality over several vintages. Australian Journal of Grape and Wine Research 11, 33–42. doi:10.1111/j.1755-0238.2005.tb00277.x

Broge, N.H., Leblanc, E., 2001. Comparing prediction power and stability of broadband and hyperspectral vegetation indices for estimation of green leaf area index and canopy chlorophyll density. Remote sensing of environment 76, 156–172.

Burini, A., Schiavon, G., Solimini, D., 2008. Fusion of high resolution polarimetric SAR and multi-spectral optical data for precision viticulure, in: Geoscience and Remote Sensing Symposium, 2008. IGARSS 2008. IEEE International. IEEE, p. III–1000.

Buschmann, C., Nagel, E., 1993. In vivo spectroscopy and internal optics of leaves as basis for remote sensing of vegetation. International Journal of Remote Sensing 14, 711–722.

Campos-Taberner, M., García-Haro, F., Camps-Valls, G., Grau-Muedra, G., Nutini, F., Busetto, L., Katsantonis, D., Stavrakoudis, D., Minakou, C., Gatti, L., Barbieri, M., Holecz, F., Stroppiana, D., Boschetti, M., 2017. Exploitation of SAR and Optical Sentinel Data to Detect Rice Crop and Estimate Seasonal Dynamics of Leaf Area Index. Remote Sensing 9, 248. doi:10.3390/rs9030248

Camps-Valls, G., Bruzzone, L., 2009. Kernel methods for remote sensing data analysis. John Wiley & Sons.

Chang, C.-I., 2013. Hyperspectral data processing: algorithm design and analysis. John Wiley & Sons.

Charbonneau, F.J., Brisco, B., Raney, R.K., McNairn, H., Liu, C., Vachon, P.W., Shang, J., DeAbreu, R., Champagne, C., Merzouki, A., others, 2010. Compact polarimetry overview and applications assessment. Canadian Journal of Remote Sensing 36, S298–S315.

Chen, C., 2015. Determining the Leaf Emissivity of Three Crops by Infrared Thermometry. Sensors 15, 11387–11401.

Choe, E., van der Meer, F., van Ruitenbeek, F., van der Werff, H., de Smeth, B., Kim, K.-W., 2008. Mapping of heavy metal pollution in stream sediments using combined geochemistry, field spectroscopy, and hyperspectral remote sensing: A case study of the Rodalquilar mining area, SE Spain. Remote Sensing of Environment 112, 3222–3233.

Clevers, J.G.P.W., Gitelson, A.A., 2013. Remote estimation of crop and grass chlorophyll and nitrogen content using red-edge bands on Sentinel-2 and -3. International Journal of Applied Earth Observation and Geoinformation 23, 344–351. doi:10.1016/j.jag.2012.10.008

Cloude, R., Papathanassiou, K.P., 1999. Surface roughness and polarimetric entropy, in: Geoscience and Remote Sensing Symposium, 1999. IGARSS'99 Proceedings. IEEE 1999 International. IEEE, pp. 2443–2445.

Cloude, S., 2009. Polarisation: Applications in Remote Sensing. Oxford University Press. doi:10.1093/acprof:oso/9780199569731.001.0001

Cloude, S.R., Pottier, E., 1997. An entropy based classification scheme for land applications of polarimetric SAR. IEEE Transactions on Geoscience and Remote Sensing 35, 68–78. doi:10.1109/36.551935

Coombe, B.G., Dry, P.R., 2004. Grapevine growth stages-The modified EL system. Viticulture 152–153.

Costa-Cabral, M.C., Burges, S.J., 1994. Digital elevation model networks (DEMON): A model of flow over hillslopes for computation of contributing and dispersal areas. Water resources research 30, 1681–1692.

Courty, N., Aptoula, E., Lefèvre, S., 2012. A classwise supervised ordering approach for morphology based hyperspectral image classification, in: Pattern Recognition (ICPR), 2012 21st International Conference On. IEEE, pp. 1997–2000.

Dalal, R.C., Henry, R.J., 1986. Simultaneous determination of moisture, organic carbon, and total nitrogen by near infrared reflectance spectrophotometry. Soil Science Society of America Journal 50, 120–123.

Dash, P., Gottsche, F.-M., Olesen, F.-S., Fischer, H., 2002. Land surface temperature and emissivity estimation from passive sensor data: Theory and practice-current trends. International Journal of Remote Sensing 23, 2563–2594. doi:10.1080/01431160110115041

Datt, B., McVicar, T.R., Van Niel, T.G., Jupp, D.L., Pearlman, J.S., 2003. Preprocessing EO-1 Hyperion hyperspectral data to support the application of agricultural indexes. IEEE Transactions on Geoscience and Remote Sensing 41, 1246–1259.

David Ballester-Berman, J., Garmendia-Lopez, I., Lopez-Sanchez, J.M., Mangas-Martin, V.J., 2012. Analysis of the polarimetric response of vineyards at C-band. Canadian Journal of Remote Sensing 38, 223–239. doi:10.5589/m12-016

Delegido, J., Verrelst, J., Alonso, L., Moreno, J., 2011. Evaluation of Sentinel-2 Red-Edge Bands for Empirical Estimation of Green LAI and Chlorophyll Content. Sensors (Basel) 11, 7063–7081. doi:10.3390/s110707063

Dubois, P.C., van Zyl, J., Engman, T., 1995. Measuring soil moisture with imaging radars. IEEE Transactions on Geoscience and Remote Sensing 33, 915–926. doi:10.1109/36.406677

Fairfield, J., Leymarie, P., 1991. Drainage networks from grid digital elevation models. Water resources research 27, 709–717.

Fauvel, M., Tarabalka, Y., Benediktsson, J.A., Chanussot, J., Tilton, J.C., 2013. Advances in spectral-spatial classification of hyperspectral images. Proceedings of the IEEE 101, 652–675.

Feng Xu, Ya-Qiu Jin, 2005. Deorientation theory of polarimetric scattering targets and application to terrain surface classification. IEEE Transactions on Geoscience and Remote Sensing 43, 2351–2364. doi:10.1109/TGRS.2005.855064

Filella, I., Serrano, L., Serra, J., Penuelas, J., 1995. Evaluating wheat nitrogen status with canopy reflectance indices and discriminant analysis. Crop Science 35, 1400–1405.

Fisette, T., Rollin, P., Aly, Z., Campbell, L., Daneshfar, B., Filyer, P., Smith, A., Davidson, A., Shang, J., Jarvis, I., 2013. AAFC annual crop inventory, in: Agro-Geoinformatics (Agro-Geoinformatics), 2013 Second International Conference On. IEEE, pp. 270–274.

Franke, J., Menz, G., 2007. Multi-temporal wheat disease detection by multi-spectral remote sensing. Precision Agriculture 8, 161–172.

Freeman, A., 2007. Fitting a Two-Component Scattering Model to Polarimetric SAR Data From Forests. IEEE Transactions on Geoscience and Remote Sensing 45, 2583–2592. doi:10.1109/TGRS.2007.897929

Freeman, A., Durden, S.L., 1998. A three-component scattering model for polarimetric SAR data. IEEE Transactions on Geoscience and Remote Sensing 36, 963–973. doi:10.1109/36.673687

French, A.., Schmugge, T.., Kustas, W.., 2000. Discrimination of Senescent Vegetation Using Thermal Emissivity Contrast. Remote Sensing of Environment 74, 249–254. doi:10.1016/S0034-4257(00)00115-2

Fuchs, M., Tanner, C.B., 1966. Infrared thermometry of vegetation. Agronomy Journal 58, 597–601.

Garbrecht, J., Martz, L.W., 1997. The assignment of drainage direction over flat surfaces in raster digital elevation models. Journal of hydrology 193, 204–213.

Gaussorgues, G., Chomet, S., 2012. Infrared thermography. Springer Science & Business Media.

Gherboudj, I., Magagi, R., Berg, A.A., Toth, B., 2011. Soil moisture retrieval over agricultural fields from multi-polarized and multi-angular RADARSAT-2 SAR data. Remote Sensing of Environment 115, 33–43. doi:10.1016/j.rse.2010.07.011

Ghosh, A., Subudhi, B.N., Bruzzone, L., 2013. Integration of Gibbs Markov random field and Hopfield-type neural networks for unsupervised change detection in remotely sensed multitemporal images. IEEE Transactions on Image Processing 22, 3087–3096.

Gitelson, A.A., Kaufman, Y.J., Merzlyak, M.N., 1996. Use of a green channel in remote sensing of global vegetation from EOS-MODIS. Remote sensing of Environment 58, 289–298.

Gitelson, A.A., Kaufman, Y.J., Stark, R., Rundquist, D., 2002. Novel algorithms for remote estimation of vegetation fraction. Remote sensing of Environment 80, 76–87.

Gitelson, A.A., Merzlyak, M.N., 1997. Remote estimation of chlorophyll content in higher plant leaves. International Journal of Remote Sensing 18, 2691–2697. doi:10.1080/014311697217558

Gitelson, A.A., Vina, A., Ciganda, V., Rundquist, D.C., Arkebauer, T.J., 2005. Remote estimation of canopy chlorophyll content in crops. Geophysical Research Letters 32.

Gomez, C., Rossel, R.A.V., McBratney, A.B., 2008. Soil organic carbon prediction by hyperspectral remote sensing and field vis-NIR spectroscopy: An Australian case study. Geoderma 146, 403–411.

Guanter, L., Alonso, L., Moreno, J., 2005. First results from the PROBA/CHRIS hyperspectral/multiangular satellite system over land and water targets. IEEE Geoscience and Remote Sensing Letters 2, 250–254.

Gudesblat, G.E., Torres, P.S., Vojnov, A.A., 2009. Stomata and pathogens. Plant Signal Behav 4, 1114–1116.

Guoquan, D., Zhengzhi, L., 1993. The apparent emissivity of vegetation canopies. International journal of remote sensing 14, 183–188.

Haboudane, D., Miller, J.R., Pattey, E., Zarco-Tejada, P.J., Strachan, I.B., 2004. Hyperspectral vegetation indices and novel algorithms for predicting green LAI of crop canopies: Modeling and validation in the context of precision agriculture. Remote sensing of environment 90, 337–352.

Haboudane, D., Miller, J.R., Tremblay, N., Zarco-Tejada, P.J., Dextraze, L., 2002. Integrated narrow-band vegetation indices for prediction of crop chlorophyll content for application to precision agriculture. Remote Sensing of Environment 81, 416–426. doi:10.1016/S0034-4257(02)00018-4

Hajnsek, I., Jagdhuber, T., Schon, H., Papathanassiou, K.P., 2009. Potential of Estimating Soil Moisture Under Vegetation Cover by Means of PolSAR. IEEE Transactions on Geoscience and Remote Sensing 47, 442–454. doi:10.1109/TGRS.2008.2009642

Hajnsek, I., Pottier, E., Cloude, S.R., 2003. Inversion of surface parameters from polarimetric SAR. IEEE Transactions on Geoscience and Remote Sensing 41, 727–744. doi:10.1109/TGRS.2003.810702

Hall, A., Lamb, D.W., Holzapfel, B., Louis, J., 2002. Optical remote sensing applications in viticulture - a review. Australian Journal of Grape and Wine Research 8, 36–47. doi:10.1111/j.1755-0238.2002.tb00209.x

Hansen, P.M., Schjoerring, J.K., 2003. Reflectance measurement of canopy biomass and nitrogen status in wheat crops using normalized difference vegetation indices and partial least squares regression. Remote sensing of environment 86, 542–553.

Harris, R., Baumann, I., 2015. Open data policies and satellite Earth observation. Space Policy 32, 44–53. doi:10.1016/j.spacepol.2015.01.001

Hoffer, M.R., n.d. Biological and physical considerations in applying computer-aided analysis techniques to remote sensing. [WWW Document]. ResearchGate. URL https://www.researchgate.net/publication/279554586_Biological_and_physical_considerations_in_applying_computer-aided_analysis_techniques_to_remote_sensing (accessed 6.28.17).

Hu, W., Huang, Y., Wei, L., Zhang, F., Li, H., 2015. Deep convolutional neural networks for hyperspectral image classification. Journal of Sensors 2015.

Huete, A.., 1988. A soil-adjusted vegetation index (SAVI). Remote Sensing of Environment 25, 295–309. doi:10.1016/0034-4257(88)90106-X

Huete, A., Didan, K., Miura, T., Rodriguez, E.., Gao, X., Ferreira, L.., 2002. Overview of the radiometric and biophysical performance of the MODIS vegetation indices. Remote Sensing of Environment 83, 195–213. doi:10.1016/S0034-4257(02)00096-2

Huete, A.R., Post, D.F., Jackson, R.D., 1984. Soil spectral effects on 4-space vegetation discrimination. Remote sensing of environment 15, 155–165.

Hunt, E.R., Daughtry, C.S.T., Eitel, J.U., Long, D.S., 2011. Remote sensing leaf chlorophyll content using a visible band index. Agronomy journal 103, 1090–1099.

Iordache, M.-D., Bioucas-Dias, J.M., Plaza, A., 2012. Total variation spatial regularization for sparse hyperspectral unmixing. IEEE Transactions on Geoscience and Remote Sensing 50, 4484–4502.

Jagdhuber, T., Hajnsek, I., Bronstert, A., Papathanassiou, K.P., 2013. Soil Moisture Estimation Under Low Vegetation Cover Using a Multi-Angular Polarimetric Decomposition. IEEE Transactions on Geoscience and Remote Sensing 51, 2201–2215. doi:10.1109/TGRS.2012.2209433

Jong-Sen Lee, Schuler, D.L., Ainsworth, T.L., 2000. Polarimetric SAR data compensation for terrain azimuth slope variation. IEEE Transactions on Geoscience and Remote Sensing 38, 2153–2163. doi:10.1109/36.868874

Kalouptsidis, N., Koutroumbas, K., Psaraki, V., 2007. Classification methods for random utility models with iid disturbances under the most probable alternative rule. European journal of operational research 176, 1778–1794.

Kauth, R.J., Thomas, G.S., 1976. The tasselled cap–a graphic description of the spectral-temporal development of agricultural crops as seen by Landsat, in: LARS Symposia. p. 159.

Kriegler, F.J., Malila, W.A., Nalepka, R.F., Richardson, W., 1969. Preprocessing transformations and their effects on multispectral recognition, in: Remote Sensing of Environment, VI. p. 97.

Kropff, M.J., Wallinga, J., Lotz, L.A.P., 2007. Modelling for Precision Weed Management, in: Lake, J.V., Bock, G.R., Goode, J.A. (Eds.), Novartis Foundation Symposia. John Wiley & Sons, Ltd., Chichester, UK, pp. 182–207. doi:10.1002/9780470515419.ch12

Küng, O., Strecha, C., Beyeler, A., Zufferey, J.-C., Floreano, D., Fua, P., Gervaix, F., 2011. The accuracy of automatic photogrammetric techniques on ultra-light UAV imagery, in: UAV-g 2011-Unmanned Aerial Vehicle in Geomatics.

Labus, M.P., Nielsen, G.A., Lawrence, R.L., Engel, R., Long, D.S., 2002. Wheat yield estimates using multi-temporal NDVI satellite imagery. International Journal of Remote Sensing 23, 4169–4180. doi:10.1080/01431160110107653

Lamb, D.W., 2000. The use of qualitative airborne multispectral imaging for managing agricultural crops - a case study in south-eastern Australia. Australian Journal of Experimental Agriculture 40, 725. doi:10.1071/EA99086

Lamb, D.W., Schneider, D.A., Trotter, M.G., Schaefer, M.T., Yule, I.J., 2011. Extended-altitude, aerial mapping of crop NDVI using an active optical sensor: A case study using a Raptor sensor over wheat. Computers and Electronics in Agriculture 77, 69–73. doi:10.1016/j.compag.2011.03.009

Landgrebe, D., 1999. Information extraction principles and methods for multispectral and hyperspectral image data. Information processing for remote sensing 82, 3–38.

Lantzanakis, G., Mitraka, Z., Chrysoulakis, N., 2017. Comparison of Physically and Image Based Atmospheric Correction Methods for Sentinel-2 Satellite Imagery, in: Karacostas, T., Bais, A., Nastos, P.T. (Eds.), Perspectives on Atmospheric Sciences. Springer International Publishing, Cham, pp. 255–261. doi:10.1007/978-3-319-35095-0_36

Lee, J.-S., Ainsworth, T.L., 2011. The Effect of Orientation Angle Compensation on Coherency Matrix and Polarimetric Target Decompositions. IEEE Transactions on Geoscience and Remote Sensing 49, 53–64. doi:10.1109/TGRS.2010.2048333

Lee, J.-S., Ainsworth, T.L., Wang, Y., 2014. Generalized Polarimetric Model-Based Decompositions Using Incoherent Scattering Models. IEEE Transactions on Geoscience and Remote Sensing 52, 2474–2491. doi:10.1109/TGRS.2013.2262051

Li, J., Bioucas-Dias, J.M., Plaza, A., 2012. Spectral–spatial hyperspectral image segmentation using subspace multinomial logistic regression and Markov random fields. IEEE Transactions on Geoscience and Remote Sensing 50, 809–823.

Li, Z., Zhu, C., Gold, C., 2004. Digital terrain modeling: principles and methodology. CRC press.

Liaghat, S., Balasundram, S.K., 2010. A Review: The Role of Remote Sensing in Precision Agriculture. American Journal of Agricultural and Biological Sciences 5, 50–55. doi:10.3844/ajabssp.2010.50.55

Liang, D., Xu, P., Tsang, L., Gui, Z., Chen, K.-S., 2009. ELECTROMAGNETIC SCATTERING BY ROUGH SURFACES WITH LARGE HEIGHTS AND SLOPES WITH APPLICATIONS TO MICROWAVE REMOTE SENSING OF ROUGH

SURFACE OVER LAYERED MEDIA. Progress In Electromagnetics Research 95, 199–218. doi:10.2528/PIER09071413

Lillesand, T., Kiefer, R.W., Chipman, J., 2014. Remote sensing and image interpretation. John Wiley & Sons.

Loew, A., Ludwig, R., Mauser, W., 2006. Derivation of surface soil moisture from ENVISAT ASAR wide swath and image mode data in agricultural areas. IEEE Transactions on Geoscience and Remote Sensing 44, 889–899. doi:10.1109/TGRS.2005.863858

Lopez-Sanchez, J.M., Cloude, S.R., Ballester-Berman, J.D., 2012. Rice Phenology Monitoring by Means of SAR Polarimetry at X-Band. IEEE Transactions on Geoscience and Remote Sensing 50, 2695–2709. doi:10.1109/TGRS.2011.2176740

Loussert, P., Baup, F., Corgne, S., Quénol, H., Ortega, A., 2016. Analysis of SAR and optical temporal signatures of grapevine over a heterogeneous vineyard landscape, in: Neale, C.M.U., Maltese, A. (Eds.), . p. 999805. doi:10.1117/12.2241755

Lyon, J.G., Yuan, D., Lunetta, R.S., Elvidge, C.D., 1998. A change detection experiment using vegetation indices. Photogrammetric engineering and remote sensing 64, 143–150.

Maas, H.-G., Kersten, T., 1997. Aerotriangulation and DEM/orthophoto generation from high-resolution still-video imagery. Photogrammetric Engineering and Remote Sensing 63, 1079–1084.

Maidment, D.R., Djokic, D., 2000. Hydrologic and hydraulic modeling support: with geographic information systems. ESRI, Inc.

Mansaray, L., Huang, W., Zhang, D., Huang, J., Li, J., 2017. Mapping Rice Fields in Urban Shanghai, Southeast China, Using Sentinel-1A and Landsat 8 Datasets. Remote Sensing 9, 257. doi:10.3390/rs9030257

Matteoli, S., Diani, M., Theiler, J., 2014. An overview of background modeling for detection of targets and anomalies in hyperspectral remotely sensed imagery. IEEE Journal of Selected Topics in Applied Earth Observations and Remote Sensing 7, 2317–2336.

Mattia, F., Le Toan, T., Souyris, J.-C., De Carolis, C., Floury, N., Posa, F., Pasquariello, N.G., 1997. The effect of surface roughness on multifrequency polarimetric SAR data. IEEE Transactions on Geoscience and Remote Sensing 35, 954–966. doi:10.1109/36.602537

Mayer, B., Kylling, A., 2005. Technical note: The libRadtran software package for radiative transfer calculations - description and examples of use. Atmospheric Chemistry and Physics 5, 1855–1877. doi:10.5194/acp-5-1855-2005

McCloy, K., 2005. Resource Management Information Systems: Remote Sensing, GIS and Modelling, Second Edition. CRC Press. doi:10.1201/b17305

McNairn, H., Kross, A., Lapen, D., Caves, R., Shang, J., 2014. Early season monitoring of corn and soybeans with TerraSAR-X and RADARSAT-2. International Journal of Applied Earth Observation and Geoinformation 28, 252–259.

McNairn, H., Shang, J., 2016. A Review of Multitemporal Synthetic Aperture Radar (SAR) for Crop Monitoring, in: Multitemporal Remote Sensing. Springer, pp. 317–340.

McNairn, H., Shang, J., Jiao, X., Champagne, C., 2009. The contribution of ALOS PALSAR multipolarization and polarimetric data to crop classification. IEEE Transactions on Geoscience and Remote Sensing 47, 3981–3992.

Melotto, M., Underwood, W., He, S.Y., 2008. Role of Stomata in Plant Innate Immunity and Foliar Bacterial Diseases. Annu Rev Phytopathol 46, 101–122. doi:10.1146/annurev.phyto.121107.104959

Merzouki, A., McNairn, H., Pacheco, A., 2010. Evaluation of the Dubois, Oh, and IEM radar backscatter models over agricultural fields using C-band RADARSAT-2 SAR image data. Canadian Journal of Remote Sensing 36, S274–S286.

Miao, Y., Mulla, D.J., Randall, G.W., Vetsch, J.A., Vintila, R., 2009. Combining chlorophyll meter readings and high spatial resolution remote sensing images for in-season site-specific nitrogen management of corn. Precision Agriculture 10, 45–62. doi:10.1007/s11119-008-9091-z

Modest, M.F., 2013. Radiative heat transfer. Academic press.

Moran, M., 1997. Combining multifrequency microwave and optical data for crop management. Remote Sensing of Environment 61, 96–109. doi:10.1016/S0034-4257(96)00243-X

Nasrabadi, N.M., 2014. Hyperspectral target detection: An overview of current and future challenges. IEEE Signal Processing Magazine 31, 34–44.

Oh, Y., Sarabandi, K., Ulaby, F.T., 1992. An empirical model and an inversion technique for radar scattering from bare soil surfaces. IEEE Transactions on Geoscience and Remote Sensing 30, 370–381. doi:10.1109/36.134086

Papoutsis, I., Kontoes, C., Paradissis, D., 2017. Multi-Stack Persistent Scatterer Interferometry Analysis in Wider Athens, Greece. Remote Sensing 9, 276. doi:10.3390/rs9030276

Peña-Barragán, J.M., Ngugi, M.K., Plant, R.E., Six, J., 2011. Object-based crop identification using multiple vegetation indices, textural features and crop phenology. Remote Sensing of Environment 115, 1301–1316.

Pettorelli, N., Vik, J.O., Mysterud, A., Gaillard, J.-M., Tucker, C.J., Stenseth, N.C., 2005. Using the satellite-derived NDVI to assess ecological responses to environmental change. Trends in Ecology & Evolution 20, 503–510. doi:10.1016/j.tree.2005.05.011

Poni, S., Intrieri, C., Silvestroni, O., 1994. Interactions of leaf age, fruiting, and exogenous cytokinins in Sangiovese grapevines under non-irrigated conditions. I. Gas exchange. American Journal of Enology and Viticulture 45, 71–78.

Prasad, R., Kumar, R., Singh, D., 2009. A RADIAL BASIS FUNCTION APPROACH TO RETRIEVE SOIL MOISTURE AND CROP VARIABLES FROM X-BAND SCATTEROMETER OBSERVATIONS. Progress In Electromagnetics Research B 12, 201–217. doi:10.2528/PIERB08120703

Pratola, C., Del Frate, F., Schiavon, G., Solimini, D., 2013. Toward fully automatic detection of changes in suburban areas from VHR SAR images by combining multiple neural-network models. IEEE Transactions on Geoscience and Remote Sensing 51, 2055–2066.

Price, J., Bausch, W.C., 1995. Leaf area index estimation from visible and near-infrared reflectance data. Remote Sensing of Environment 52, 55–65. doi:10.1016/0034-4257(94)00111-Y

Rao, N.R., 2008. Development of a crop-specific spectral library and discrimination of various agricultural crop varieties using hyperspectral imagery. International Journal of Remote Sensing 29, 131–144.

Rao, N.R., Garg, P.K., Ghosh, S.K., 2007. Development of an agricultural crops spectral library and classification of crops at cultivar level using hyperspectral data. Precision Agriculture 8, 173–185.

Rao, N.R., Garg, P.K., Ghosh, S.K., Dadhwal, V.K., 2008. Estimation of leaf total chlorophyll and nitrogen concentrations using hyperspectral satellite imagery. The Journal of Agricultural Science 146, 65–75.

Reddy, K.R., Zhao, D., 2005. Interactive effects of elevated CO_2 and potassium deficiency on photosynthesis, growth, and biomass partitioning of cotton. Field Crops Research 94, 201–213. doi:10.1016/j.fcr.2005.01.004

Richter, R., Schläpfer, D., 2011. Atmospheric/topographic correction for airborne imagery. ATCOR-4 user guide.

Rondeaux, G., Steven, M., Baret, F., 1996. Optimization of soil-adjusted vegetation indices. Remote Sensing of Environment 55, 95–107. doi:10.1016/0034-4257(95)00186-7

Rouse, J.W., Haas, R.H., Schell, J.A., Deering, D.W., n.d. Monitoring Vegetation Systems in the Great Plains with ERTS [WWW Document]. ResearchGate. URL https://www.researchgate.net/publication/246866091_Monitoring_Vegetation_Systems_in_the_Great _Plains_with_ERTS (accessed 6.29.17).

Rouse, J.W., Haas, R.H., Schell, J.A., Deering, D.W., Harlan, J.C., 1974. Monitoring the vernal advancement and retrogradation (green wave effect) of natural vegetation, NASA/GSFC type III final report: Greenbelt, Maryland, NASA, 371 p.

Rubio, E., Caselles, V., Badenas, C., 1997. Emissivity measurements of several soils and vegetation types in the 8–14, μm Wave band: Analysis of two field methods. Remote Sensing of Environment 59, 490–521.

Schellberg, J., Hill, M.J., Gerhards, R., Rothmund, M., Braun, M., 2008. Precision agriculture on grassland: Applications, perspectives and constraints. European Journal of Agronomy 29, 59–71. doi:10.1016/j.eja.2008.05.005

Shamsi, U.M., 2005. GIS applications for water, wastewater, and stormwater systems. CRC press.

Singh, D., Srivastava, V., Pandey, B., Bhimsaria, D., 2009. APPLICATION OF NEURAL NETWORK WITH ERROR CORRELATION AND TIME EVOLUTION FOR RETRIEVAL OF SOIL MOISTURE AND OTHER VEGETATION VARIABLES. Progress In Electromagnetics Research B 15, 245–465. doi:10.2528/PIERB09043003

Singh, P., Kato, Z., Zerubia, J., 2014. A multilayer markovian model for change detection in aerial image pairs with large time differences, in: Pattern Recognition (ICPR), 2014 22nd International Conference On. IEEE, pp. 924–929.

Smith, R.B., 2001. Introduction to remote sensing of the environment. 2001b. www. microimages. com.

Song, K., Zhou, X., Fan, Y., 2010. RETRIEVAL OF SOIL MOISTURE CONTENT FROM MICROWAVE BACKSCATTERING USING A MODIFIED IEM MODEL. Progress In Electromagnetics Research B 26, 383–399. doi:10.2528/PIERB10072905

Sripada, R.P., Heiniger, R.W., White, J.G., Meijer, A.D., 2006. Aerial Color Infrared Photography for Determining Early In-Season Nitrogen Requirements in Corn. Agronomy Journal 98, 968. doi:10.2134/agronj2005.0200

Srivastava, H.S., Patel, P., Sharma, Y., Navalgund, R.R., 2009. Large-Area Soil Moisture Estimation Using Multi-Incidence-Angle RADARSAT-1 SAR Data. IEEE Transactions on Geoscience and Remote Sensing 47, 2528–2535. doi:10.1109/TGRS.2009.2018448

Steele, M., Gitelson, A.A., Rundquist, D., 2008. Nondestructive estimation of leaf chlorophyll content in grapes. American Journal of Enology and Viticulture 59, 299–305.

Steele-Dunne, S.C., McNairn, H., Monsivais-Huertero, A., Judge, J., Liu, P.-W., Papathanassiou, K., 2017. Radar remote sensing of agricultural canopies: A review. IEEE Journal of Selected Topics in Applied Earth Observations and Remote Sensing 10, 2249–2273.

Stöcker, C., Bennett, R., Nex, F., Gerke, M., Zevenbergen, J., 2017. Review of the Current State of UAV Regulations. Remote Sensing 9, 459. doi:10.3390/rs9050459

Thenkabail, P.S., Enclona, E.A., Ashton, M.S., Van Der Meer, B., 2004. Accuracy assessments of hyperspectral waveband performance for vegetation analysis applications. Remote sensing of environment 91, 354–376.

Thenkabail, P.S., Lyon, J.G., 2016. Hyperspectral remote sensing of vegetation. CRC Press.

Thenkabail, P.S., Mariotto, I., Gumma, M.K., Middleton, E.M., Landis, D.R., Huemmrich, K.F., 2013. Selection of hyperspectral narrowbands (HNBs) and composition of hyperspectral twoband vegetation indices (HVIs) for biophysical characterization and discrimination of crop types using field reflectance and Hyperion/EO-1 data. IEEE Journal of Selected Topics in Applied Earth Observations and Remote Sensing 6, 427–439.

Thenkabail, P.S., Smith, R.B., De Pauw, E., 2002. Evaluation of narrowband and broadband vegetation indices for determining optimal hyperspectral wavebands for agricultural crop characterization. Photogrammetric Engineering and Remote Sensing 68, 607–622.

Thenkabail, P.S., Smith, R.B., De Pauw, E., 2000. Hyperspectral vegetation indices and their relationships with agricultural crop characteristics. Remote sensing of Environment 71, 158–182.

Topp, G.C., Davis, J.L., Annan, A.P., 1980. Electromagnetic determination of soil water content: Measurements in coaxial transmission lines. Water Resources Research 16, 574–582. doi:10.1029/WR016i003p00574

Treuhaft, R.N., Lowe, S.T., Cardellach, E., 2011. FORMULATING A VECTOR WAVE EXPRESSION FOR POLARIMETRIC GNSS SURFACE SCATTERING. Progress In Electromagnetics Research B 33, 257–276. doi:10.2528/PIERB11042910

Trishchenko, A.P., Cihlar, J., Li, Z., 2002. Effects of spectral response function on surface reflectance and NDVI measured with moderate resolution satellite sensors. Remote Sensing of Environment 81, 1–18. doi:10.1016/S0034-4257(01)00328-5

Truong-Loi, M.-L., Dubois-Fernandez, P., Freeman, A., Pottier, E., 2009. The conformity coefficient or how to explore the scattering behaviour from compact polarimetry mode. IEEE, pp. 1–6. doi:10.1109/RADAR.2009.4977048

Tucker, C.J., Elgin, J.H., McMurtrey, J.E., Fan, C.J., 1979. Monitoring corn and soybean crop development with hand-held radiometer spectral data. Remote Sensing of Environment 8, 237–248. doi:10.1016/0034-4257(79)90004-X

van Zyl, J.J., Arii, M., Kim, Y., 2011. Model-Based Decomposition of Polarimetric SAR Covariance Matrices Constrained for Nonnegative Eigenvalues. IEEE Transactions on Geoscience and Remote Sensing 49, 3452–3459. doi:10.1109/TGRS.2011.2128325

Villa, P., Stroppiana, D., Fontanelli, G., Azar, R., Brivio, P.A., 2015. In-season mapping of crop type with optical and X-band SAR data: A classification tree approach using synoptic seasonal features. Remote Sensing 7, 12859–12886.

Viña, A., Gitelson, A.A., Nguy-Robertson, A.L., Peng, Y., 2011. Comparison of different vegetation indices for the remote assessment of green leaf area index of crops. Remote Sensing of Environment 115, 3468–3478. doi:10.1016/j.rse.2011.08.010

Wang, Y., Paris, J.F., Davis, F.W., 1998. Inclusion of a Simple Multiple Scattering Model into a Microwave Canopy Backscatter Model. Remote Sensing of Environment 63, 101–111. doi:10.1016/S0034-4257(97)00129-6

Wentao An, Yi Cui, Jian Yang, 2010. Three-Component Model-Based Decomposition for Polarimetric SAR Data. IEEE Transactions on Geoscience and Remote Sensing 48, 2732–2739. doi:10.1109/TGRS.2010.2041242

Woolley, J.T., 1971. Reflectance and Transmittance of Light by Leaves. PLANT PHYSIOLOGY 47, 656–662. doi:10.1104/pp.47.5.656

Yamaguchi, Y., Moriyama, T., Ishido, M., Yamada, H., 2005. Four-component scattering model for polarimetric SAR image decomposition. IEEE Transactions on Geoscience and Remote Sensing 43, 1699–1706. doi:10.1109/TGRS.2005.852084

Yi Cui, Yamaguchi, Y., Jian Yang, Kobayashi, H., Sang-Eun Park, Singh, G., 2014. On Complete Model-Based Decomposition of Polarimetric SAR Coherency Matrix Data. IEEE Transactions on Geoscience and Remote Sensing 52, 1991–2001. doi:10.1109/TGRS.2013.2257603

Zarco-Tejada, P.J., Berjón, A., López-Lozano, R., Miller, J.R., Martín, P., Cachorro, V., González, M.R., De Frutos, A., 2005. Assessing vineyard condition with hyperspectral indices: Leaf and canopy reflectance simulation in a row-structured discontinuous canopy. Remote Sensing of Environment 99, 271–287.

Zhang, N., Wang, M., Wang, N., 2002. Precision agriculture - a worldwide overview. Computers and Electronics in Agriculture 36, 113–132. doi:10.1016/S0168-1699(02)00096-0

Abbreviations

ACE	Active Contrast Enhancement
AGL	Above Ground Level
ATCOR	Atmospheric/Topographic Correction
BOA	Bottom of the Atmosphere
CI_RedEdge	Red Edge Chlorophyll Index
CNES	Centre National d'Études Spatiales
CONOPS	Concept of Operations
DDE	Digital Detail Enhancement
DEM	Digital Elevation Model
DSM	Digital Surface Model
DTM	Digital Terrain Model
EASA	European Aviation Safety Agency
EO	Earth Observation
EOEI	Earth Observation Entrepreneurship Initiative
ESA	European Space Agency
EU	European Union
EXIF	EXchangeable Image File
FAA	Federal Aviation Administration
FAO	Food and Agriculture Organization
FAPAR	Fraction Of Absorbed Photosynthetically Active Radiation
GCP	Ground control point
GEOGLAM	Group on Earth Observations Global Agricultural Monitoring
GIS	Geographic Information Systems
GNDVI	Green Normalized Difference Vegetation Index
GNSS	Global Navigation Satellite Systems
GPS	Global Positioning System
ha	hectares
HNSDMS	Hellenic Sentinel Data Mirror Site
ICAO	International Civil Aviation Organization
ICT	Information Communication Technologies
IFOV	Instantaneous Field of View
IMU	Inertial Measurement Units
IoT	Internet of Things
IPCC	Intergovernmental Panel on Climate Change
L1A	Level-1A
L1B	Level-1B
L1C	Level-1C
LAI	Leaf Area Index

LTDN	Local Time at Descending Node
m	meters
MACCS	Multi-sensor Atmospheric Correction and Cloud Screening
MEMS	Micro-Electro-Mechanical-Systems
Mpx	Megapixels
MSI	Multispectral Instrument
NDRE	Normalized Difference Red-Edge
NDVI	Normalized Difference Vegetation Index
NDWI	Normalized Difference Water Index
NIR	Near-Infrared
NIRRG	NIR-Red-Green
nm	nanometers
NOA	National Observatory of Athens
OSAVI	Optimized Soil Adjusted Vegetation Index
PA	Precision Agriculture
PAR	Photosynthetic Active Radiation
PPP	Public–Private Partnership
PV	Precision Viticulture
RENDVI	Red Edge Normalized Difference Vegetation Index
RGB	Red-Green-Blue
ROI	Region Of Interest
RPAS	Remotely Piloted Aircraft Systems
RS	Remote Sensing
S2	Sentinel-2
SAR	Synthetic Aperture Radar
SAVI	Soil Adjusted Vegetation Index
SBAS	Satellite-based augmentation systems
SR_GRVI	Simple Ratio Green Ratio Vegetation Index
SSO	Smart Scene Optimization
SWIR	Shortwave Infrared
TIR	Thermal Infrared
TOA	Top of the Atmosphere
UAS	Unmanned Aircraft Systems
UAV	Unmanned Aerial Vehicles
USA	United States of America
UTM	Universal Transverse Mercator
VI	Vegetation Indices
VIN	Vegetation Index Number
VNIR	Visible Near Infrared
XMP	Extensible Metadata Platform
µm	micrometers

the end?